NOCTURNAL MEASUREMENTS OF UPPER ATMOSPHERIC OZONE AND THE LUNAR ULTRAVIOLET FLUX

by

Brian Henry Horton B.Sc. (Qld).

Department of Physics

A thesis
presented for the degree of
Doctor of Philosophy
in the
University of Adelaide
May, 1968.

CONTENTS

SUMMARY

The experiments described in this thesis were performed with rocket borne, middle ultraviolet photometers. Results obtained from the experiments gave information, firstly, pertaining to the nocturnal distribution of atmospheric ozone between 35 and 75 kilometers, and secondly, regarding the spectral reflectivity of the lunar suface.

Because of the unusual environment in which they operated, some details of the design of the photometers will be given together with a discussion of their calibration and the means of determining aspect and height of the vehicles during flight.

The ozone distribution was obtained from measurements of the differential absorption, with respect to height, of radiation within selected wavelength regions. These regions lie within the Hartley absorption bands extending over the range 2000Å to 3000Å.

The light source used in making these measurements was the solar radiation reflected from the moon. Rocket launch times, in each case, were chosen so that the lunar phase angle was within a 10° of full moon.

Within the range of sensitivity of the photometers,

the results indicated that a negligibe amount of ozone remained above the sensors when the vehicles were still some 5 to 10 kilometers below the apogee heights which lay between 80 and 85 kilometers. The fluxes observed within 5 kilometers of apogee were then taken as bases for simple extrapolation, in this wavelength region, to values existing outside the earth's atmosphere.

The results obtained by this method were then used for broadband spectrophotometry of the lunar reflected solar radiation and estimates made of the spectral reflectivity of the moon's surface.

The flights were made during early Summer and late Winter in the Southern Hemisphere. In both cases, the number density of ozone molecules above 60 kilometers is shown to be greater than when the atmosphere is sunlit. The difference, however, is not as great as that predicted by the application of photochemical and recombination theories to simple model atmospheres.

Values obtained for lunar reflectivity were compared with measurements of spectra/reflectivity of various stony and glassy surfaces, made by other workers in the laboratory. The implications resulting from this comparison are discussed with reference to the nature of the lunar surface.

PREFACE

This thesis contains no material which has been accepted for the award of any other degree or diploma in any University. To the best of the author's knowledge and belief it contains no material previously published or written by another person, except when due reference is made in the text.

ACKNOWLEDGEMENTS

The rocket experiments described in this thesis were carried out in co-operation with the Flight Projects Group, Weapons Research Establishment. The author would like to express his thanks to Mr B. Rofe, Principal Officer and Mr F. Burger, Engineer Officer of Flight Projects Group for making these experiments possible.

The author would also like to thank Mr P. Stevenson and Mr R. Hurn of the Physics Department, University of Adelaide for construction of the electronic systems and preflight checks of the instrumentation.

Finally the author would like to thank his supervisor, Professor J.H. Carver most sincerely for his guidance throughout the course of this work.

CHAPTER 1

RADIATION AND CHEMISTRY IN THE UPPER ATMOSPHERE

1.1 Introduction

The atmosphere, its structure and composition; have been the subject of inquiry for many years. While the lower portion, or troposphere, has always been open to direct investigation of varying degree, and the top layers, or ionosphere, has been reachable by radio means for some time, it is only in the last twenty years that the advent of rockets has made the intermediate region, or chemosphere, accessable to any but very indirect methods. The advances in rocket and satellite technology have made it possible to make relatively detailed studies of the temperatures, atmospheric densities and compositions, gravity and magnetic fields and surface structures of other planets of our solar system as well as the earth. Such measurements may provide information, directing theoretical studies and thus leading to an understanding of the evolution of planets and stellar systems.

1.2 The Solar Spectrum

The primary source of energy, inducing reactions in a planetary atmosphere, is the parent star of the system. In the case of the solar system, the star is the sun. Until recently the spectrum of the sun was approximated to that of a black body at a temperature of about 5785°K. With the advent of rocket vehicles, capable of climbing above the atmosphere, measurements of the solar spectrum have been made by such workers as Tousey (1963), which have extended knowledge to the ultraviolet wavelengths. Despite these studies, there is still an uncertainty in the value of the solar flux of approximately 10% at about 3000Å, this uncertainty increasing to about 20% at 2000Å. These values are quoted by Tousey (1966) and supported by Furakawa et al (1967). At still shorter wavelengths theory predicts time variations and these have been observed, changing with the degree of solar activity. The two main regions of the spectrum contributing to atmospheric effects are those to the short wavelength side of 3000Å and to the long wavelength side of 9000Å.

1.3 The Infrared Region

In the infrared region there are a number of alternating windows and absorption bands. Infrared absorption is chiefly due to induced vibrational and rotational transitions in polyatomic molecules. By comparison of the spectral absorption of the atmospheric gases, H_2O vapour, CO_2, and O_3 with the observed solar spectrum at sea level, it has been shown that these are the principle absorbers in the infrared portion of the spectrum. Such a comparison, by Howard (1961), is shown in Figure 1.1. Yamamoto (1962) has computed the absorption by these constituents for a model atmosphere, and his results are shown in Figure 1.2. Despite this absorption of solar energy in the infrared, the overall effect of absorption and emission in this region, in the lower atmosphere, is a loss of heat. The excess of emission comes from the heated gases rising from the earths surface. This statement applies to the global atmosphere but not to particular latitudinal regions. Some small heating occurs in the equatorial latitudes where the water vapour content is high, (Murgatroyd 1965). Infrared absorption has little effect upon the physics and chemistry of formation and maintenance of the atmosphere, but a large effect upon the energy transport mechanisms, and the production of an

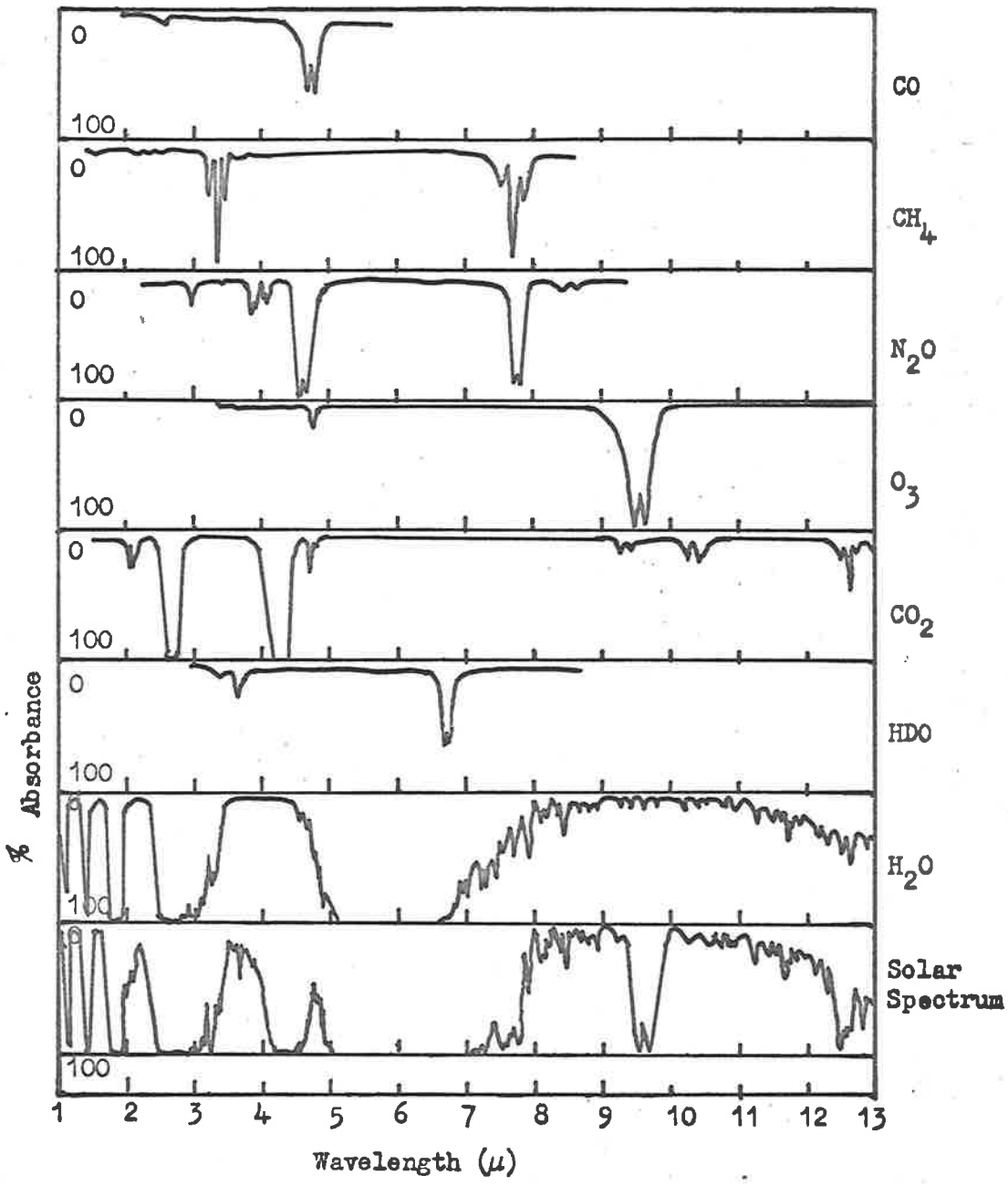

Figure 1.1 Comparison of absorption by atmospheric gases with the infrared spectrum of the sun ex Howard, 1961.

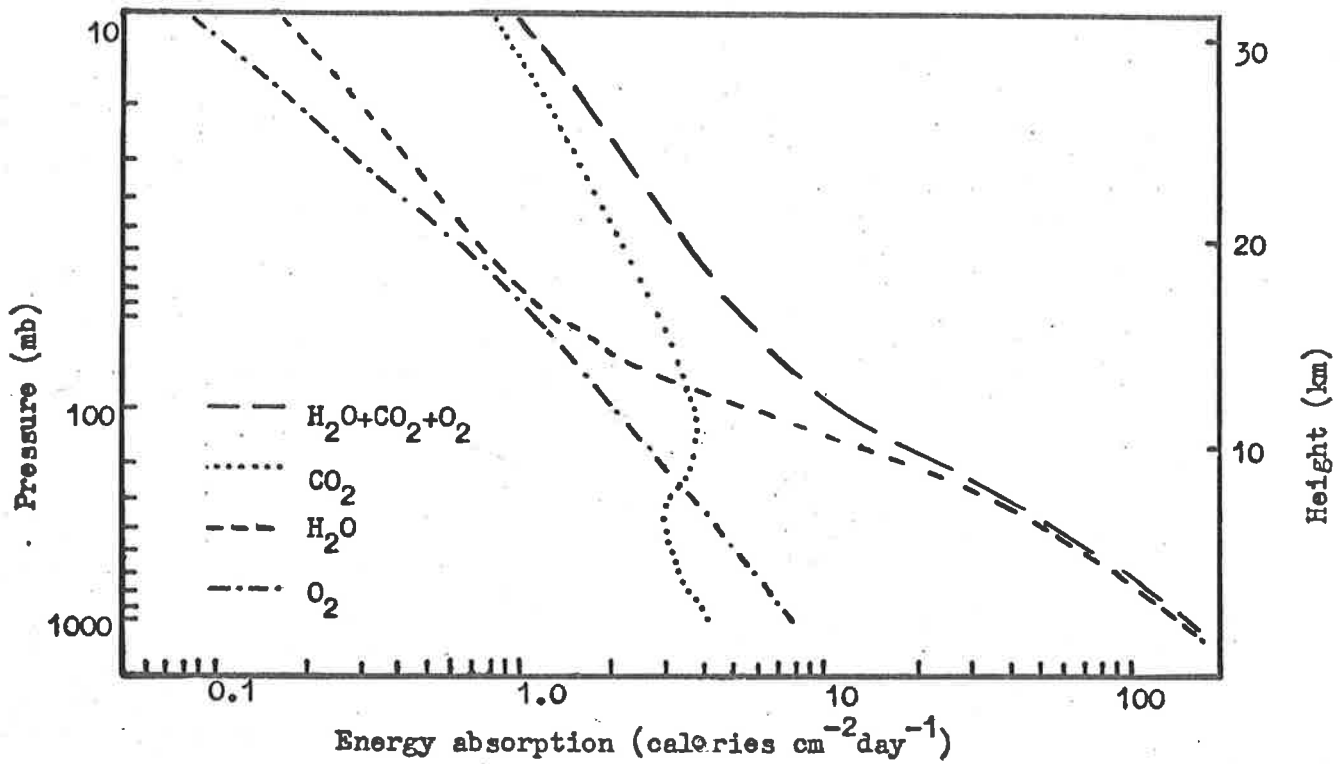

Figure 1.2 Energy absorbed by H_2O, CO_2 and O_2 for a model atmosphere. After Yamamoto (1962).

environment suitable for life.

1.4 The Ultraviolet Region

The spectral region to the short wavelength side of 3000Å may be divided into two parts. Above 1350Å, the radiation, reacting with the principle constituents of the atmosphere, produces molecular excitation and dissociation. This absorption, measured in terms of the height at which solar intensity is reduced from its value outside the atmosphere by a factor of e^{-1}, takes place at heights between 25 and 100 kilometers, with a sharp drop to sea level beyond 3200Å.

The effects of wavelengths shorter than 1350Å are molecular ionization, excitation and dissociation and atomic excitation and ionization. The height associated with these interactions varies with wavelength. Between 1150Å and 1350Å, due to the structure of the molecular oxygen absorption coefficient, the height varies from 70 kilometers to 150 kilometers. Between 850Å and 1150Å the results are uncertain, because of difficulty of measurement, but appear close to a value of 100 kilometers. The absorption height rises rapidly for wavelengths below

850Å to a maximum of 170 kilometers near 700Å, then falls smoothly towards 100 kilometers near 150Å, where the complex structure of the absorption coefficient for soft X-rays takes control.

In considering the effects of energy interchange in the atmosphere, the most important region of the spectrum is that lying between 2000Å and 3000Å. The reason for this is the steep increase of energy content, with wavelength, in the solar spectrum over this interval, coupled with the large absorption coefficient of the minor atmospheric constituent, ozone, the triatomic form of oxygen. Figure 1.3 shows the energy distribution in the solar spectrum between 2080Å and 3200Å taken from (Furukawa et al 1967), while Figure 1.4 shows the absorption cross sections for O_2 and O_3 in this wavelength region.

1.5 The Photochemical Reactions of the Chemosphere

It can be seen that ozone is the main absorber of radiant energy in this part of the spectrum, and, as such, is responsible for the peak in the atmospheric

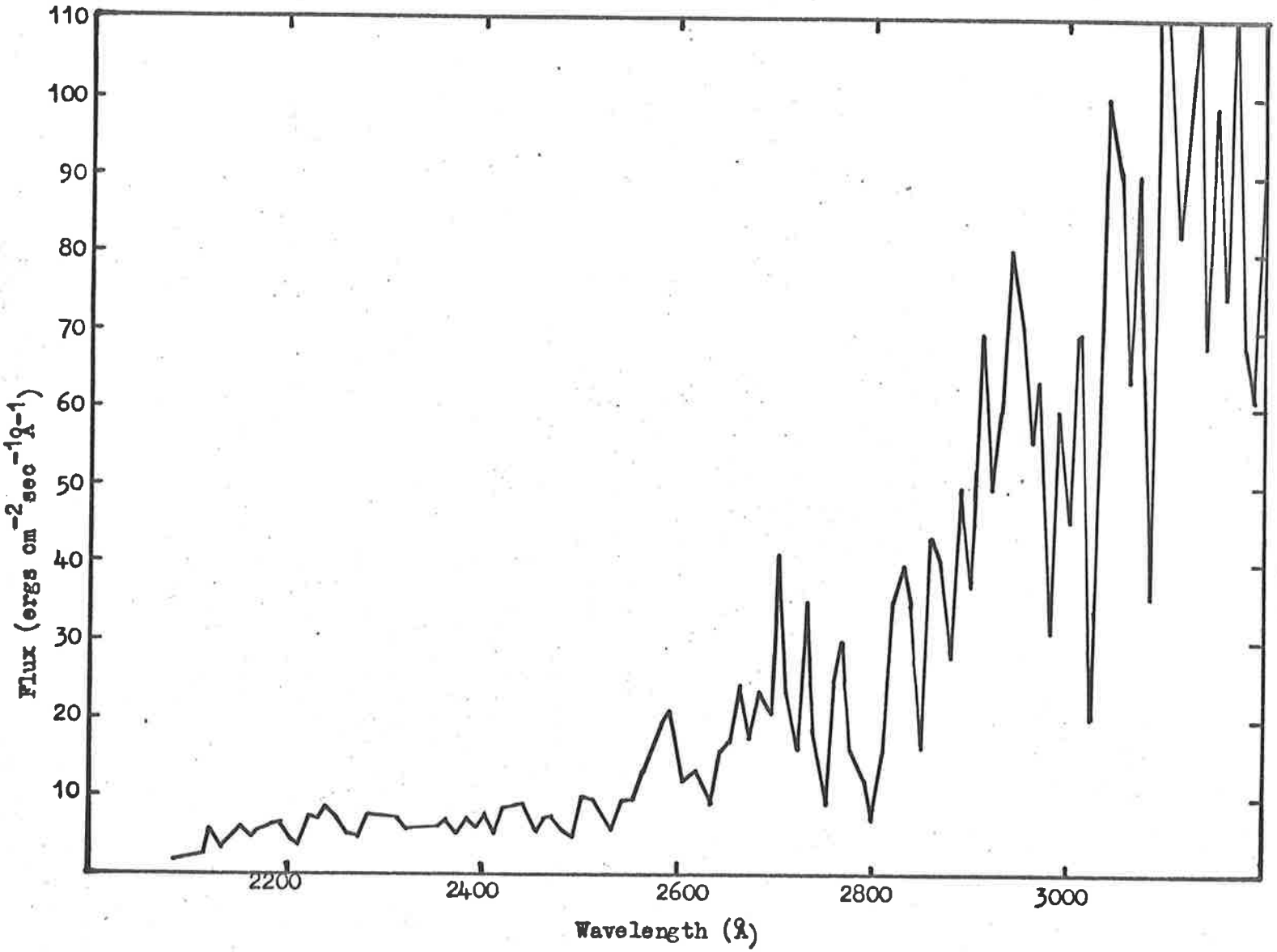

Figure 1.3 The solar spectrum. ex Furakawa et al, 1967.

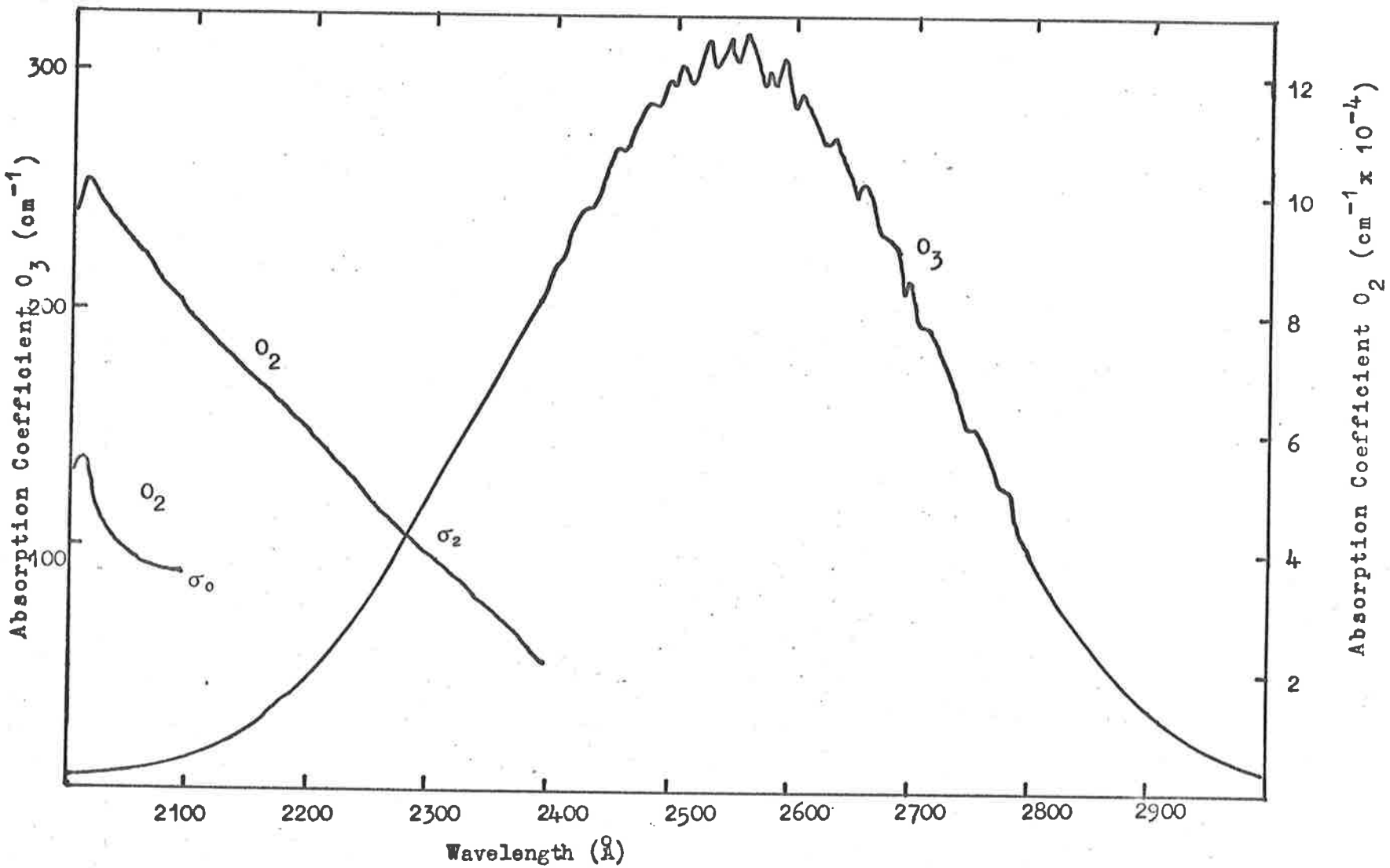

Figure 1.4 Absorption coefficients of O_2 (after Blake et al 1966) and O_3 (after Inn and Tanaka (1959), σ_i refers to the coefficient as measured at an extrapolated to i atmosphere.

temperature curve which is centered at approximately 50 kilometers. A comprehensive survey of the solar heating of the atmosphere is given by Murgatroyd (1957).

If we consider the principle reacting molecular species, in the height range 30 to 100 kilometers, to be O_2, O_3 and H_2O, the following photo reactions are of importance:-

$$O_2 + h\nu \text{ --- } O(^3P) + O(^3P)$$
$$1750\text{Å} < \lambda < 2424\text{Å}$$

$$O_2 + h\nu \text{ --- } O(^1D) + O(^3P)$$
$$\lambda < 1750\text{Å}$$

$$O_3 + h\nu \text{ --- } O_2 + O(^3P)$$
$$3100\text{Å} < \lambda < 11800\text{Å}$$

$$O_3 + h\nu \text{ --- } O_2 + O(^1D)$$
$$\lambda < 3100\text{Å}$$

$$H_2O + h\nu \text{ --- } OH + H$$
$$\lambda < 2390\text{Å}$$

As a result of these reactions, and collisonal processes occurring between the original components and the products of the reactions, the following molecular and

and atomic species exist in this region of the atmosphere when it is sunlit:-

O, O_2, O_3, OH, HO_2, H_2O_2, H_2O, H and H_2.

Other species that are present in relatively high concentration, but which take little direct part in the photochemical reactions in this part of the atmosphere are:-

N_2 and CO_2.

Other minor constituents are:-

NO, NO_2, CH_4, Na, A and He.

Molecular nitrogen, while taking little part in the direct photochemical reactions, probably plays an important part in three body collisional reactions. The occurrence of these atomic and molecular species and their reactions are discussed by Bates and Nicolet (1950), Leovy (1964), Nicolet (1964), Warneck (1964), Hunt (1965), and Cadle and Powers (1966).

1.6 Model Atmosphere Methods and Results

There have been several attempts to combine known and estimated reaction rates of the various reactions

with measured and estimated atomic and molecular densities, theoretical and measured temperatures and the calculated solar flux at different heights, to give values to the number densities of all important gases, fluxes of radiation resulting from some of the reactions, and other predictable events.

A recent study by Hunt (1966), gives the results of two separate calculations of the densities of various molecular species in the upper atmosphere. Both are for equinoctial equatorial conditions and are based on the U.S. Standard Atmosphere (1962).

The first model assumes an atmosphere with the initial gas containing O_2 and H_2O as reactants. The H_2O concentration used is based on the assumption of a constant mixing ratio equal to that found for stratospheric conditions by other workers as $2\text{-}3 \times 10^{-6}$ grams/gram or 5×10^{-6} H_2O molecules per air molecule.

Using time variable values for solar radiation, an iteration process was used by Hunt to produce the molecular concentrations as a function of height, when equilibrium conditions have been reached.

The second model studied by Hunt starts with the

molecular concentrations produced by the equilibrium method, and, by integration with respect to time over eight diurnal cycles, produces repeatable concentrations for succeeding twenty four hour periods. The results of the work by Hunt are shown in Figure 1.5, for noon and pre-dawn conditions.

This latter model is among the most detailed developed with regard to the diurnal number density variations of the more reactive constituents of the upper atmosphere.

The deficiency of Hunt's models is the lack of reference to latitude variations. A series of models by Blankenship and Crutzen (1966) of the oxygen allotropes and their variation with space and time shows that the variations with latitude is of the same order of magnitude as the diurnal variations and should be taken into account in future production of models.

1.7 Measurements of Atmospheric Content other than Ozone

Despite the importance of obtaining an under-

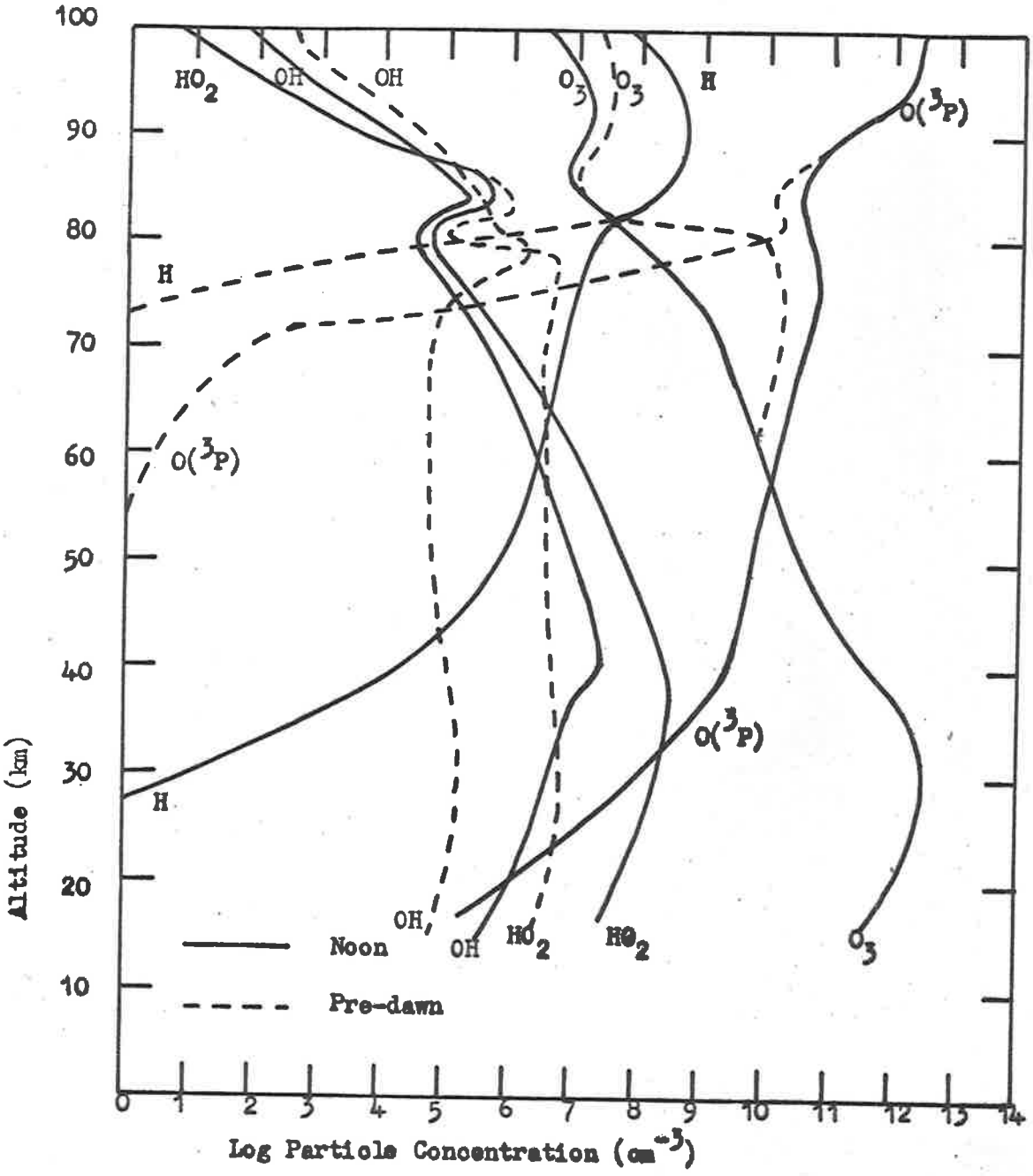

Figure 1.5 Distribution of Atmospheric species with diurnal effects. After Hunt (1966).

standing of the details of reactions occurring in the atmosphere in the height range 30 to 100 kilometers, relatively few measurements have been made of the number densities of atmospheric constituents in this region. Relative values of O/O_2 and N/N_2 ratios have been made by mass spectrographs; as example, the work of Schaefer (1963).

Measurements of the absorption of solar radiation have been used by a number of workers such as Friedman et al (1964), Smith and Weekes (1965), Carver et al (1965), to obtain values of molecular oxygen concentrations. This method has only been suitable for obtaining values above 60 kilometers as the instruments used do not have sufficient range to measure intensities much reduced by absorption at lower levels.

In a theoretical study, Miller (1960), suggests that there is still considerable atomic oxygen at about 40 kilometers, being 10^{10}-10^{11} cm^{-3}. On the basis of this suggestion, a test of the assumption of a constant mixing ratio for O_2 to high altitudes would provide further information as to the reactions in the atmosphere.

The production of OH, resulting from photo-dissociation of H_2O vapour and subsequent reactions, has been calculated by Wallace (1962) and Hunt (1966) and

compared by Hunt with the observations by Tarasova (1963) and Packer (1961) of the emission by OH. There is some disagreement between the structures as calculated and observed, though the general distributions are similar.

Attempts at measuring the water vapour concentration above 30 kilometers have been made by Williamson and Houghton (1965) and Kartashev et al (1966). Both methods rely on the measurement of the 6.3 micron radiation of water vapour from this region. In both cases, the measurements have exceeded expectation in their intensity, and this excess has been ascribed to some other atmospheric constituent, say OH, NO or N_2O.

1.8 Measurements of Ozone Content in a Sunlit Atmosphere

Measurements of the ozone concentration above 30 kilometers have been made by a number of different methods. The earliest developed was the Umkehr method (see Section 2.1), developed by Gotz et al (1934). The measurements necessary for deduction of the results are made at sea level. With the advent of telemetry systems, enabling the results of measurements made in flight to be

transmitted to ground stations, balloon borne instrumentation was developed, which, with the advance of balloon technology, was capable of carrying out in situ determinations of ozone density up to heights of 35 to 40 kilometers. Instruments of this type have been developed by Brewer and Milford (1960) and Regener (1960).

With the use of rockets for atmospheric investigation, the absorption of solar radiation by ozone at particular wavelengths has been used for measurement of the concentration of this gas in the atmosphere. An example of such a measurement is that of Johnson et al (1952). Observations of the absorption of solar radiation through a slant path through the atmosphere as viewed from an orbiting satellite have also been used for ozone concentration determinations by such workers as Rawcliffe et al (1963) and Miller and Stewart (1965).

The details of these various methods of measurement will be discussed in Chapter 2.

1.9 Measurement of Atmospheric Components in the Absence of Sunlight

As solar radiation is important in the production

of the reacting species in the upper atmosphere, it is obvious that considerable difference is to be expected in the conditions existing at high altitudes between periods when the atmosphere is sunlit and when the solar radiation is absent. The measurements of OH by Heppner and Meredith (1958) and Packer (1961) and of H_2O vapour by Kartashev et al (1966) were made at night, the latter when the satellite vehicle, making the measurements, was on the side of the earth away from the sun. These two constituents, however, are difficult to measure accurately as measurements depend upon the excitation mechanisms resulting from the dissociation and recombination of oxygen, the predominant reactions occurring in this part of the atmosphere. The method of measuring molecular oxygen that has been used for daylight flights is regarded as unsuitable for use at night as there are few sources, thought to be of sufficient strength, to enable the recording of change of absorption with height, necessary for this method. It is possible that the lunar surface may reflect ultraviolet radiation of sufficient strength to record the necessary change in signal if an ion chamber, used as a detector, is operated at gas gain. An experiment to measure the intensity of reflected radiation is at present past the design stage and under construction.

When considering a measurement of the ozone distribution at night, the value of the lunar flux in the middle ultraviolet, as measured by Heddle (1962), seemed to provide a possible source. While the value determined by Heddle was not regarded as very accurate, it proved the intensity was of sufficient strength for the purpose and, in the measurement of its value, over a wider spectral range, also would supply further information about the nature of the lunar surface itself. With these two objects in mind, the experiments to be described were designed.

CHAPTER 2

METHODS OF MEASUREMENT OF OZONE CONCENTRATION IN THE UPPER ATMOSPHERE

2.1 The Umkehr Method

Various methods of measurement of ozone at altitudes greater than 30 km mentioned in Chapter 1. These are discussed in some detail below.

The first was the Umkehr method, developed by Gotz et al (1934). The method depends upon the signals received, at ground level, from two narrow band pass photometers centred at two wavelengths within the relatively small cross-section Huggins absorption bands of O_3 in the region 3000Å to 3500Å. The ratio of the signals received is recorded as a function of solar zenith angle, the relation being of the form, (Craig, 1965)

$$\frac{I(\lambda_1)}{I(\lambda_2)} = \frac{K(\lambda_1)\, E_\infty(\lambda_1) \int_0^\infty \rho\, \tau_{oz}(\lambda_1)\, \tau_{z\infty}(\lambda_1)\, dz}{K(\lambda_2)\, E_\infty(\lambda_2) \int_0^\infty \rho\, \tau_{oz}(\lambda_2)\, \tau_{z\infty}(\lambda_2)\, dz}$$

where $I(\lambda_i)$ = measured intensity at λ_i

$K(\lambda_i)$ = Rayleigh scattering coefficient at λ_i

$F(\lambda_i)$ = Solar flux at the limit of the earths atmosphere at λ_i

ρ = air density at altitude z

$\tau_{\alpha\beta}(\lambda_i)$ = transmissivity of the slant air column between the altitude limits α and β.

The values of this last term are functions of the zenith angle, altitude z, and the absorption coefficient of O_3 in the pass band of the photometer.

Numerical methods for the derivation of profiles from the measurements have been given by Walton (1957) and Ramathan and Dave (1957). Very little information about the high altitude distribution can come from this method as it rests on the assumption of zero ozone above some fixed level. It is extremely useful, however, for recording the seasonal variations in height and density of the maximum concentration peak between 20 and 40 kilometers.

2.2 Balloon Borne Chemical Sensors

While the Umkehr method uses measurements made at ground level, other means require the instruments to be lifted to some height in the atmosphere, the height depending on the instrument used. One type depends upon the reaction of ozone with potassium iodide, viz.

$$O_3 + 2KI + H_2O \rightarrow 2KOH + O_2 + I_2 .$$

The number of ozone molecules taking part in the reaction is measured by electrolysis of the iodine formed in the solution. If a potential difference is maintained in the nonreacting solution, the electrodes are polarised and no current flows. Upon release of the I_2 from the reaction, at the cathode,

$$I_2 + 2e^- \rightarrow 2I^-$$

there is a drift of the negative ion to the anode where

$$2I^- \rightarrow I_2 + 2e^- .$$

Thus, for each ozone molecule interacting, two electrons flow into the circuit.

Two systems for collecting this current are used. These were developed by Brewer and Milford (1960). They

are

(a) The "Transmogrifier" in which the KI solution is dripped, through the ozone atmosphere, onto the cathode, then flows down an insulating rod, giving up the electrons to the anode.

(b) The "Bubbler" in which the ozone atmosphere is bubbled through the solution at a constant rate. The negative ions formed at the cathode are collected at a silver or mercury anode. Here the electrons are passed to the anode while the iodine reacts with the anode material, forming an insoluable salt and is so removed from the solution.

These methods are used in balloon flights and may give information as to the ozone distribution up to heights in the region of 35 to 40 kilometers.

Another method involving the chemical properties of ozone is that developed by Regener (1960), which depends upon the chemiluminescent reaction of ozone with the luminescent material 'Luminol'. Samples of air are drawn past a disc, coated with Luminol, and the radiation resulting from the reactions is, as found by Regener (1960), proportional to the ozone content of the air sample. If

the disc is viewed by a photomultiplier, the observed current is then a measure of the ozone content of the air sample. This method has been widely used by the United States Air Force Cambridge Research Laboratory, the early results of which are presented by Hering and Barden (1964).

2.3 Rocket Borne Sensors

Modifications of Regeners balloon borne ozonosonde have been developed by Randhawa (1966a, 1966b), for the measurement of ozone concentrations down from approximately 60 kilometers over the White Sands Missile Range. The first of these instruments consisted of a chamber which was periodically opened to the atmosphere, as the sonde descended from the peak height by parachute, having been placed at altitude by an ARCAS rocket. On opening the chamber, a sample of air from the surroundings of the sonde entered the chamber. The chamber was then closed, the closing action opened a shutter which allowed the photomultiplier to view the chemiluminescent disc, thus measuring the ozone content of the sample enclosed.

The second instrument operated on a similar system except that the sample chamber was continuously open to the atmosphere through a folded channel which acted as a light trap, the main body acting as a storage volume, while the chemiluminescent disc was mounted along part of the path from the atmosphere to the storage volume.

Randhawa's method of measurement of high altitude ozone has the advantage of being independent of external conditions to the extent that the experiment may be made at any time of day, without variation of the instrumentation in any way. The weakness of the method appears to lie in the assumptions that must be made as to the dynamics of flow, first in relation to the conditions near the skin of the sonde relative to those some distance from it as it falls, and second, the effect of flow over the surface of the sonde upon the rate of flow into the storage chamber past the sampling region. The results obtained by Randhawa will be presented in Chapter 6.

2.4 The Atmosphere Radiance Method

An indirect approach to the determination of the upper atmospheric ozone distribution has been formulated by

Twomey (1961). This method involves the use of measurements of the scattering of the solar radiation by the earth atmosphere as a function of the solar zenith angle and the observation angle together with the expected depth of penetration as a function of wavelength. The atmospheric quantities involved include the vertical distribution of air, oxygen and ozone and the method calls for the fitting of the observed radiance values to those expected from perturbation calculations with a model atmosphere distribution as a starting point. Observations are made from satellite vehicles and an example of this method is the work of Friedman et al (1963). Because of the complex nature of the mathematical treatment that must be applied and the assumptions that must be made, it is not an ideal method of obtaining detailed ozone distribution profiles.

2.5 Measurement by Atmospheric Absorption

A further method of measuring high altitude ozone distributions uses the effect of absorption of radiation by the gas, the source of radiation being beyond the region of expected measurable ozone concentration. The first of these measurements was made by Johnson et al

(1952), who used rocket spectrometry in the region 2500Å to 3400Å. The spectrograms, taken as a function of altitude, show the extension of the observed solar spectrum towards the ultraviolet as the vehicle climbed through the atmosphere. By comparison of the distribution of radiation intensity as a function of wavelength, received at successively increasing altitudes, and applying knowledge of the absorption coefficient of ozone, the number of absorbing molecules between each observation point along the radiation path may be measured. The advantage of this method lies in the self consistency required within the whole part of the spectrum that is observed. While some uncertainty may exist in the number density determined at a particular wavelength, the requirement that the result associated with an adjacent wavelength must agree supplies a check on each determination.

The disadvantage of the system lies in the sophistication of the instrumentation required, and the necessity of recovery of the vehicle after the flight. Such a system is not suitable for recurrent measurements.

A method of determining the high altitude ozone profile, involving the use of artificial earth satellites, is that employed by Rawcliffe et al (1963) and Miller and

Stewart (1965). The experiment depends upon the measurement of the absorption of solar radiation along a slant path through the atmosphere during satellite sunset and sunrise. The path length of the radiation may be simply calculated, on making assumptions as to the scale height of the absorbing gas, according to the theory as presented by Smith and Weekes (1965). Because of the ranges of height in the atmosphere subtended at the satellite by the finite angular size of the sun some difficulty exists in the reduction of the results though this may be balanced to some extent by the collection of a large number of data points. A photometer, capable of employing this method and, also the method of Twomey, mentioned in section 2.4, has been included by the author in the payload of the Australian built satellite which it is planned to launch into a near polar orbit late in 1967. Details of this instrument and others included in the satellite will be given in Chapter 8.

2.6 Selection of Methods of Night Time Measurement

Because of the basic simplicity of absorption measurements, and their independence of the conditions in

the immediate location of the sensors, a system similar to that used by Johnson et al was decided upon, with variations in that high resolution spectrometry was replaced by broad band spectrometry and the intensity was recorded photoelectrically rather than photographically. This latter change meant that the information could be transmitted in real time by telemetry and did not require the recovery of the instrumentation. The facility of attitude control of the vehicle was not available so that the design had to make use of the dynamics of the vehicle in flight to obtain the number of measurements required for a meaningful measurement of the distribution.

2.7 Detail of Absorption Measurements

The measurement of gas densities by absorption depends upon the application of the law attributed to Beer, which states the absorbance of a parallel, monochromatic beam of radiation, in a homogeneous, isotropic medium, is proportional to the path length in the medium and to the concentration of the absorbing species along the path. For an element of path, dx, this may be stated as

$$\Delta I = -I_\lambda n \alpha_\lambda dx$$

Where I_λ = Radiant energy per unit wavelength interval at Wavelength, per unit area incident on a surface normal to the direction of the radiation.

ΔI_λ = The change in the intensity I after traversing a path length dx in the medium.

n = The number of absorbing particles per unit volume of the medium.

and α_λ = The absorption coefficient, at wavelength λ, of each particle, in units of area.

This form may be integrated to give

$$I_{2\lambda} = I_{1\lambda}\, e^{-n\alpha_\lambda x_{12}}$$

where x_{12} is the path length between the positions of measurements of $I_{1\lambda}$ and $I_{2\lambda}$, and the number density, n, is assumed constant over this distance.

In general, in atmospheric measurements, the value of n may not be considered as constant. If the details of the distribution are to be known, measurements should be made such that the path length between successive

measurements is small. If this is the case, the approximation,

$$n = \frac{\int_{\text{path}} n(x)\, dx}{\int_{\text{path}} dx},$$

may be made, where n(x) is the true distribution, in many cases unknown, of the number density along the path of the radiation.

2.8 Approximation of the Path Length

The path length of the radiation through the atmosphere is dependent upon the height difference between successive observations and the angle between the normal to the earth's surface, at the point of observation, and the position vector of the source of radiation.

Referring to Figure 2.1,

R = the radius of the earth

h_0 = the height of the observation at point P

θ_0 = the angular displacement of the source from the normal to the earth's surface through P

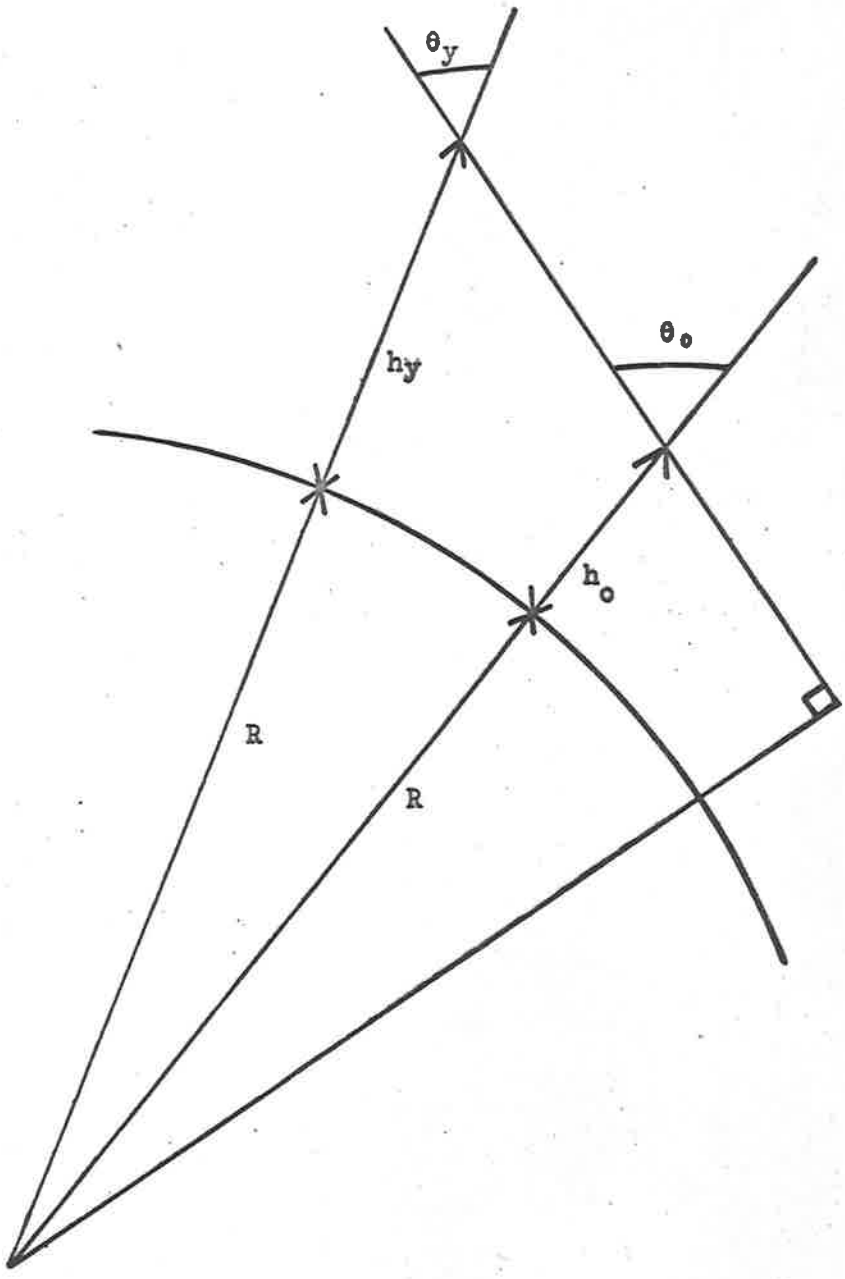

Figure 2.1

h_y = the height of an element of path length of the radiation towards P at position Y

θ_y = the angular displacement of the source from the normal to the earth's surface through the point Y

then, from the Sine relation,

$$\frac{\text{Sin } \theta_o}{R + h_y} = \frac{\text{Sin } \theta_y}{R + h_o}$$

$$\text{i.e.} \quad \text{Sec } \theta_y = \left(1 - \left(\frac{R + h_o}{R + h_y}\right)^2 \text{Sin}^2 \theta_o\right)^{-\frac{1}{2}}$$

If the assumption is made that Sec θ_y = Sec θ_o in calculating the magnitude of the path length element, the element ds is given by

$$ds = dh \text{ Sec } \theta_o$$

where dh = the distance along the normal to the earth's surface subtended by the path length element. The error introduced by this assumption may be determined by calculating the ratio of Sec θ_o to Sec θ_y as a function of θ_o and the height difference $(h_y - h_o)$. The results

of such a calculation for the values concerned in this study are shown in Figure 2.2. It may be seen that the error involved is of the order of a few percent over the ranges considered.

2.9 The Ozone Absorption Cross Sections

The ozone absorption cross section, because of its major effect upon the radiant energy interchange with the atmosphere, is of considerable importance to atmospheric studies. Due to the complex treatment required for poly atomic molecules and the lack of information relating to its molecular structure, Mulliken (1942) as example, little success has attended theoretical approaches to prediction of values of ozone cross sections. Due to the difficulty of measuring the concentration during measurement, there has also been some lack of consistency in the measured results presented. These differences are discussed by Inn and Tanaka (1959).

The principle regions of ozone absorption over the spectrum are listed below.

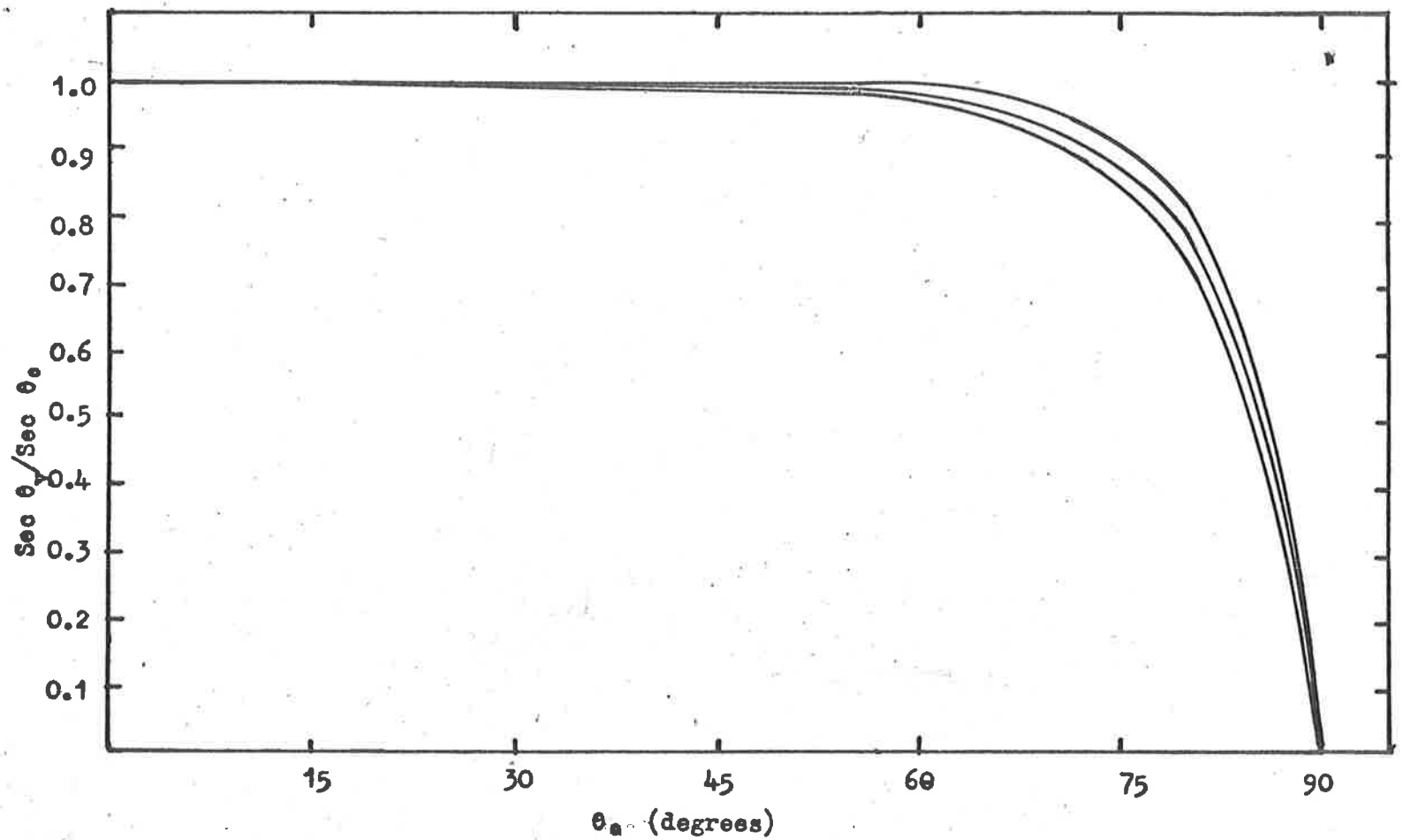

Figure 2.2 Ratio $\mathrm{Sec}\theta_y/\mathrm{Sec}\,\theta_o$ as a function of θ_o for (h_y-h_o) at 10 km (upper curve) 30 km (middle curve) and 50 km (lower curves).

Wavelength region	Form	References
1050 - 1500Å	Some bands and continuum	Tanaka, Inn and Watanabe
1500 - 2000Å	Continuum	Tanaka, Inn and Watanabe
2000 - 3000Å (Hartley Bands)	Continuum with suggestion of structure	Inn and Tanaka
3000 - 3500Å (Huggins Bands)	Bands	Inn and Tanaka
4350 - 7550Å (Chappuis Bands)	Continuum with suggestion of structure	Inn and Tanaka
3.3μ, 3.6μ, 4.8μ, 5.7μ.	Vibration-rotation bands	M. Griggs
9.0μ - 9.6μ	Strong vibration-rotation bands	Glough and Kneizys

The last listed bands, in the infra-red, are very temperature dependent and are unsuitable for absorption

measurements but, because of their strength, are important in the effects of atmospheric heating.

The bands existing in the vacuum ultraviolet region have very large cross sections but are of little use for absorption measurements in the atmosphere as molecular oxygen, while having a smaller cross section by some orders of magnitude, exceeds ozone in number density to such an extent that any absorption by ozone would be completely masked by that of molecular oxygen. To illustrate the optical density of the atmosphere at 1215Å, in the vacuum ultraviolet, values of cross section and number density of both ozone and molecular oxygen are listed below.

$$O_2 \text{ cross section} = 1 \times 10^{-20}\ cm^2 = \alpha O_2$$

$$O_3 \text{ cross section} = 7.5 \times 10^{-18}\ cm^2 = \alpha O_3$$

Height (km)	$n(O_2)$	$n(O_3)$	$\frac{\alpha_{O_2} n(O_2)}{\alpha_{O_3} n(O_3)}$
40	1.6×10^{16}	6×10^{11}	3.49×10^{1}
60	1.5×10^{15}	9×10^{9}	2.28×10^{2}
80	8.9×10^{13}	10^{8}	1.19×10^{3}

The three absorption bands in the near ultraviolet and visible regions of the spectrum are all suitable for use in atmospheric absorption studies and have been used for this purpose. The Dobson spectrophotometer, which is used to obtain values of total ozone, takes advantage of the rapidly changing absorption cross section with wavelength that is characteristic of Huggins bands. Solar radiation, either direct or scattered, is measured at two close wavelengths such that the intensity at the top of the atmosphere is almost the same but the absorption due to ozone is very different. The structure of the Huggins absorption bands as determined by Inn and Tanaka (1959) is shown in Figure 2.3.

Two features of the Huggins bands made them unsuitable for use in the type of system that was to be used in this study.

(a) The cross section is too small to clearly define structure above the maximum concentration region within the expectation of the equipment, including telemetry.

(b) The cross section, particularly in the minima of the band structure has been found to be temperature dependent in a study by Vassy (1937).

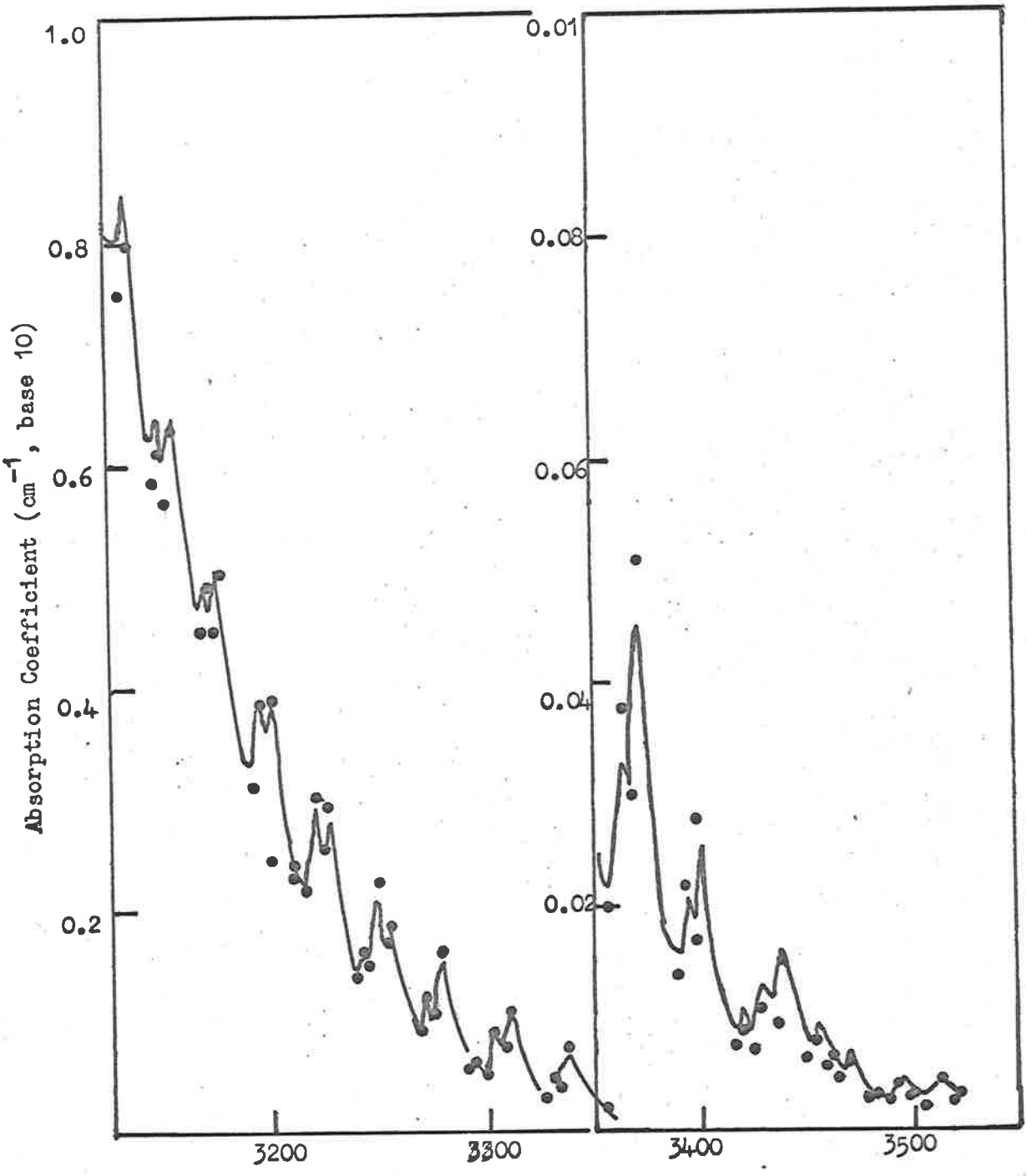

Figure 2.3 The Huggins absorption bands. The curves show the values of Inn and Tanaka while the points are those of Vigroux. After Inn and Tanaka 1953.

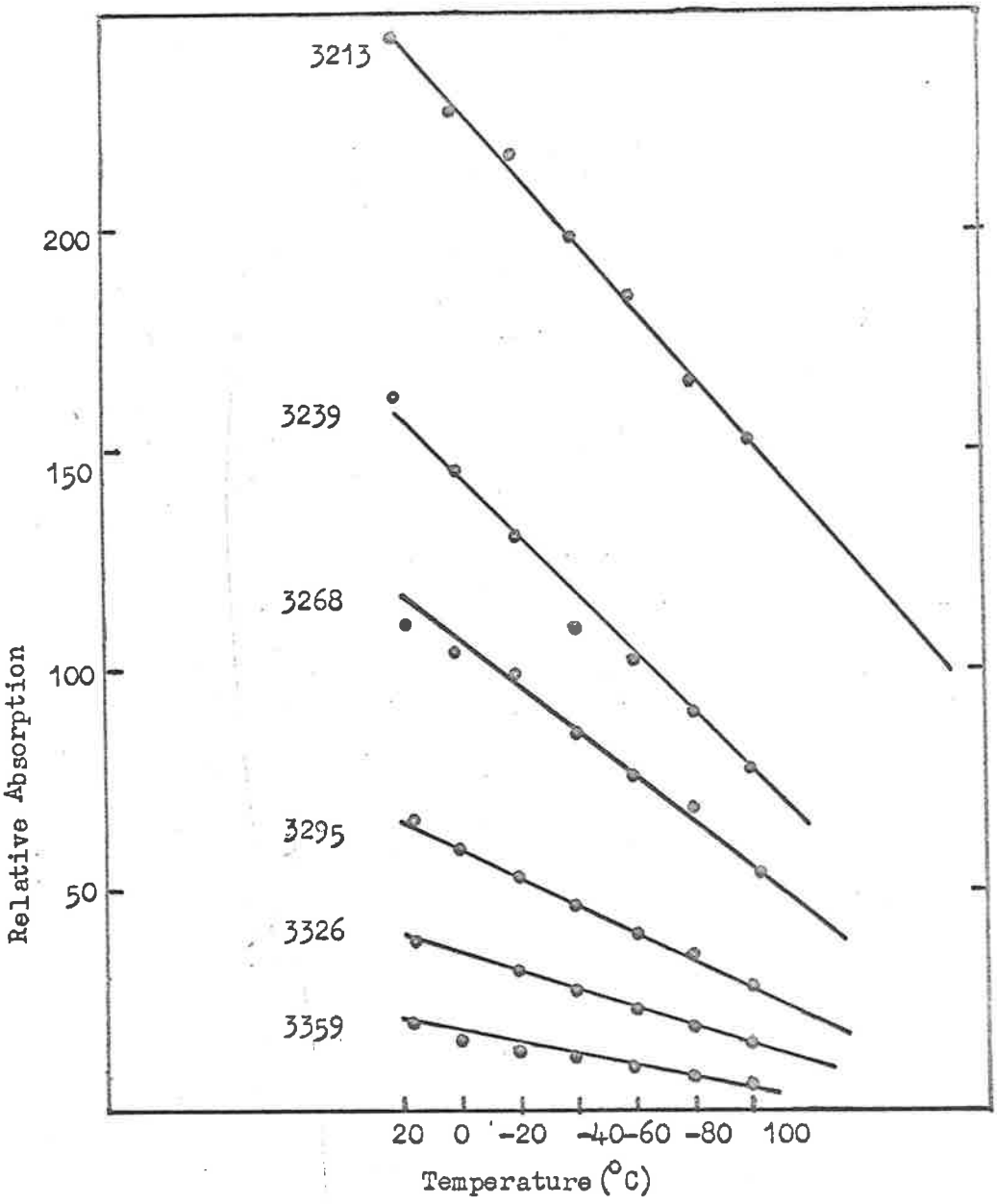

Figure 214 Variation of absorption in the minima of the Huggins Absorption Bands as a function of Temperature. After Vassy 1937.

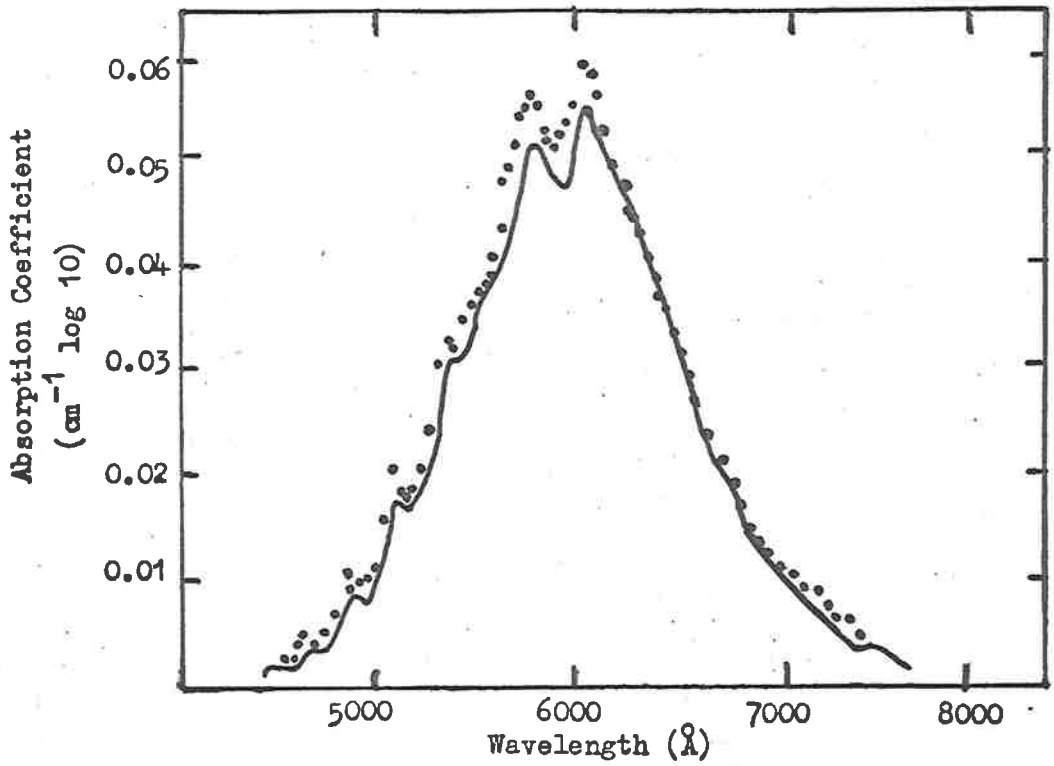

Figure 2.5 The structure of the Chappius absorption bands. The points shown are by Vigroux and the curve by Inn and Tanaka. After Inn and Tanaka 1953.

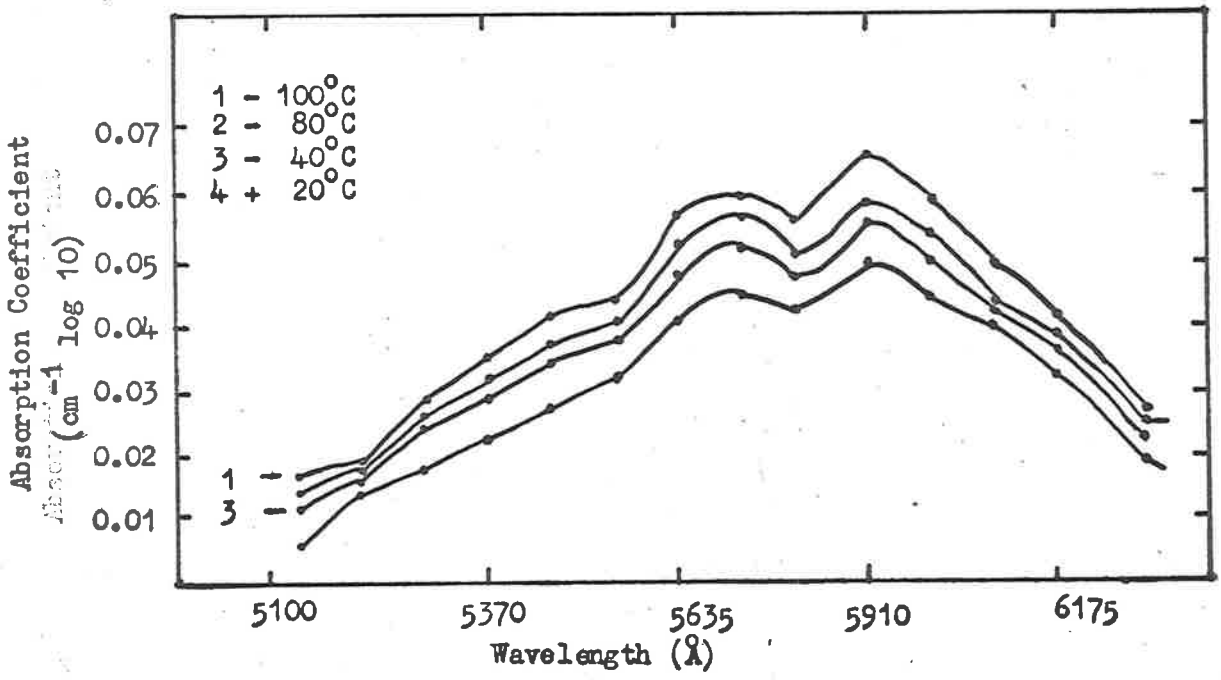

Figure 2.6 Variation of absorption in the Chappius bands with temperature. After Vassy 1937.

Some results of the temperature dependence study by Vassy are shown in Figure 2.4. Due to the uncertainty existing in the structure of the temperature vs. height profile at any particular moment, a temperature sensitive cross section is not suitable for use in atmospheric absorption measures.

The study by Vassy also showed temperature dependence in the Chappuis absorption bands, which, for the same reasons as stated previously, were not used in the investigation. The structure of the Chappuis bands from Inn and Tanaka (1959) and the temperature dependence from Vassy (1937) are shown in Figures 2.5 and 2.6 respectively.

The Hartley absorption bands, when studied by Vassy, over the range 2700Å to 3000Å, showed no temperature effect when observed over the range 0, -20, -40, -60 and -80°C, the spectrophotometric curves being superposable. The variation of the cross section with wavelength is shown in Figure 1.4. It can be seen from this curve that the Hartley bands provided absorption coefficients suitable for both the measurements of ozone in the regions near the maximum at about 30 kilometers and the regions of low

density extending above 50 kilometers.

To give the best coverage of the height distribution, pass bands centred on 2400Å, 2700Å and 2900Å were chosen for the first set of instrumentation and a further band, centred on 2500Å was included in the second round.

As the spectrometric method tc be used was a broad band system, the width of the band being dependent upon both the spectral response of the photodetector and the spectral resolution of the filters used, the actual value of absorption coefficient used was a weighted mean value. The method of obtaining this mean value will be given in detail in Section 6.2.

2.10 The Full Moon as a Radiation Source

Use of the method of absorption in the determination of atmospheric densities requires a source of radiation, preferably of constant intensity and at some distance from the absorbing region. A suitably bright source in the night sky is the full moon. As the measurements were to be made in the middle ultraviolet, information

as to the intensity in this part of the spectum was required. Few studies have been made of the spectral intensity of the total lunar surface. Stair and Johnston (1953), produced results showing the total lunar surface spectrum down to a wavelength of 3300Å in the near ultraviolet while Heddle (1962) made an observation of the intensity at a wavelength near 2200Å. The results of Stair and Johnston and Heddle were combined by Heddle (1963) as a measure of the difference in brightness as a function of wavelength, between the sun and the full moon, and thus, a measure of the spectral reflectance of the lunar surface. A graph showing the magnitude difference, as given by Heddle, is given in Figure 2.7.

From the results of Heddle, the flux expected from the total lunar surface was of the order of 10^{-5} to 10^{-6} ergs $cm^{-2} sec^{-1} Å^{-1}$ over the range of wavelengths to be used. This expected flux figure set the level of sensitivity of the photometers required and the experiments were planned to be flown at a period near to full moon. The difference in intensity between the sun and the reflected radiation from the moon was so large that a moonlit atmosphere would show no characteristic of a sunlit atmosphere and be representative of the atmosphere in the absence of radiation within the accuracy of the measurements to be made.

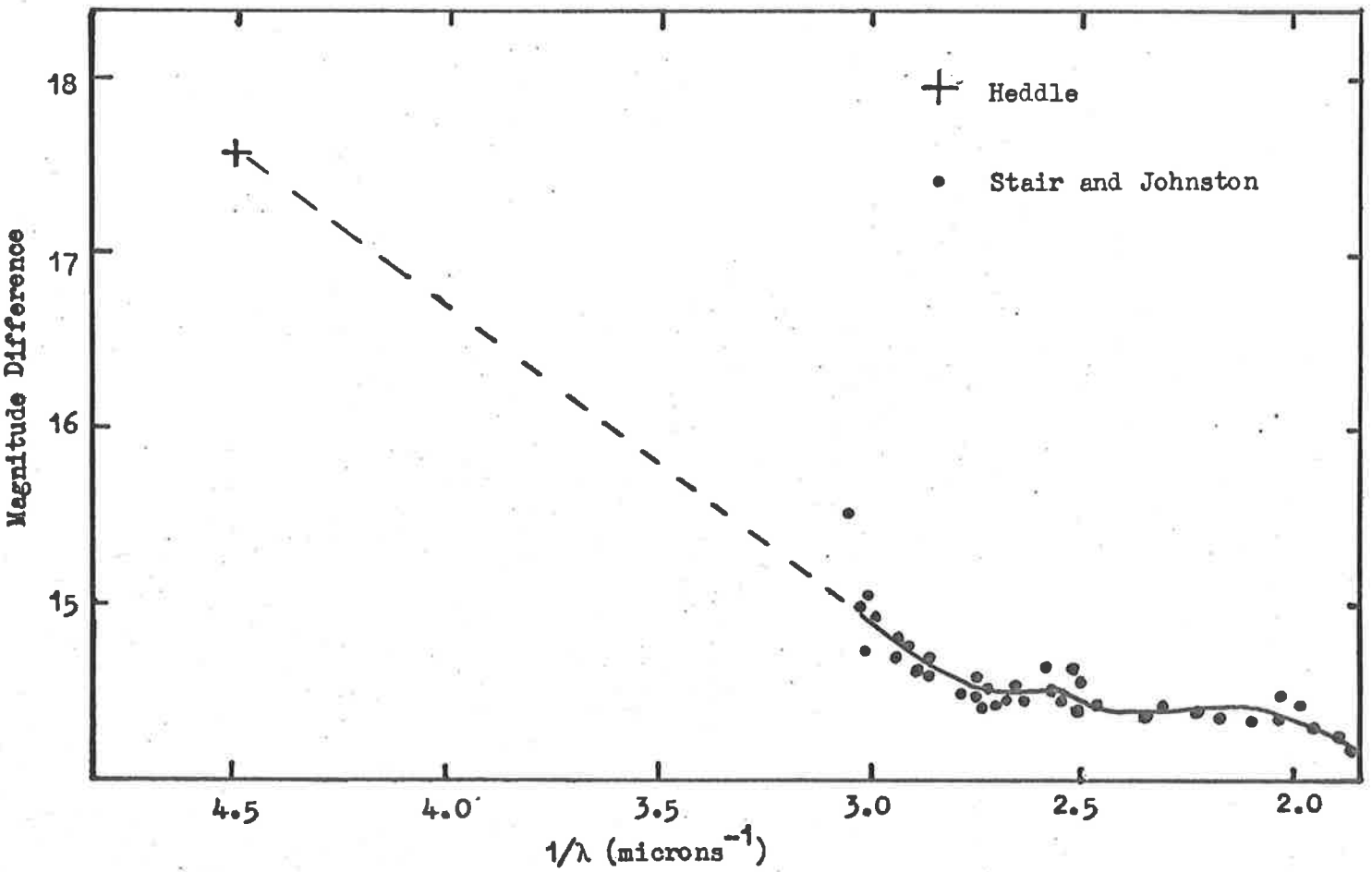

Figure 2.7 The Lunar–Solar magnitude difference. After Heddle 1963

CHAPTER 3

INSTRUMENTATION OF THE ROCKET VEHICLES

3.1 Introduction

The experimental apparatus employed in the rocket borne measurement of the lunar ultraviolet flux, and hence, the night time distribution of high atmospheric ozone, consisted of thin film filters backed by photoelectric sensors. The currents received from these were then passed through amplifiers, the voltages produced applied to a telemetry system and transmitted from the vehicle to the ground receiving station and recorded. Details of each item of the equipment are given below.

3.2 Photometers

3.2.1 Filters. Transmission and use in Photometers

The spectral resolution of the photometers was defined by the use of interference filters, which were obtained commercially and had nominal peak wavelengths of 2500Å, 2700Å, and 2900Å. The transmission of each

filter was measured, using a Perkin Elmer Type 137UV Ultraviolet-Visible Spectrophotometer. Graphs of Log Absorbance vs. Wavelength, as produced by this instrument, are given in Figures 3.1.1, 3.1.2, 3.1.3 and 3.1.4.

Although the commercial process employed by the suppliers is not known, the general procedure used in the making of interference filters for use in the middle ultraviolet has become well known in the last ten years, e.g. Schroeder (1962), Soklova and Krylova (1959) and Barr and Jenkins (1956). One of the problems associated with interference filters is the transmission of lower order passbands of longer wavelengths. Such an effect was noticable in the filters supplied with nominal wavelength peak transmission at 2500Å, but had been suppressed to the extent that transmission at the lower order peak at 5000Å gave a signal, from the complete photometer, only slightly above noise level, when exposed to full moonlight at ground level. In the case of the other filters supplied, the lower order transmission was removed by use of ultraviolet transmitting glass filters of the type of Corning 7-54.

The simple theory of interference filters has the form, for maximum transmission, of

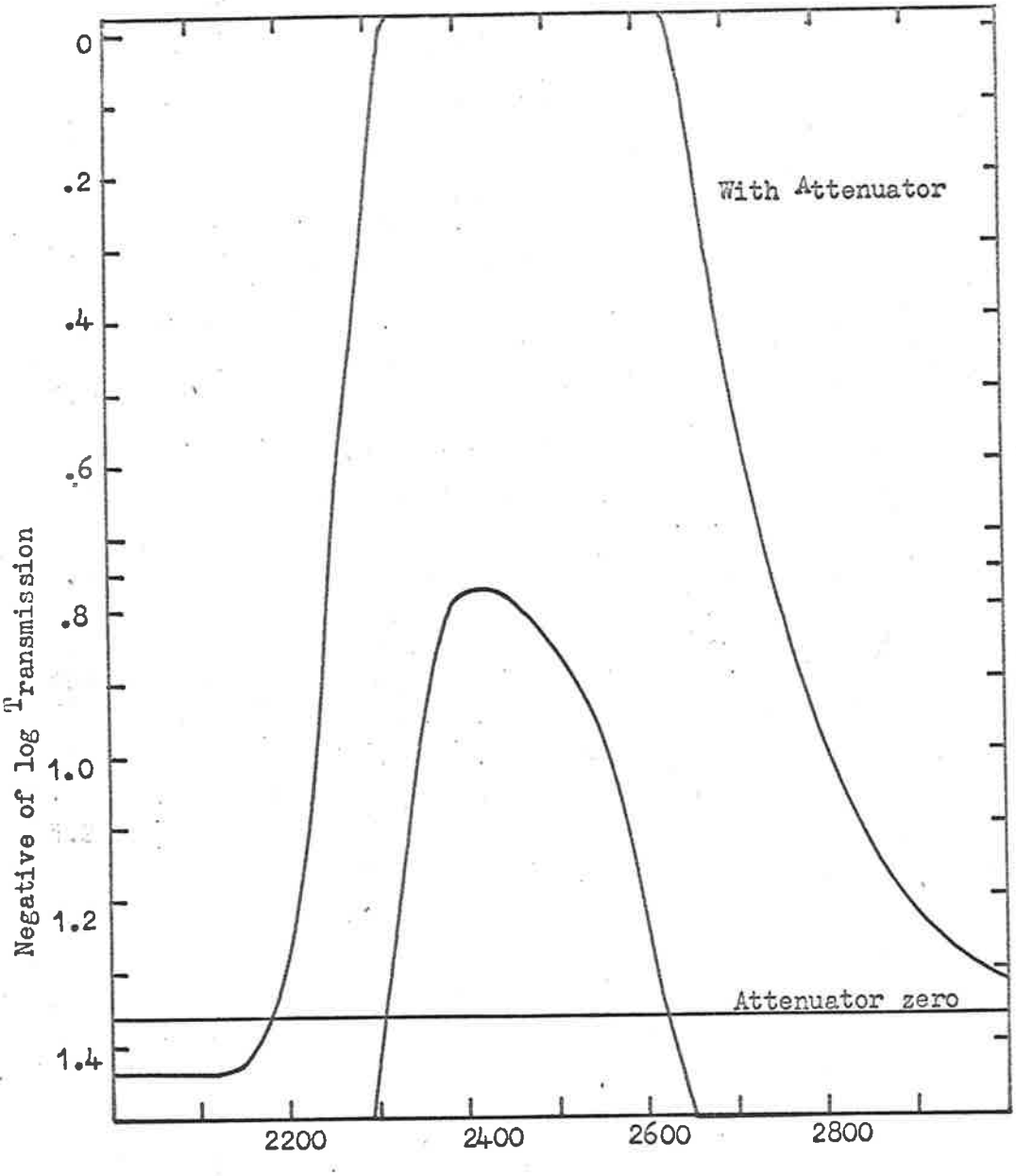

Figure 3.1.1 Transmission of filter at 2400Å. The value of the curve with attenuator should be added to the value of the attenuator.

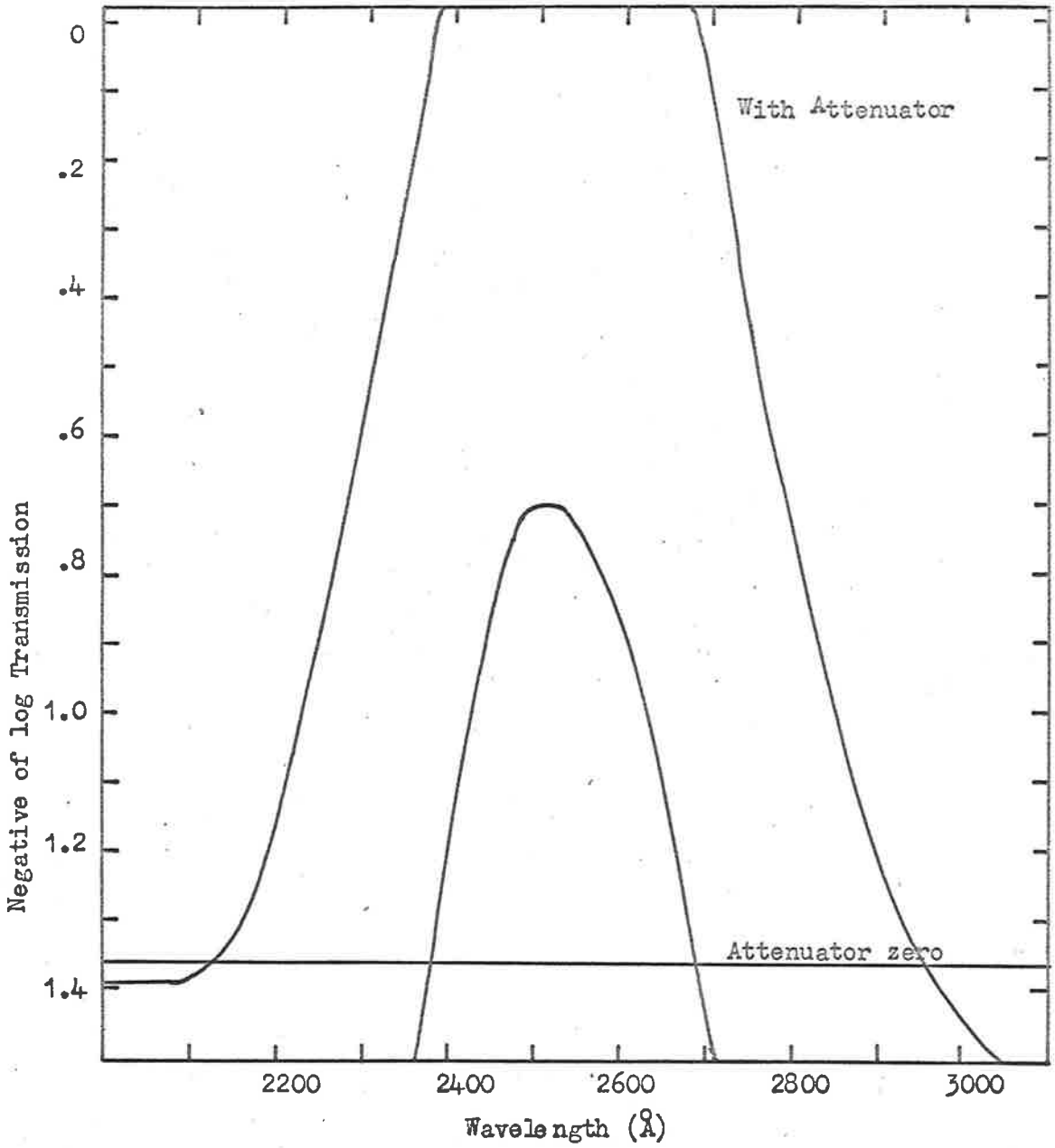

Figure 3.1.2 Transmission of filter at 2500Å. The value of the curve with attenuator should be added to the value of the attenuator zero.

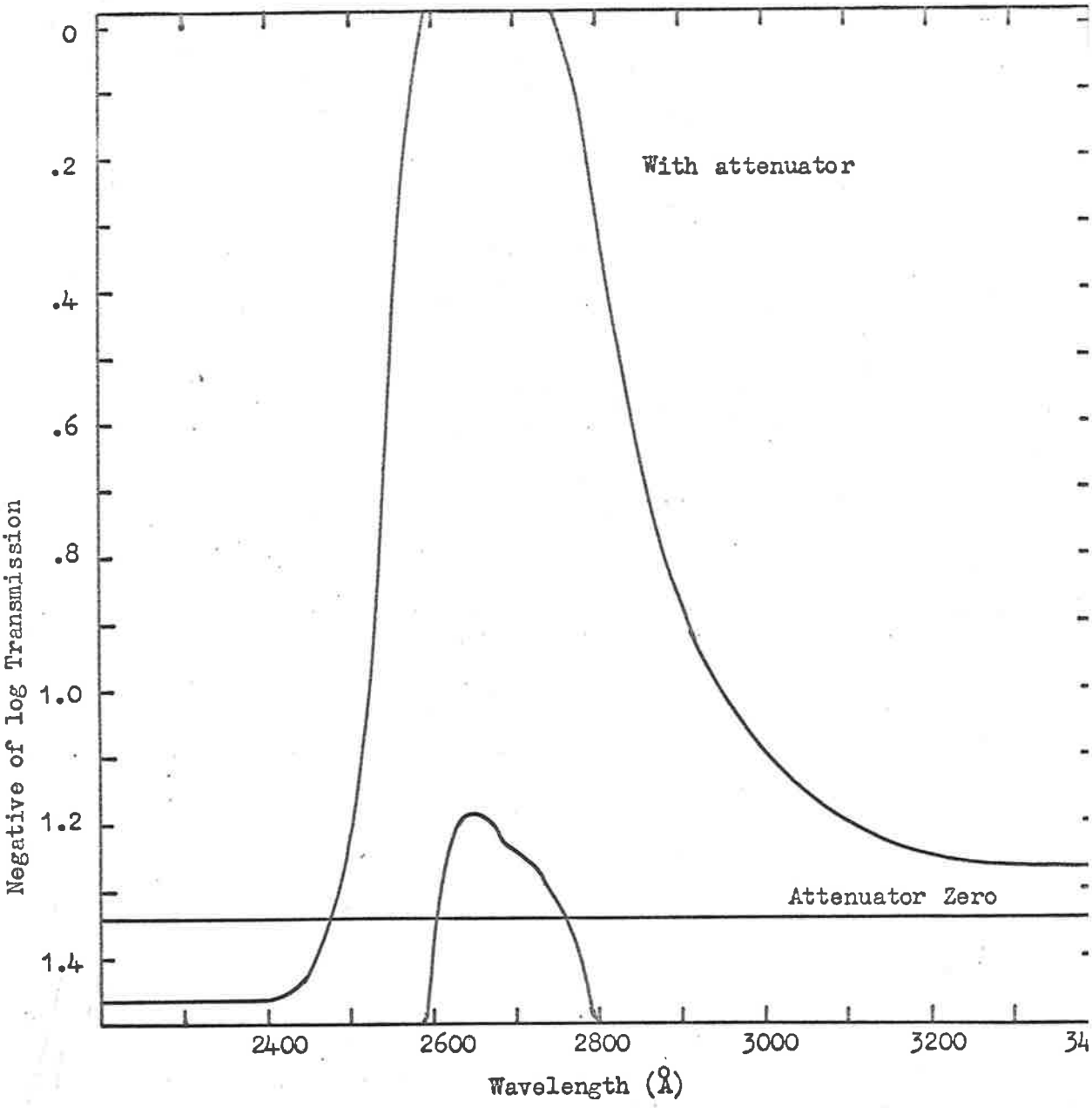

Figure 3.1.3 Transmission of filter at 2700Å. The value of the curv with attenuator should be added to the value of the attenuator zero.

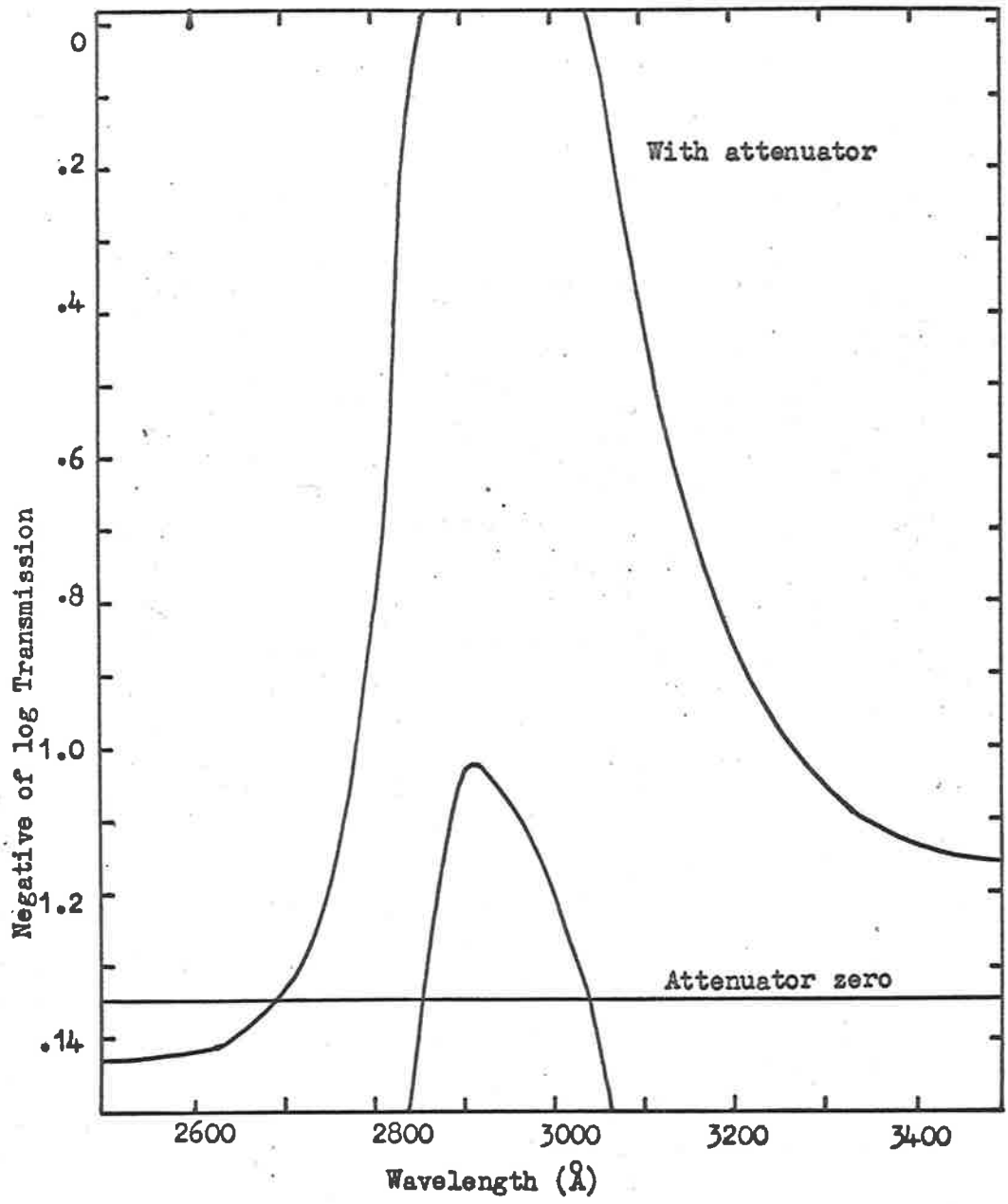

Figure 3.1.4 Transmission of filter at 2900Å. The value of the curve with attenuator should be added to the value of the attenuator zero.

$$2\mu d \cos\theta = n\lambda$$

where μ = refractive index of the transmitting medium

d = thickness of the film of the medium

θ = angle of incidence of the radiation

n = an integer, low for such filters

and λ = the wavelength of maximum transmission.

The dependence on θ of the transmitted wavelength was also observed, using the same spectrophotometer as mentioned above. The results for a typical filter are shown in Figure 3.2. It may be seen that, while the beam of the spectrophotometer is slightly divergent, with a half angle of 3.5°, this has no practical effect on the transmission measured at normal incidence, though some effect could be expected when measurements were made at large angles. The curves in Figure 3.2 were not critical to the experiment but serve to explain the change in wavelength sensitivity with angle observed in calibration of the final photometer.

The mountings for the filters in the flight vehicle consisted of shallow flanged cylinders, the filters being held in place by screwed retaining rings. Protection from shock was provided by neoprene O-rings,

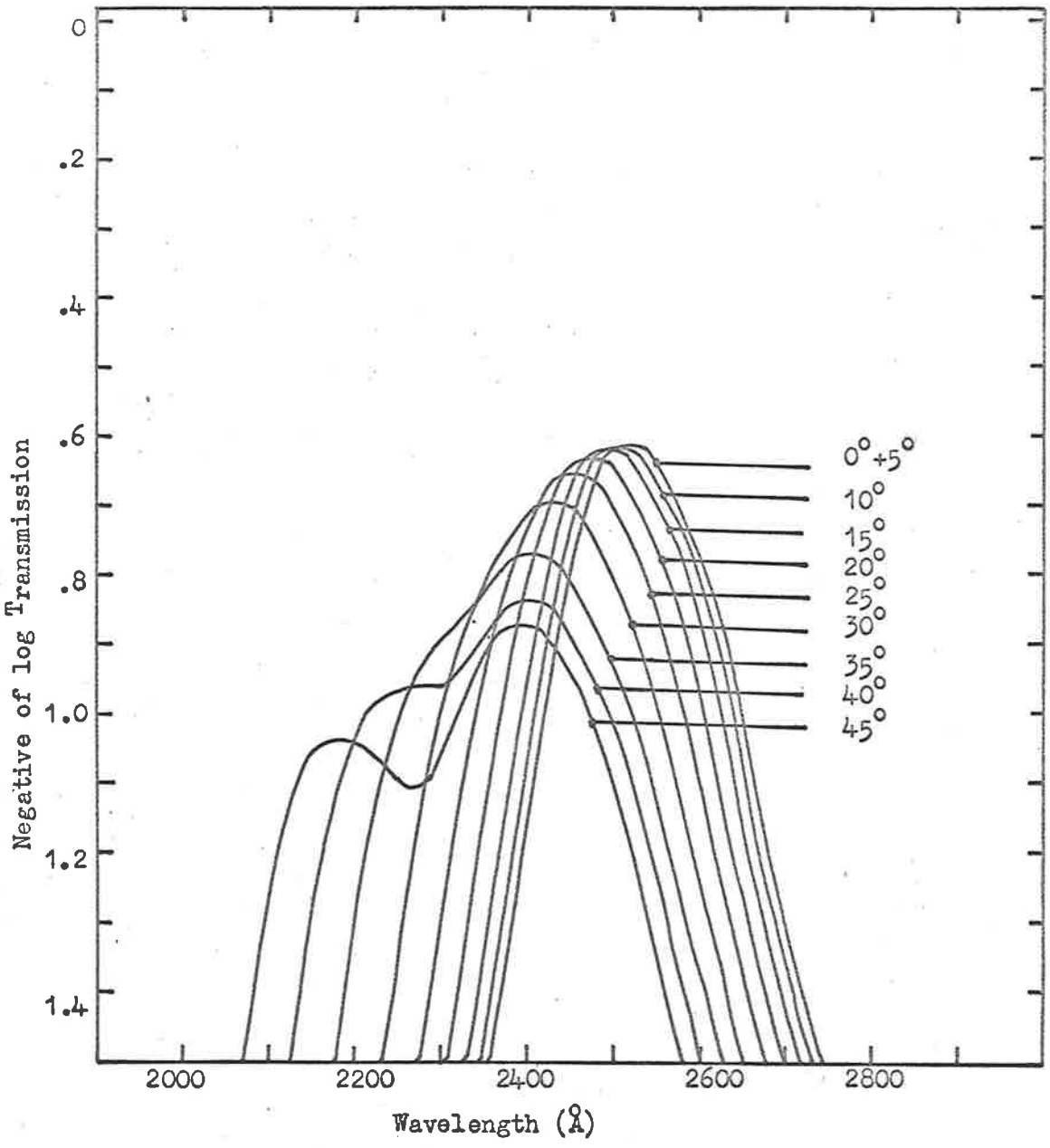

Figure 3.2 Variation with angle of incidence of the pass band of an interference filter centred on 2500Å.

Figure 3.3 Filter mounting used on HADs 305 and 312.

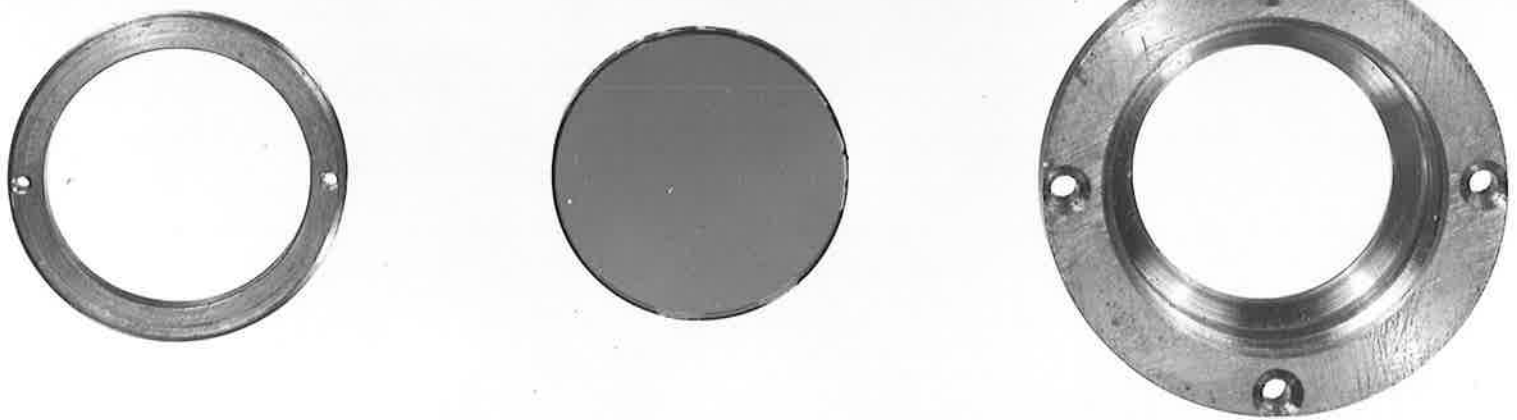

which also served as light seals. The mounting is shown in Figure 3.3.

3.2.2 Photomultiplier Type and Mounting

The photomultipliers used were R.C.A. Type 1P28. The 1P28 is a side window tube of circular cage dynode structure, with a Cs - Sb cathode and an envelope of Corning 9741 glass which is capable of transmitting ultraviolet.

The choice of this photomultiplier was determined by the combination of its spectral response and its size. Upon removal of base pin structure, the tube has an overall length of about $3\frac{1}{8}$ inches, this varying slightly, depending on the shape of the sealed off pumping lead at the base. The envelope has a maximum diameter of 1 5/16 inches. This dimension is maintained from the top of the envelope for 2 inches. From this point on, the diameter decreases so as to fall inside a straight line from this point to the tip of the pumping lead. This shape enabled the mounting of the tube inside the payload diameter of $4\frac{1}{2}$ inches. The position and shape of the mounting is shown in the layout diagram, Figure 3.6.1.

3.2.3 Requirement and method of A.C. Modulation of Photomultipliers

The thermal environment of the rocket, involving high temperature excursions, is such that drift of the output level associated with zero input current can occur in solid state D.C. amplifiers. Because of this, an A.C. system was used in preference to D.C. To obtain this A.C. condition of output current from the photomultipliers, the signal was modulated by changing the gain of the tube in a periodic fashion. This was done by shifting the potential of one of the dynodes with respect to the value that would exist in a normal D.C. chain.

In order to determine the magnitude and sign of this shift and which dynode was the most suitable to shift to obtain the desired effect, tests were made on dynodes numbers 4, 5, 6 and 7. These were made by adjusting a light source to give a convenient output signal at three operating voltages and varying the potential of the dynode with respect to its normal chain position voltage. The resulting curves are shown in Figures 3.4.1, 3.4.2, 3.4.3 and 3.4.4. It can be seen that dynode number 6, varying negatively gave the sharpest cut off of signal. For this reason, dynode number

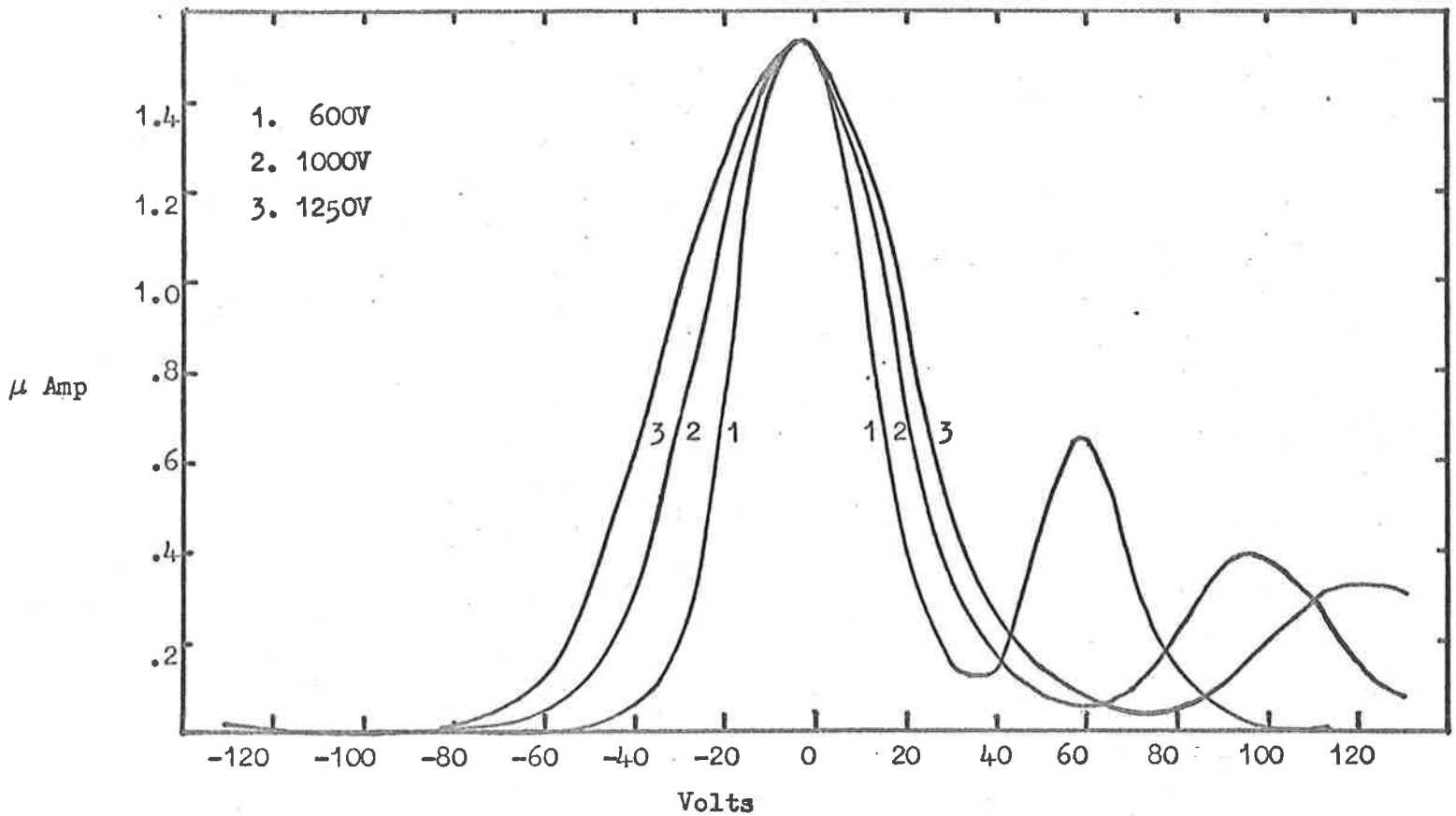

Figure 3.4.1 Variation of signal current as Dynode 4 of a 1P28 is changed in potential with respect to the value fixed for its position on a normal resistor chain. Curves 1, 2 and 3 refer to the total voltage applied across the resistor chain.

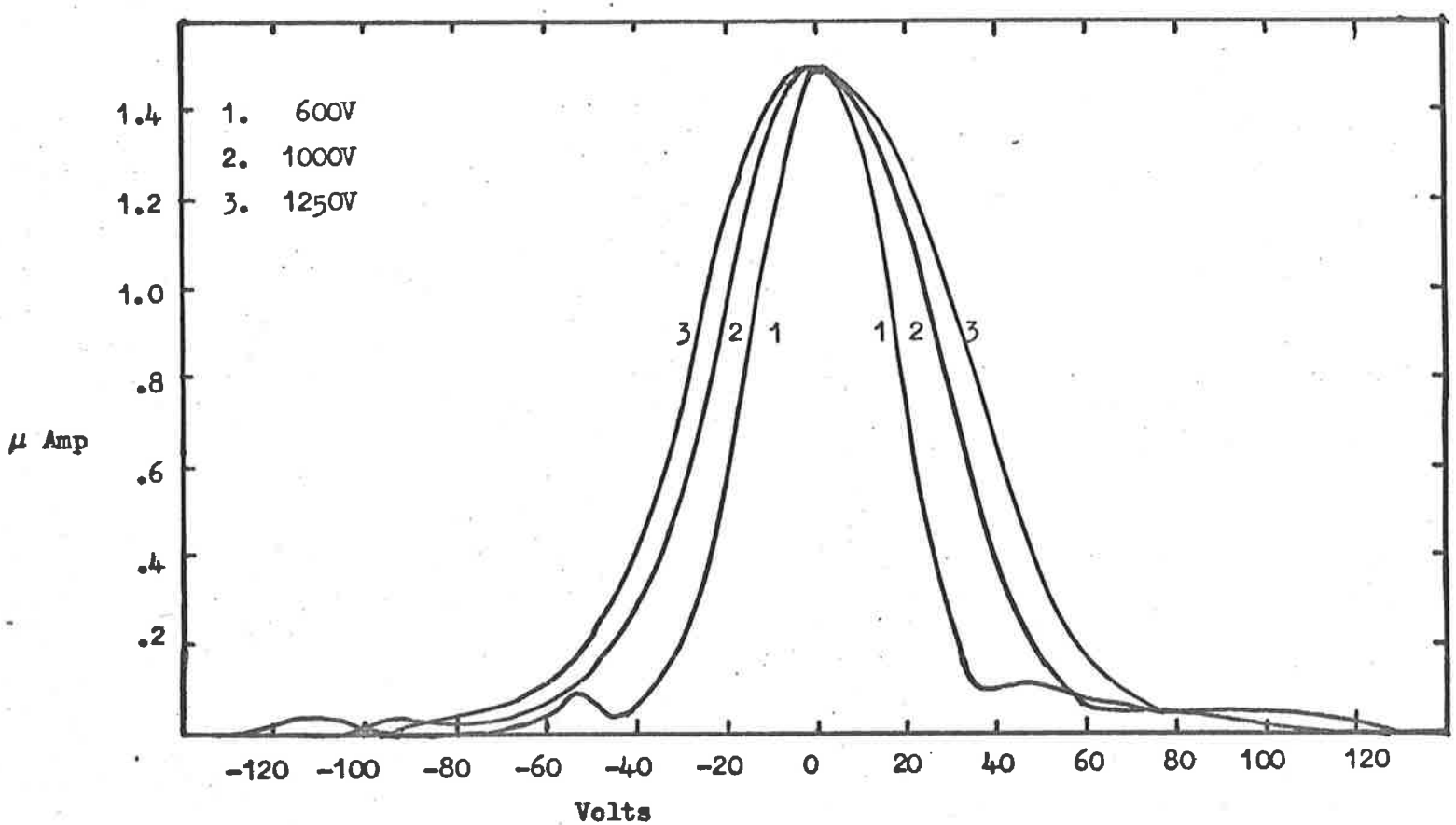

Figure 3.4.2 Variation of signal current as Dynode 5 of a 1P28 is changed in potential with respect to the value fixed for its position on a normal resistor chain. Curves 1, 2 and 3 refer to the total voltage applied across the resistor chain.

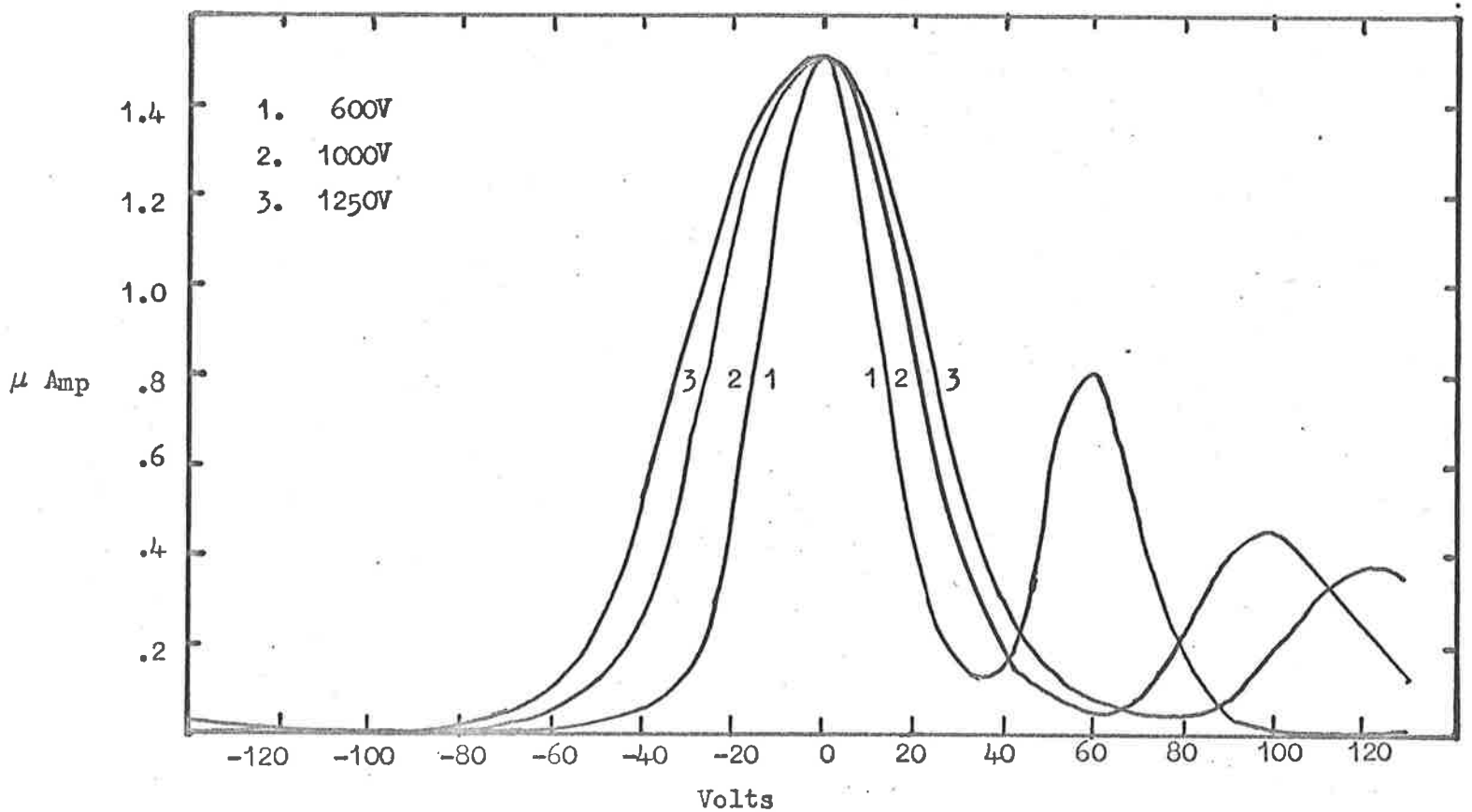

Figure 3.4.3 Variation of signal current as Dynode 6 of a 1P28 is changed in potential with respect to the value fixed for its position on a normal resistor chain. Curves 1, 2 and 3 refer to the total voltage applied across the resistor chain.

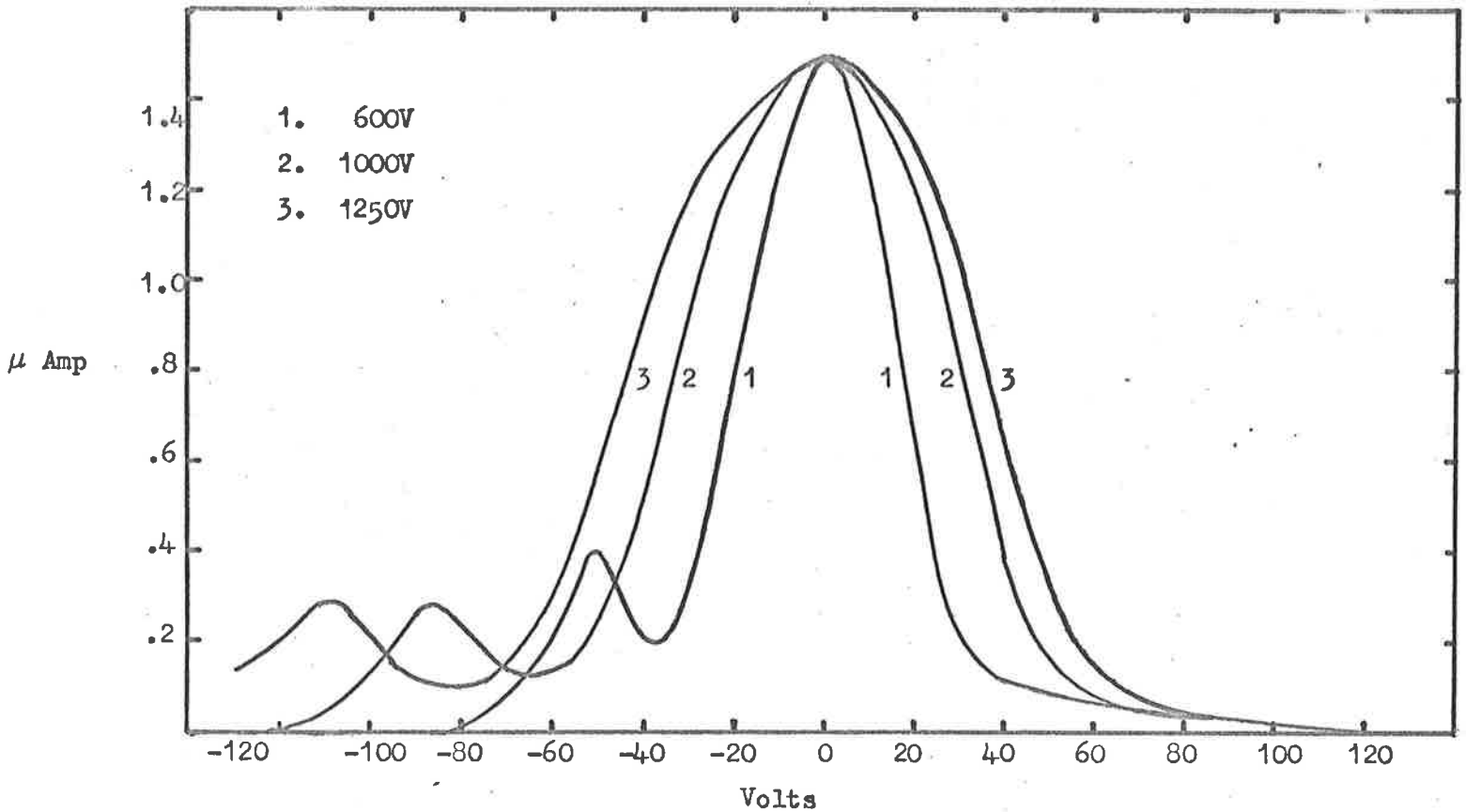

Figure 3.4.4 Variation of signal current as Dynode 7 of a 1P28 is changed in potential with respect to the value fixed for its position on a normal resistor chain. Curves 1, 2 and 3 refer to the total voltage applied across the resistor chain.

6 was chosen as the most suitable. The method of producing the required shift of potential from a supplied square wave is shown in Figure 3.5.

3.3. Electronics

3.3.1 Dynode Modulation

The square wave supplied to dynode number 6 comes from the unsmoothed output of a D.C. converter operating at a frequency of 1.2 Kc/s, with a peak to peak voltage at the output of 100 volts for an input of -15 volts. Details of circuit operation and a circuit diagram are given in Appendix 1.

3.3.2 High Tension Supply

The high tension voltage, necessary for the operation of photomultipliers, is supplied from a D.C. to D.C. converter. The potential developed is dropped across the five resistor chains which supply the dynode potentials to the five tubes used. The magnitude of the resistors used in the chains must be balanced between two demands. The first of these

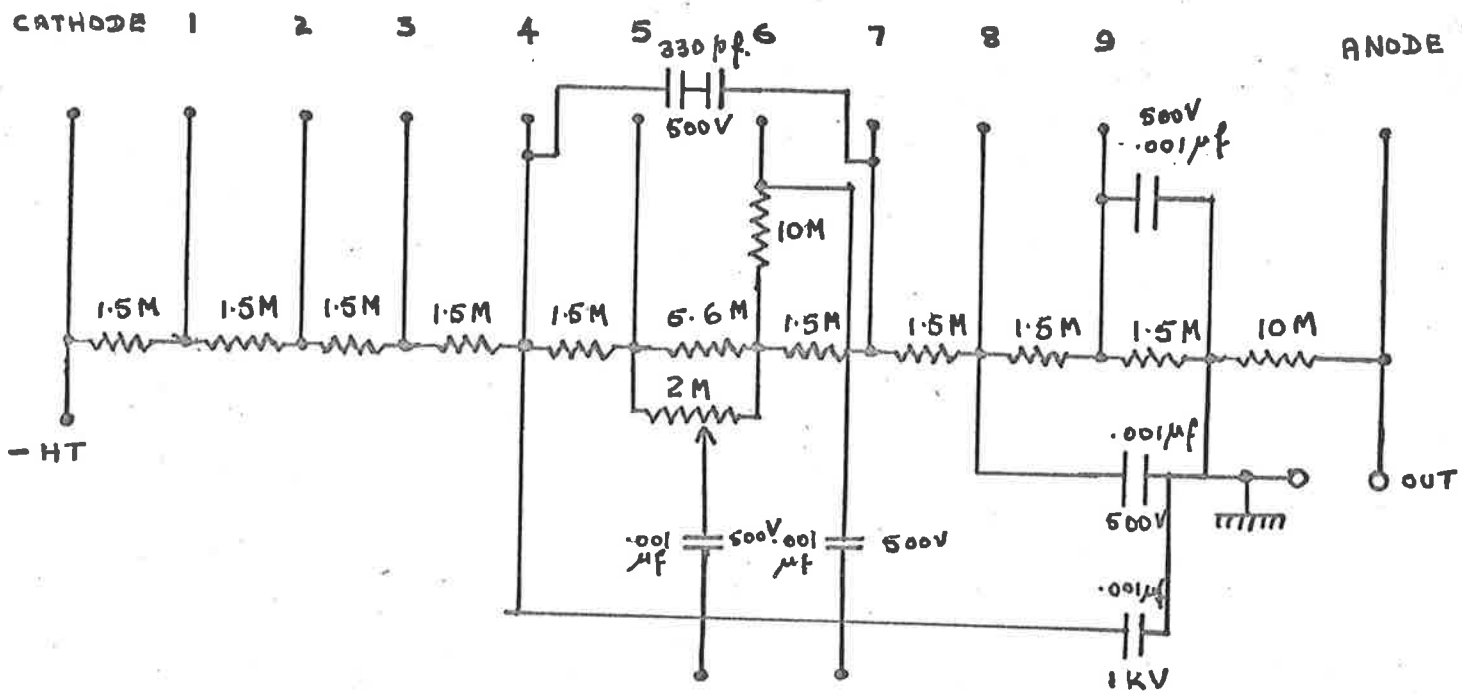

Figure 3.5 Dynode chain with facility for dynode modulation.

is that the chain current in each photomultiplier system must be between one and two orders of magnitude greater than the signal current while the second is that the power dissipated is within the tolerances of the transistors used, the types used being limited by the dimensions allowable for rocket application. These conditions were controlled by variation of the applied potential, by use of a dropping resistor between the supply and the resistor chains, and adjustment of the amplifier gain. This method can be used as the signal current has an exponential dependence on the applied voltage while the dependence of the chain current is linear. The circuit diagram and description of operation is given in Appendix 2.

3.3.3 Amplifiers

The amplifiers to which the output currentsof the photomultipliers were applied had three outputs. The gain of the first stage of each amplifier was variable by adjustment of the input impedance while each of the two succeeding stages had a gain of 10. Each stage had its own output which was monitored by the telemetry system. The wide dynamic range of this system was necessary if details of the high level

absorption were to be obtained. This can be seen if it is assumed that the total column number density of ozone molecules above 30 kilometers if of order 10^{19} to 10^{20} molecules per cm^2 while the cross section is of order 10^{-17} cm^2 per particle, which implies that the signal would be expected to change by a factor of e^3 to e^4 during the flight, thus showing the need for a wide dynamic range of the photometers. Because of limitations imposed by the telemetry system used, all three outputs have a voltage limit of 1.5 volts. This limit prevented the sensor voltages being confused with the synchronised pulse of the telemetry frame. A circuit diagram of the amplifiers and a discussion of their operation is given in Appendix 3.

3.3.4 Calibration Circuits

Because of the possibility of change of gain due to the thermal environment, an in flight calibration system was devised. This consisted of two pairs of 'grain of wheat' lamps that were lit sequentially for a period of 200 milliseconds each eleven seconds. The lamps were arranged so that pair 1 illuminated tubes 1, 2, 3 and 4 while pair 2 illuminated tubes 2, 3, 4 and 5. It would thus be possible, on examination of the

recorded output, to note if any change was apparent in the signal from any one tube and by reference to an adjacent tube, determined if this was due to change in the gain of a particular photometer of a change in the level of illumination from a particular lamp. The voltage output for each calibration lamp was adjustable by variation of the depth of penetration of a screw into the light path between the lamp and the particular photometer. The position of the lamps with respect to the photometers is shown in Figure 3.6.2, while the circuit diagram and explanation of operation of the calibration timer and lamp supply is given in Appendix 4.

3.3.5 Protection against Dynode Vibration

During laboratory tests it was found that what appeared to be mechanical resonances of the dynode structure occurred at some frequencies during the vibration test. At certain frequencies, when the tube was vibrated with the high tension voltage applied, large pulses of current were observed followed by a considerable increase in the dark current level of the tube. When the tube was subjected to several traverses

of the vibration spectrum in the absence of high tension, no increase in the dark current was observed when the high voltage was again applied. To avert any unnecessary increase in dark current during the flight, the high tension was not applied until 26 seconds after ignition of the first stage motor. At this time the second stage motor has passed burnout and the vehicle is in free fall. The switch system which permitted this form of operation, as well as control for preflight checks is described, together with a circuit diagram in Appendix 5.

3.4 The Rocket Vehicle

The rocket used in these experiments is the HAD (High Altitude Density) vehicle designed by Flight Projects Group of Weapons Research Establishment, Australian Department of Supply. It is a two stage vehicle, both stages having solid fuel motors, both burning for approximately 3 seconds, burnout of the second stage occurring 24 seconds after launch at approximately 20 kilometers. The second stage is partially spin stabilised by the action of fins, but, as the ratio of moment of inertia about the longitud-

inal axis to that about an axis normal to it, is much less than unity, there is a tendency for precession of the longitudinal axis to occur during flight. This form of motion is advantageous overall as it allows change of aspect angle during flight almost completely eliminating the possibility of no observations of a particular source of small angular extent being made during the flight.

3.5 Distribution of the Payload

The instrumentation head is divided into four main sections which are listed below

a. Telemetry

b. Sensors

c. Acquisition aid

d. Firing and timing

and are shown in Figure 3.6.1.

Sections c and d will not be discussed in this survey as they are part of the rocket itself and are only associated with the firing of the vehicle and the subsequent tracking of the trajectory. The telemetry section, a W.R.E. 465 system, consisted of:

Figure 3.6.1 Distribution of the payload in HADs 305 and 312.

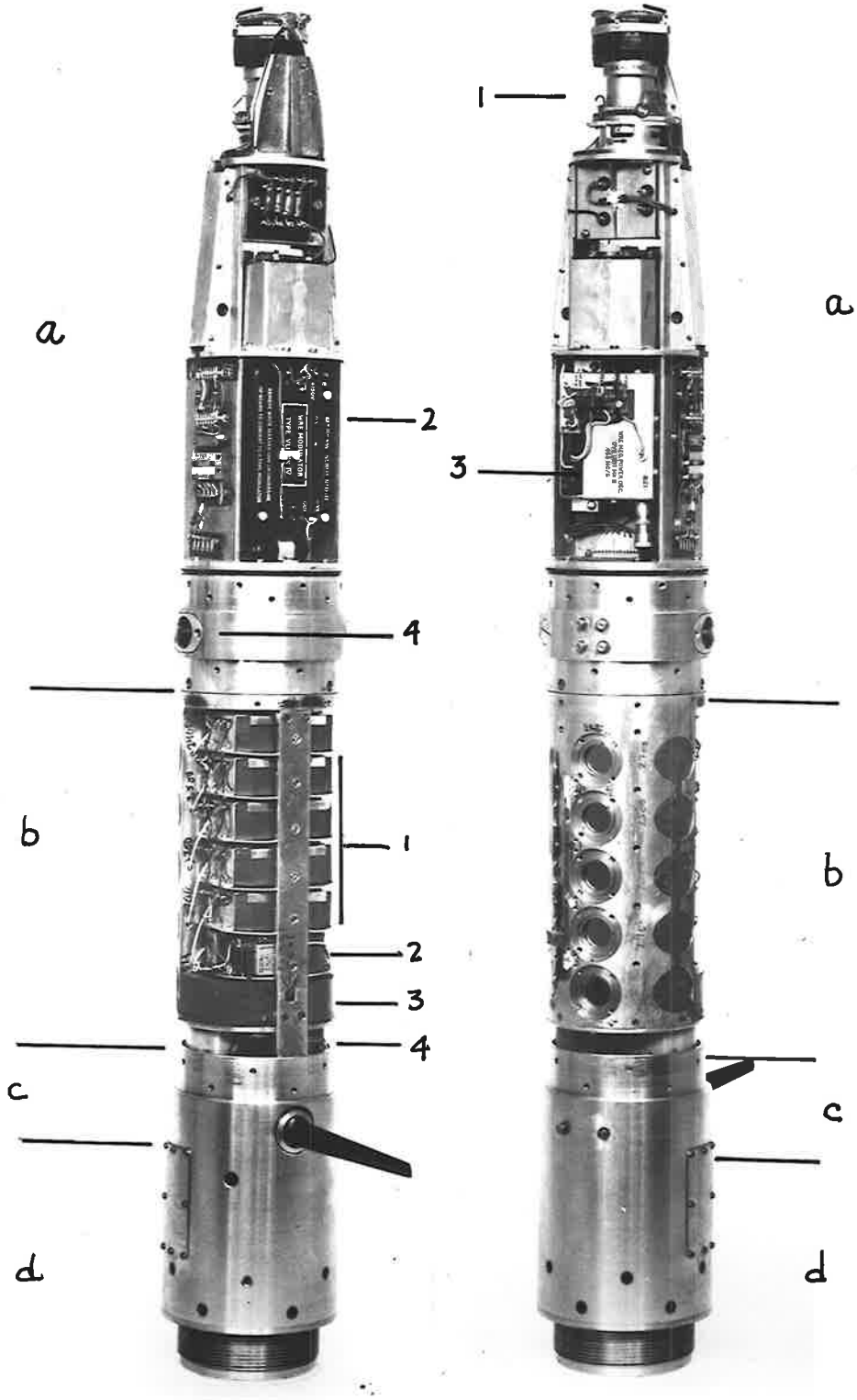
a
2
4
b
1
2
3
4
c
d
1
a
3
b
c
d

Figure 3.6.2 Filter mounts and positioning of photomultipliers in the payload.

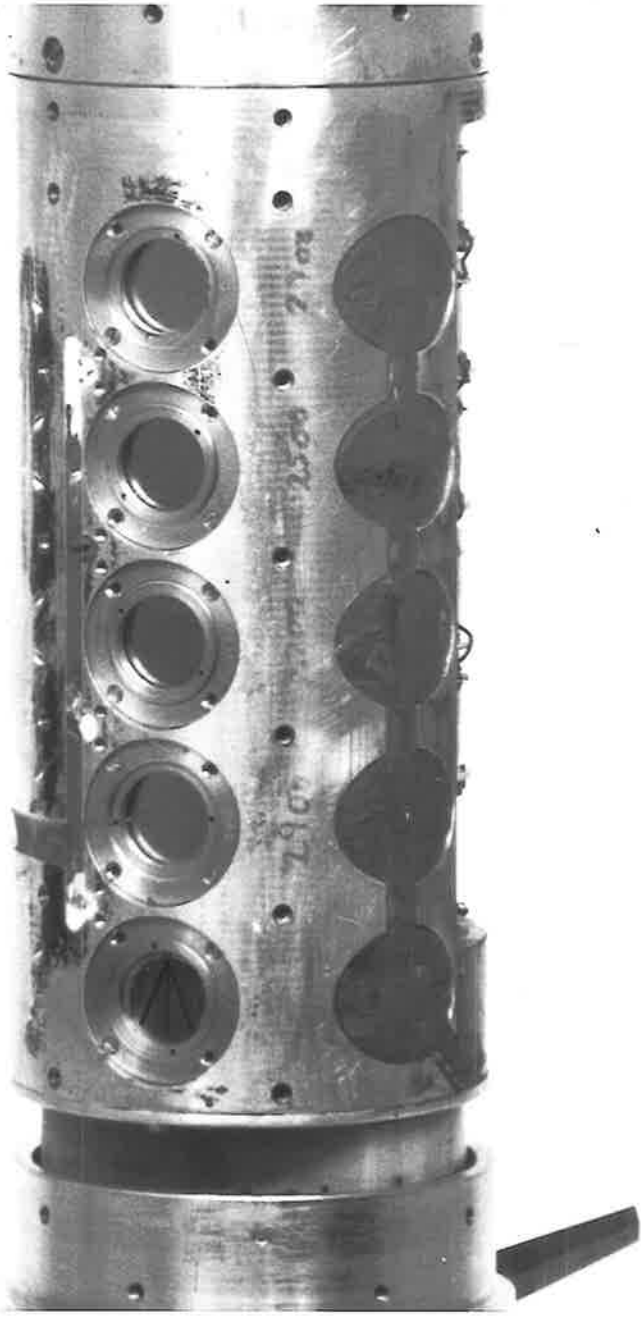

a.1 The switch motor which was a 24 pin head with a wiper arm, rotating at 80 rev/sec. The motor power was supplied by Venner silver-zinc accumulators. The voltages, from the sensor amplifiers and calibration points, which appear on each of the 24 pins were sampled in turn by the wiper arm and were applied to -

a.2 a voltage controlled oscillator, varying between 130 kc/s, and 160 kc/s as the applied voltage from the wiper arm varied between 0 volts and 1.5 volts. This frequency modulated signal then amplitude modulated -

a.3 a 465 Mc/s power oscillator which fed two quarter wave dipoles at section -

a.4 for transmission to a ground receiving station.

The section b contained the photomultiplier tubes, mounted across the section. to one side of the axis, such that the photocathodes were as close to the surface of the rocket as the length of the tube allowed. A filter mount was in front of each photocathode, screwed to the inner instrument casing. Figure 3.6.2 shows the layout of the filter mounts and positioning of the photomultiplier tubes. On the section of casing behind the photomultipliers were mounted the amplifiers, b1, switching circuits, b2, and the

dynode modulator and high tension supply, b3. All the power, necessary for the operation of the electronics associated with the sensors, is supplied by Eveready No. 912 dry cells, arranged in series and parallel, as required, to supply the necessary voltages and currents, as designated by the appendices relating to the circuitry. The battery pack is designated in the diagram as b4.

All electronics and photomultipliers were potted in Dow Corning Silastic 850 RTV Rubber. This material served two purposes, the first being electrical insulation and the second, protection from shock.

3.6 Preflight Checks for Equipment

Two main checks were made on the instrumentation prior to flight. The first of these consisted of placing the instrumentation section in a vacuum chamber, and reducing the pressure to a value of 10^{-3} torr. The pressure was allowed to leak slowly up to atmospheric, the electronic systems all operating from laboratory power supplies during this period, each power supply being monitored. If corona discharge had occurred during this period, it was known, from previous tests, that an obvious

change in the current drain of the supply to the high tension unit would take place, enabling detection and correction of such a fault. The second test consisted of a sensor and telemetry check. This required the facilities of the Weapons Research Establishment of the Department of Supply. The complete head, as shown in Figure 3.7 was operated and the telemetry received at a remote station. Signals appeared on the photometer channels, due to the operation of the calibration lamps, all voltage monitor channels were observed and checks made of the channel allocations and the efficiency of the voltage limiting circuits.

This latter check was also carried out as part of the immediate prelaunch sequence, using the actual range facilities.

Figure 3.7 Complete instrumentation head of an HAD rocket vehicle.

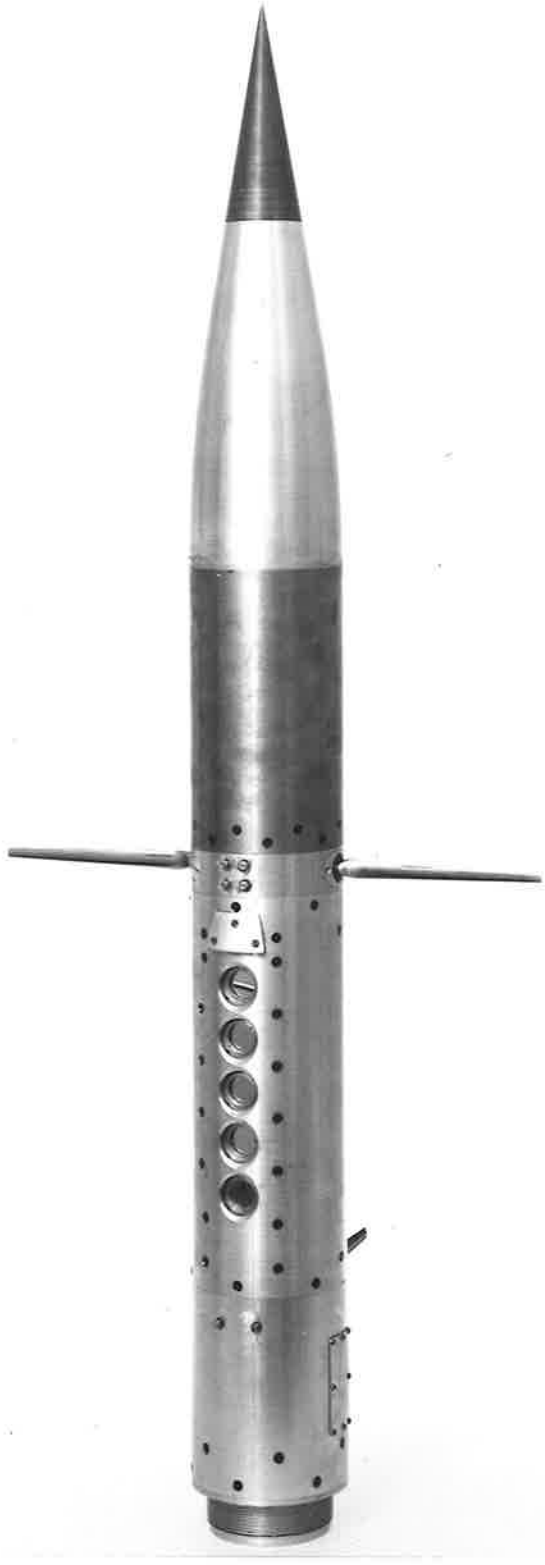

CHAPTER 4

CALIBRATION OF THE FLIGHT PHOTOMETERS

4.1 Introduction

As values of the ultraviolet flux, reflected from the lunar surface, were required, it was necessary to measure the absolute response of the sensors flown. The same basic method of calibration was used for the set of sensors carried in each rocket.

The method involves the use of sodium salicylate as a transfer detector from the region of Lyman α to the 2000Å to 3000Å range of the detectors. The light source used for the calibration was a Hydrogen capilliary discharge lamp, operated in the A.C. mode, mounted on a McPherson Vacuum Monochromator. Both $\frac{1}{2}$ metre and 1 metre instruments were used.

4.2 Experimental Method for Calibration of Sodium Salicylate

The first step was the calibration of the sodium salicylate. The experimental arrangement is shown in Figure 4.1. The sodium salicylate to be calibrated was deposited on a beam splitter (consisting of a mesh screen, set at 45° to the beam direction so that some of the incident radiation was passed while some was stopped) by spraying a saturated solution in methyl alcohol onto the mesh with a fine spray atomiser, the mesh being held in a warm air stream. The freshly coated beam splitter was then placed in position and the chamber, inwards from the lithium flouride window, evacuated to a pressure of 10^{-5} torr. These conditions were maintained for a period in excess of 24 hours. The lamp was run for short intervals during this period, in order to stabilise the salicylate layer. With the system as above, an ion chamber, filled with Nitric oxide and having a Lithium flouride window, was placed in the light path and the space between it and the window of the vacuum system flushed with oxygen-free nitrogen. A potential was applied to the centre wire of the chamber of 450 volts, thus operating the ion chamber at a gas gain figure of G, where

$$G = \frac{\text{Current for potential 450 Volts}}{\text{Current for potential 45 Volts (Unit gain)}}$$ for the

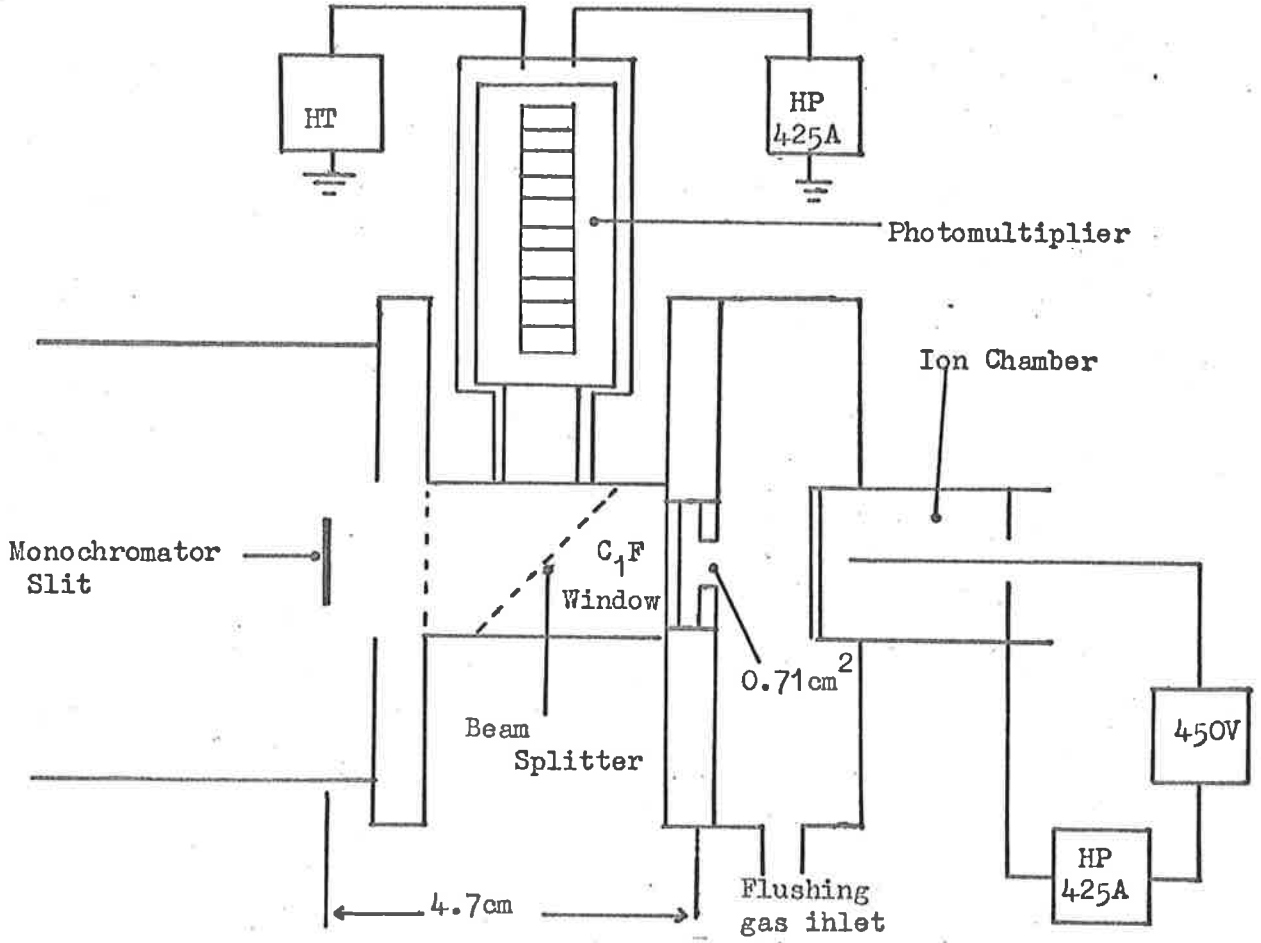

Figure 4.1 Experimental arrangement for the calibration of sodium salicylate beam splitter.

same intensity beam.

The photomultiplier viewing the beam splitter was operated at a voltage of 1400 volts, this value being maintained for the total period of operation of the tube during the calibration. The hydrogen lamp was then excited, the pressure of hydrogen being held at 5 millimetres of Hg, at which the line radiation of the discharge was found to be predominant. The wavelength at the exit slit was set at 1216Å.

The output currents of both the ion chamber and the photomultiplier were measured on Hewlett Packard Type 425A microvolt-ammeters. These currents are denoted by I_c and $I_{p\ 1216}$ respectively.

4.3 Theory of Sodium Salicylate Calibration

The quantum efficiency of an ion chamber is measured by comparison with a standard, parallel plate ion chamber set in the same beam while the gas gain figure is obtained by comparison of the currents obtained when the chamber has a potential of 45 volts, giving unit gain to the current obtained when the gas gain potential

is applied. If the quantum efficiency is q and the gas gain factor is G, then the total number of photons entering the ion chamber, through the diaphram, is given by

$$N_{1216} = I_c/Gqe \text{ photons/sec.} \qquad \ldots(1)$$

where e = electronic charge in coulombs.

The number of photons falling on the salicylate will be equal to this number, multiplied by some constant, say A, which is a function of the transmission of the beam splitter. The number reacting with the salicylate will be this number multiplied by the relative response of the salicylate at the wavelength of Lyman α, $SR_{L\alpha}$. The reaction of the salicylate was viewed by the photomultiplier which produced a current I_{p1216}, which depends, by a constant C on the number of phosphorescent photons produced.

$$\text{i.e.} \quad A\, SR_{L\alpha} I_c/Gqe = C\, I_{p1216} \qquad \ldots(2)$$

$$\text{i.e.} \quad N_{1216} = C/A.I_{p1216}/SR_{L\alpha} \qquad \ldots(3)$$

In general, at any wavelength λ, the number of photons passing through the diaphram, N_λ, is given by

$$N_\lambda = C/A.I_{p\lambda}/SR_\lambda \qquad \ldots(4)$$

where SR_λ is the relative response of sodium salicylate at wavelength λ. The value of the ratio C/A was obtained from the measured values at Lyman α.

$$\text{i.e.} \quad C/A = (I_c\ SR_{L\alpha})/(I_{p1216}{}^{Gqe}) \qquad \ldots(5)$$

From this relation, the number of photons per second at any wavelength, λ, is given by the relation

$$N_\lambda = (I_c\ SR_{L\alpha})/(I_{p1216}{}^{Gqe}).I_{p\lambda}/SR_\lambda \qquad \ldots(6)$$

Thus the number of photons passing through the diaphram was determined as a function of the current from the photomultiplier viewing the salicylate beam splitter.

4.4 Determination of Flux at Sensor

The sensor to be calibrated was mounted at a distance from the diaphram such that the beam spreads to a cross sectional area sufficient to illuminate the whole

of the aperture of the sensor. If this distance placed the sensor at a distance D_s centimeters from the slit of the monochromator, while the diaphram, of area A_d cm^2, was at a distance D_d centimeters from the slit, the number of photons reaching the sensor per cm^2 was

$$N_s \ cm^{-2} = (N_\lambda / A_d).(D_d/D_s)^2 \qquad ...(7)$$

The energy per unit area at the sensor was then given by the product of the number of photons per unit area and the energy per photon.

i.e. Energy per unit area = E cm^{-2} where

$$E \ cm^{-2} = (I_c \ SR_{L\alpha})/(I_{p1216} Gqe).(D_d/D_s)^2/A_d.hc \times I_{p\lambda}/SR_\lambda \lambda$$

$$= F.I_{p\lambda}/SR_\lambda \lambda.$$

where $F = (I_c \ SR_{L\alpha})/(I_{p1216} Gqe).(D_d/D_s)^2/A_d.hc$

h = Plancks constant

c = Speed of light

and λ = Wavelength of the photons.

4.5 Calibration of HAD 305

The sensors, mounted in the rocket body, were placed at the opening of the tube as defined by the length D_s. Laboratory power supplies were connected to the instrumentation, set at the values fixed at the battery outputs in the actual flight system. The output pin of the selected stage of the sensor amplifier was connected to one Hewlett Packard type 425A microvolt ammeter set in the voltage mode, while the current output of the photomultiplier was fed to a second Hewlett Packard, set in the current mode.

The monochromator lamp was then activated and high voltage applied to the photomultiplier. With the wavelength at the exit slit set to a value below any response of the detector, the background levels were measured, with the flap valve to the monochromator first closed then open to assure that this region was outside the sensitivity range of the sensor. The wavelength of the radiation at the exit slit was then varied in 10Å steps across the whole acceptance band of the detector, the photomultiplier current and voltage output being recorded at each step. The information was tabulated under the headings Wavelength, Monitor Photomultiplier Current, Sensor Output Volts together with details of the widths

of the entrance and exit slits. Each 20th reading was made with the flap valve closed to monitor any zero drift during the calibration. The maximum photomultiplier current drift during calibration was 1.2×10^{-9} amps while the zero drift of the sensor outputs was as listed

Detector	Dark Signal	Drift	Half Peak Signal
2400Å	6.0 mV	1.5 mV	496 mV
2700Å	7.0 mV	0.1 mV	250 mV
2900Å	8.5 mV	0.6 mV	255 mV

The dark signal appearing on each sensor output was largely due to radiated noise from the dynode modulation system.

4.6 Reduction of Measurements

The corrected values for voltage from the sensor and current from the photomultiplier were obtained by subtraction of the dark signal values. Let these be $V_o(\lambda)$ and $I_o(\lambda)$ respectively, at wavelength λ. The ratio, $V_o(\lambda)/I_o(\lambda) = R(\lambda)$, was then calculated for each wavelength recorded. The quantity $S(\lambda)$, being the

voltage out of the amplifier per unit energy flux incident on the sensor over the wavelength interval defined by the slit width used, was then defined by the relation:

$$S(\lambda) = \frac{R(\lambda).SR(\lambda).\lambda}{F} \qquad \ldots(9)$$

where the value of F is defined in equation (8).

The integral of the function $S(\lambda)$ with respect to λ was obtained by graphical methods, this integral being the sensitivity of the sensor in volts per unit flux per wavelength interval defined by the slit width of the instrument. The value of wavelength interval is given by

$$\Delta\lambda = \text{Resolution } (\text{Å/micron}) \times \text{Slit width (microns)}$$

4.7 Numerical values, HAD 305

The values of the relative spectral response of sodium salicylate were obtained by combining the results of Sampson (1964) and Kristianpoller and Knapp (1964) as no measurements were available that covered the range from

1216Å to 3000Å. Kristianpoller and Knapp find the response to be flat over the range 2100Å to 3000Å, and give a value for 1700Å. The range of Sampsons study includes 1216Å and 1600Å. The response was adjusted to the scale of Kristianpoller and Knapp by the relation:

$$SR_{1216} = SR_{1700} \frac{SR_{1216\ S}}{SR_{1600\ S}}$$

as the curve of response appears flat between 1600Å and 1700Å. The numerical values used in the calibration were:

Item	Symbol	Value
Spectral response at 1216Å	SR_{1216}	6.1
Spectral response 2000Å to 3000Å	SR_{λ}	8.0
Ion Chamber current at 1216Å	I_c	3.0×10^{-11} amp
Photomultiplier current at 1216Å	I_{p1216}	3.6×10^{-7} amp
Quantum efficiency of chamber	q	0.19
Gas gain factor	G	48.5
Area of diaphram	A_d	0.71 cm^2
Distance of diaphram from slit	D_d	4.7 cm
Distance of sensor from slit	D_s	26.2 cm
Resolution at slit of the monochromator		0.03Å/micron

The physical constants have the values

Plancks constant	$h = 6.625 \times 10^{-34}$ Joule sec
Speed of light	$c = 2.997 \times 10^{8}$ metres sec^{-1}
Electronic charge	$e = 1.602 \times 10^{-19}$ Coulomb

Taking the unit of $I_{p\lambda}$ as micro amps and the unit of wavelength as 10^3 Angstroms and noting that SR_λ is constant over the range covered by the sensors at a value of 8, equation (9) reduces to

$$S(\lambda) = \frac{R(\lambda).\lambda}{3.78 \times 10^{-12}} \quad \text{Volts per watt per cm}^2 \text{ per (0.03xSlit width)Å.} \quad (10)$$

The value of $S(\lambda)$ for the sensor centred at 2400Å is shown in Figure 4.2. As an example, the integral of $S(\lambda)$, recorded on the second stage of amplification, when operating at a slit width of 500 microns, of the sensor centred on 2400Å was

294 Volts per 10^{-12} watts per cm^2 per (0.03xslit width) Å

which reduces to

$$S_{2400} = 19.6 \text{ Volts per } 10^{-12} \text{ watts } cm^{-2} Å^{-1}$$
$$= 19.6 \text{ Volts per } 10^{-5} \text{ ergs } sec^{-1} cm^{-2} Å^{-1}$$

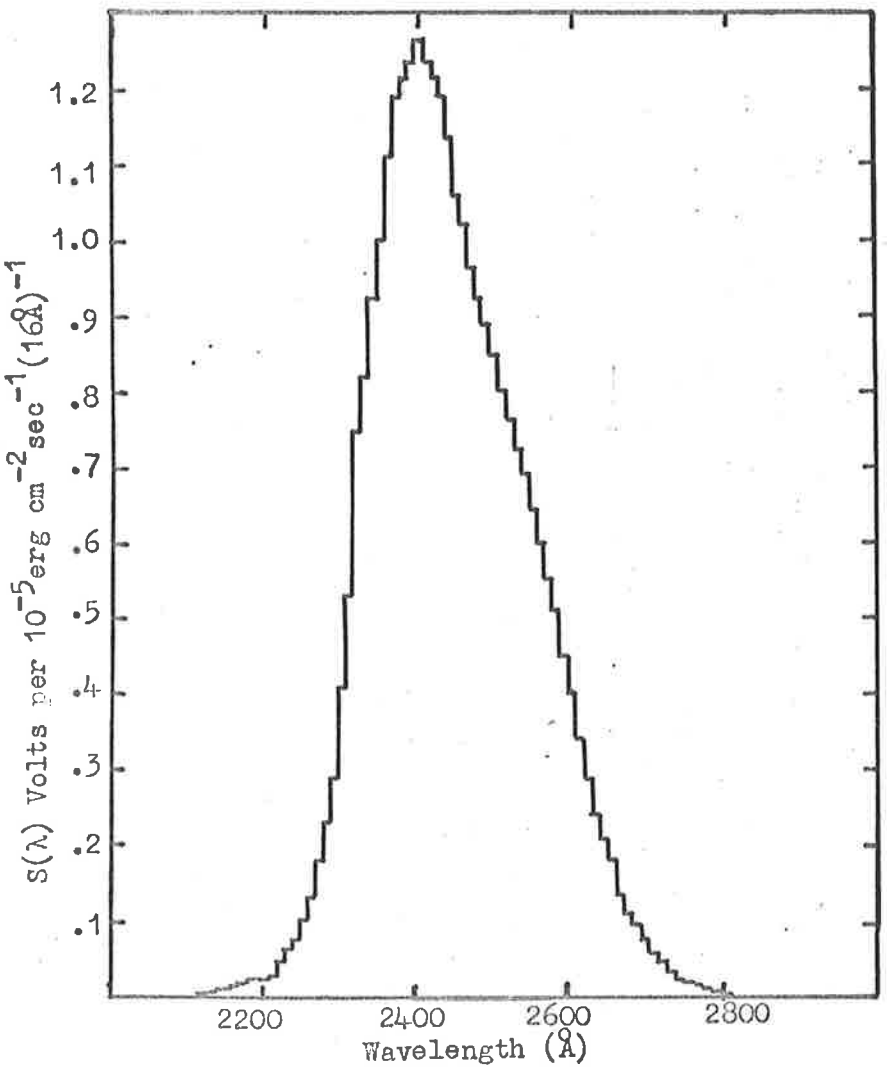

Figure 4.2 Measured response of second stage of the 2400Å sensor of HAD 305.

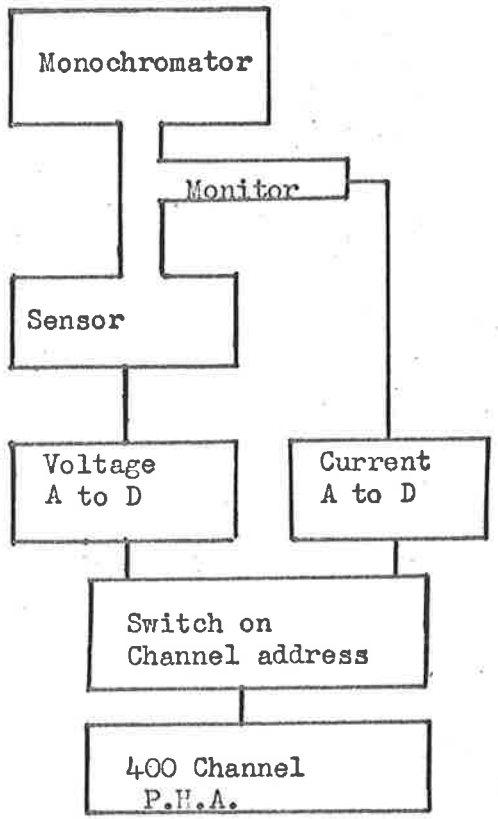

Figure 4.3 Layout of digital response measurement system.

where S_{2400} is the sensitivity of the sensor centred on 2400Å operated on amplifier stage 2. As stage 1 gain is less by a factor of 10 this sensitivity will be reduced by this factor on stage 1.

The sensitivity of the detectors flown in HAD 305, calibrated in this method, was

Wavelength of Centre	Sensitivity of First Stage
2400Å	1.96 Volts $(10^{-5}$ erg $sec^{-1} cm^{-2} Å^{-1})^{-1}$
2740Å	0.32 " " " " " " "
2910Å	0.49 " " " " " " "

where the wavelengths quoted are the measured peaks rather than the nominal values.

Measurements of the uniformity of the beam at 80 cm from the exit slit of the monochromator, made on this instrument, show that at the wavelength of Lyman α, there is a variation of intensity across the beam of up to 30% within the area used in this calibration. Measurements have not been made at wavelengths longer than Lyman α, but at 900Å and 584Å. By comparison of the beam patterns as a function of wavelength, it appears that there is an

increase of uniformity of the beam with increasing wavelength. As the photo cathode of the 1P28 photo-multiplier is rectangular in shape, it would not be sampling the whole of the area monitored by the beam splitter but a strip which would contain the central region of the beam. If the beam section viewed by the sensor is more intense than that seen by the monitor, the measured sensitivity of the sensor will be higher than its actual value. The structure of the beam cross section was, however, measured with line radiation. As the radiation in the 2000Å to 3000Å region was continuous, and the sensitivity of the sensor was not sharply varying with wavelength, the intensity across the beam should have been smoothed by the contribution of wavelengths adjacent to the central wavelength passed.

The conclusions reached from these considerations is that the sensitivity of the sensor could contain a possible error of order 20% introduced by the assumption of uniform illumination of the aperture. A further error may be introduced by the use of the relative response values of the sodium salicylate as variations of order 10% can occur, dependent upon the age and thickness of the layer used, the actual values employed being undetermined. The total error to be expected in the

calibration was of the order of 25%.

4.8 Calibration of HAD 312

The method of calibration used for three of the sensors flown in the second round fired was basically the same as that used in the previous round, the difference being that a 1 metre McPherson monochromator was employed. The wavelengths covered were scanned at a constant rate and the current and voltage measurements were made with an analog to digital integrating system, The integration period was coupled to the wavelength drive of the monochromator, and the sensor output and monitor current were recorded alternately and stored in a pulse height analyser operated in sequential address mode. A diagramatic layout of the recording system is shown in Figure 4.3.

Prior to the measurement of the current and voltages required for the calibration, the number of counts recorded for each system for known current and voltage inputs was measured over a period equal to that used during the wavelength scan. The values of the recorded

counts for sensor and spectrum for the sensor centred on 2500Å are shown in Figure 4.4. The number of counts recorded was then used, in each case, to determine the monitor current and the output voltage. In practice the mean value of the number of counts recorded in the channels adjacent to the voltage channel was used to determine the value of the monitor current. The value of the term $R(\lambda)$ of equation (9) was then determined by taking the ratio of the current and voltage so measured. The remainder of the procedure employed in the calibration of HAD 305 was applied as before. Numerical values of terms which were different from the previous measurement are given below.

Item	Symbol	Value
Ion chamber current at 1216Å	I_c	4.4×10^{-12} amps
Photomulitplier current at 1216Å	I_{p1216}	1.25×10^{-6} amps
Quantum efficiency of chamber	q	0.13
Gas gain factor	G	1.0
Resolution at slit of the monochromator		0.0038Å per micron

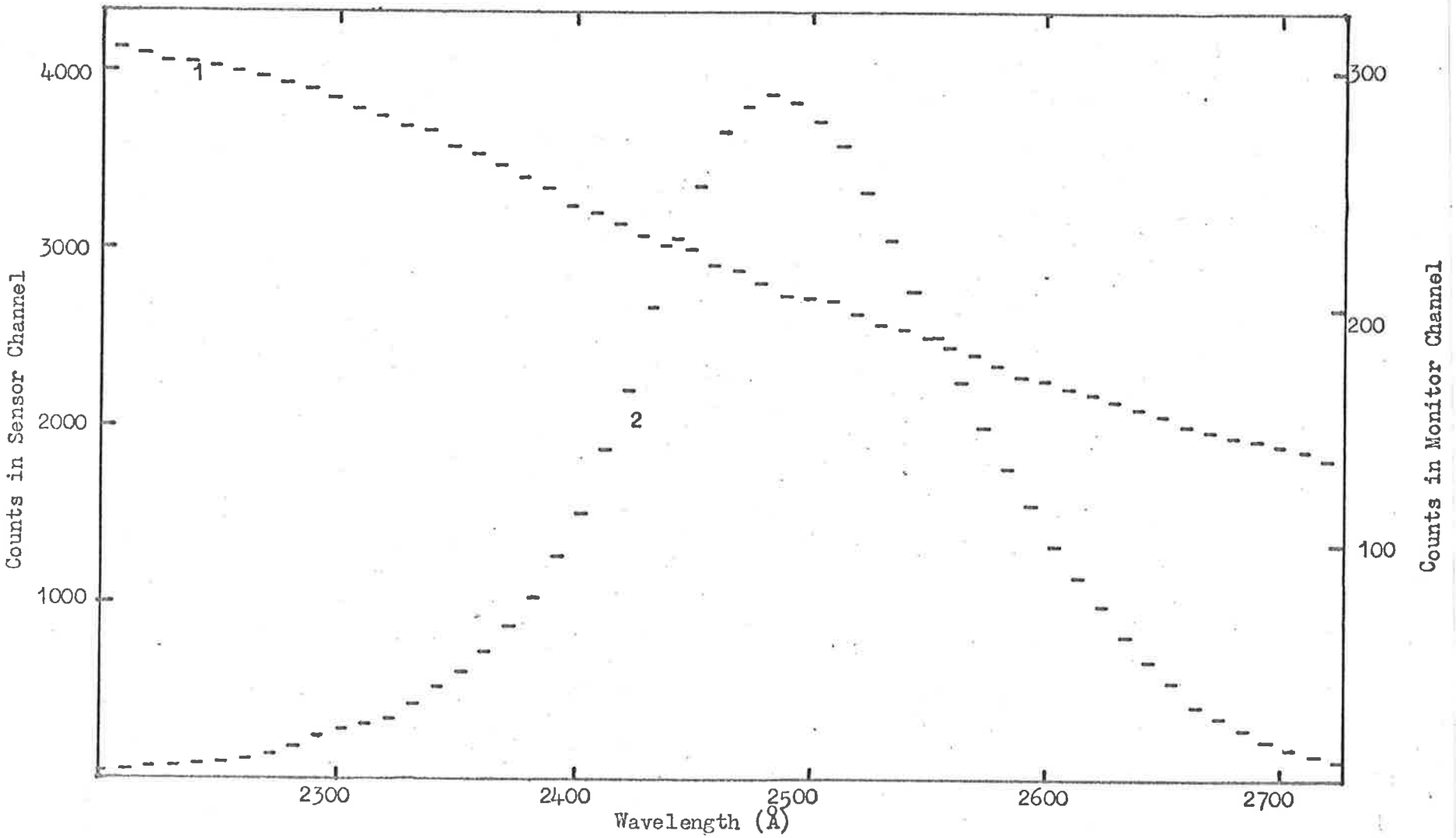

Figure 4.4 Results of digital recording for the sensor centred on 2500Å in HAD 312. (1 Monitor, 2 Sensor). Alternate channels scan for 5Å at fixed scan rate.

As the limit of the monochromator used for the calibration of HAD 312 was 3000Å, the sensor centred at a wavelength of 2900Å required a separate method of measurement of sensitivity. The light source used was a Bauch and Lomb high intensity monochromator illuminated by a high pressure mercury discharge lamp. The beam was passed through a second monochromator to reduce scattered light and the exit slit of this instrument taken as the source. The slit widths of the primary source were set to a pass band of 120Å and the emergent wavelength set at 2900Å. The resolution of the second instrument was such that the pass band would be still effectively 120Å. Two thermopiles were placed in the beam, an Eppley open window thermopile of sensitivity 0.069 microvolts per microwatt per cm^2, and an uncalibrated Reeder quartz window thermopile.

The outputs of the two thermopiles placed successively in the same position in the beam were:

Eppley - 9.4 microvolts Reeder - 68.0 microvolts

giving a calibration of the Reeder thermopile at 2900Å of 0.5 microvolts per microwatt per cm^2.

The sensor to be calibrated was mounted at a distance of 345 cms from the source and the Reeder thermopile at a distance of 23 cms from the source in such a way

that sufficient of the beam passed the thermopile to fully illuminate the sensor. Prior to measurement of the sensor output, the thermopile was placed in that part of the beam that would by pass it to the sensor during calibration in order to test for uniformity across the beam. No sensible difference was observed between the two positions although, due to the open mounting necessary, air currents and other sources produced a noise level of about 10% of output read. Because of the intensity of the beam at the sensor, a 5% transmission Perkin Elmer attenuator was placed 10 cms from the sensor, the distance being such that the diffraction pattern of the attenuator was smoothed to give even illumination. The reduction factor between the energy as measured by the thermopile and that at the sensor was then:

$$\left(\frac{23}{345}\right)^2 .0.05 = 2.1 \times 10^{-4}$$

The results of the measurement were:

Measured Thermopile output	Flux at sensor	Sensor output
2.0 microvolts	8.4 microwatts cm^{-2}	0.5 volts

With the above resolution, these values reduced to a sensitivity of

0.07 volts per 10^{-5} ergs $sec^{-1} cm^{-2} Å^{-1}$

As the signal obtained for this sensor in HAD 305 was of the order of 2×10^{-5} erg $sec^{-1} cm^{-2} Å^{-1}$, this sensitivity was too low and was increased by increasing the input impedance of the first stage of the amplifier, thus increasing the sensitivity by a factor of four. The sensitivities of all sensors flown in HAD 312, calibrated as stated above were as listed below.

Wavelength at centre	Sensitivity of First Stage
2400Å	2.13 volts/10^{-5} erg $sec^{-1} cm^{-2} Å^{-1}$
2490Å	2.2 volts/10^{-5} erg $sec^{-1} cm^{-2} Å^{-1}$
2740Å	0.51 volts/10^{-5} erg $sec^{-1} cm^{-2} Å^{-1}$
2910Å	0.28 volts/10^{-5} erg $sec^{-1} cm^{-2} Å^{-1}$

A similar error of 30% was also applied to these calibrations.

4.9 Aspect Correction

As the angle between the normal to the sensor and the sensor source line was expected to vary during flight, the angular response of each sensor was determined. For both HAD 305 and HAD 312 this was done by mounting

the instrumentation section with the axis horizontal on a table, free to rotate in the horizontal plane. (See Figure 4.5). The sensors were illuminated by a Bauch and Lomb monochromator and the zero position was determined by observation from behind the source, of the reflected light from the surface of the interference filter. The output of each sensor was then recorded as a function of angle as the table was rotated in the horizontal plane. The responses of the various sensors are shown in Figure 4.6 (.1, .2, .3, .4, .5, .6, .7). The assymetric nature of the response results from the structure and orientation of the photocathode of the 1P28 photomultiplier.

4.10 Design and Calibration of Aspect Sensors

The variation of sensor response with aspect angle required that this angle be measured in flight. The aspect sensor was similar in both sets of instrumentation and is shown in Figure 4.7. As assumption made in the measurement of angle with this system was that the roll rate of the vehicle is only slowly varying and is much greater than the precession rate of the longitudinal axis of the vehicle. As the vehicle rolled, the source would

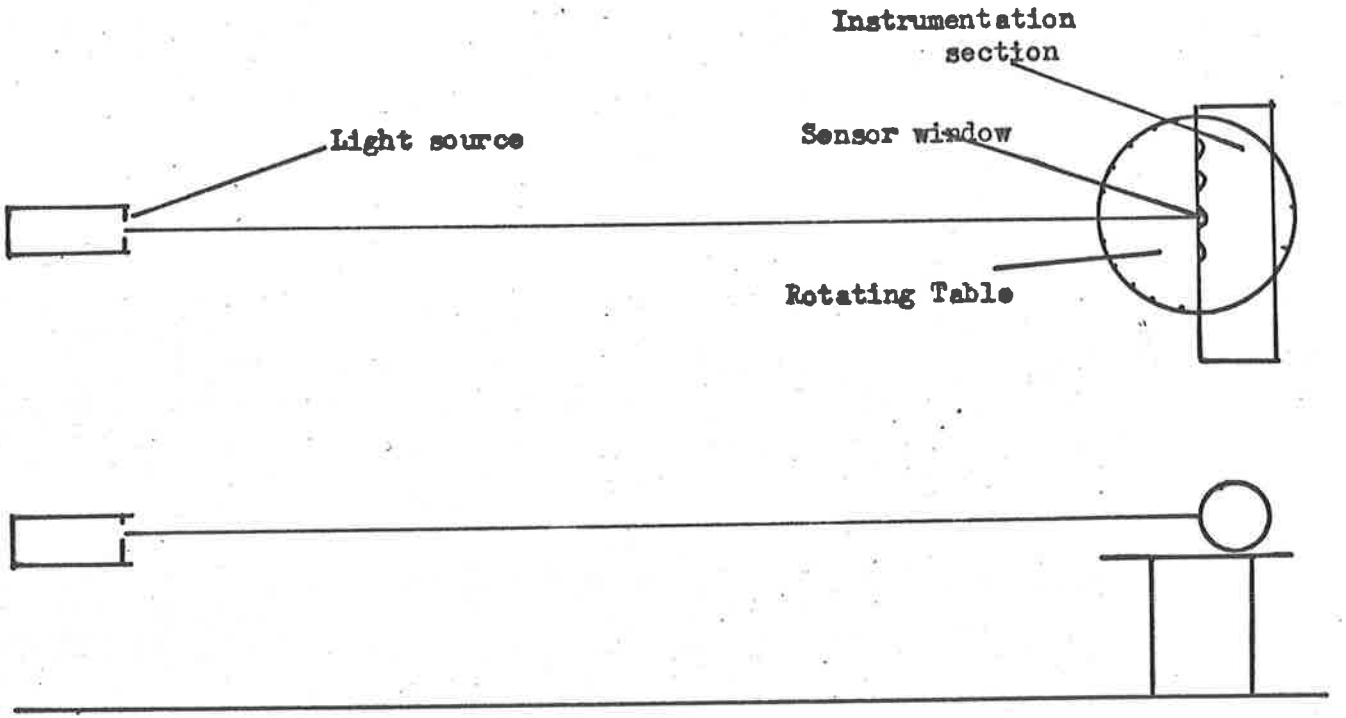

Figure 4.5 Diagram of method of measurement of angular response of detectors.

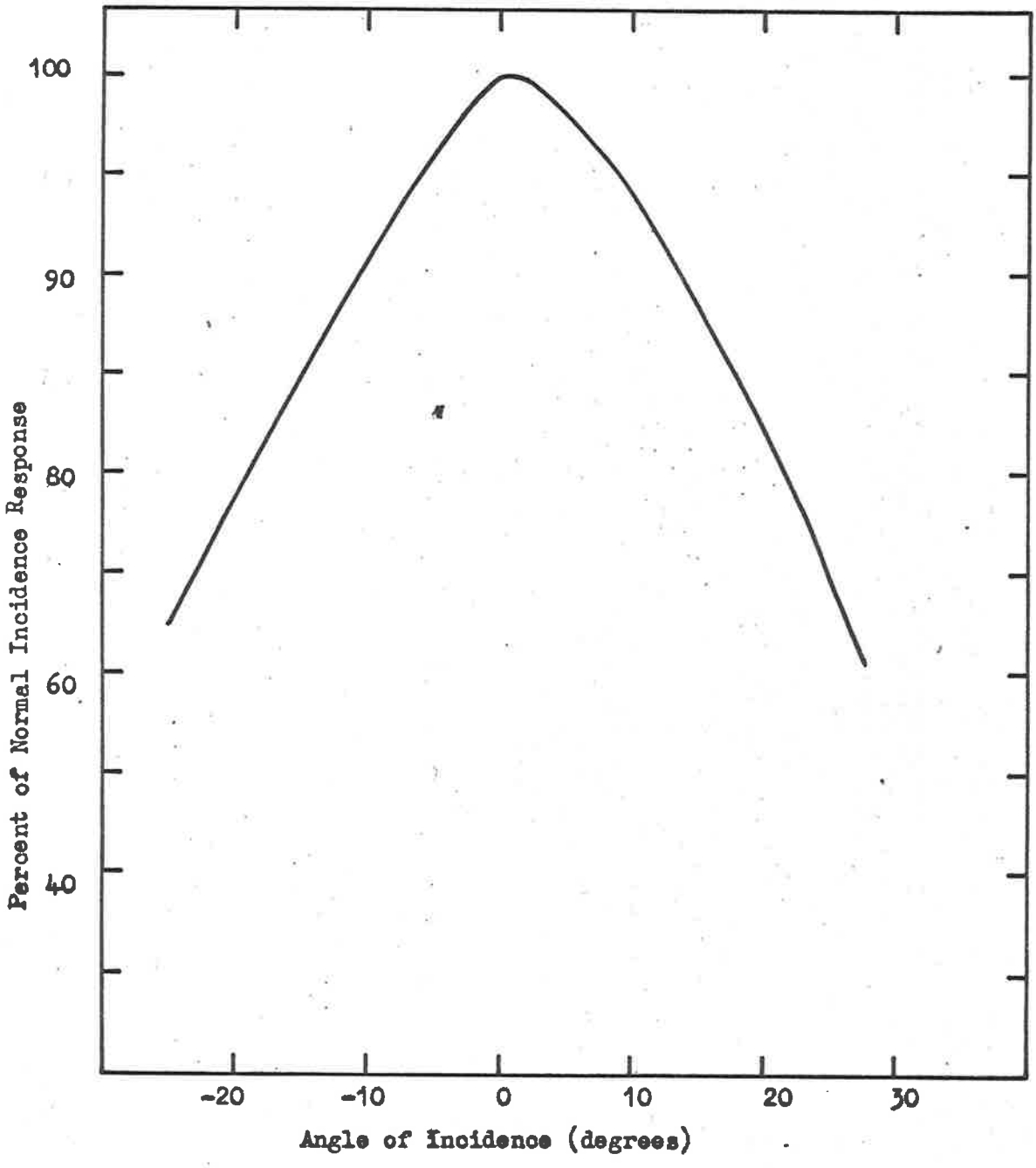

Figure 4.6.1 Angular response of 2400Å sensor in HAD 305.

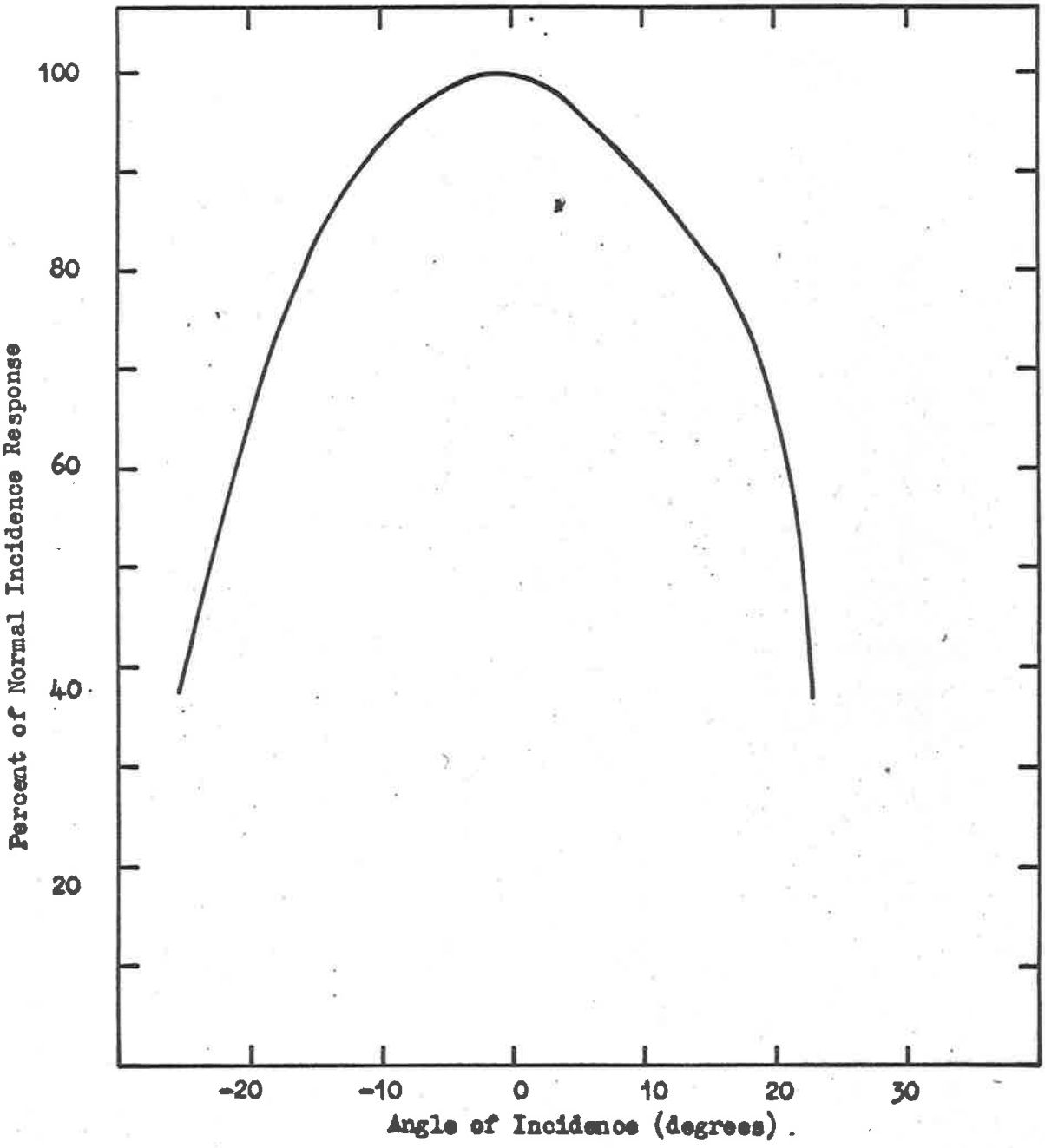

Figure 4.6.2 Angular response of 2700Å sensor in HAD 306.

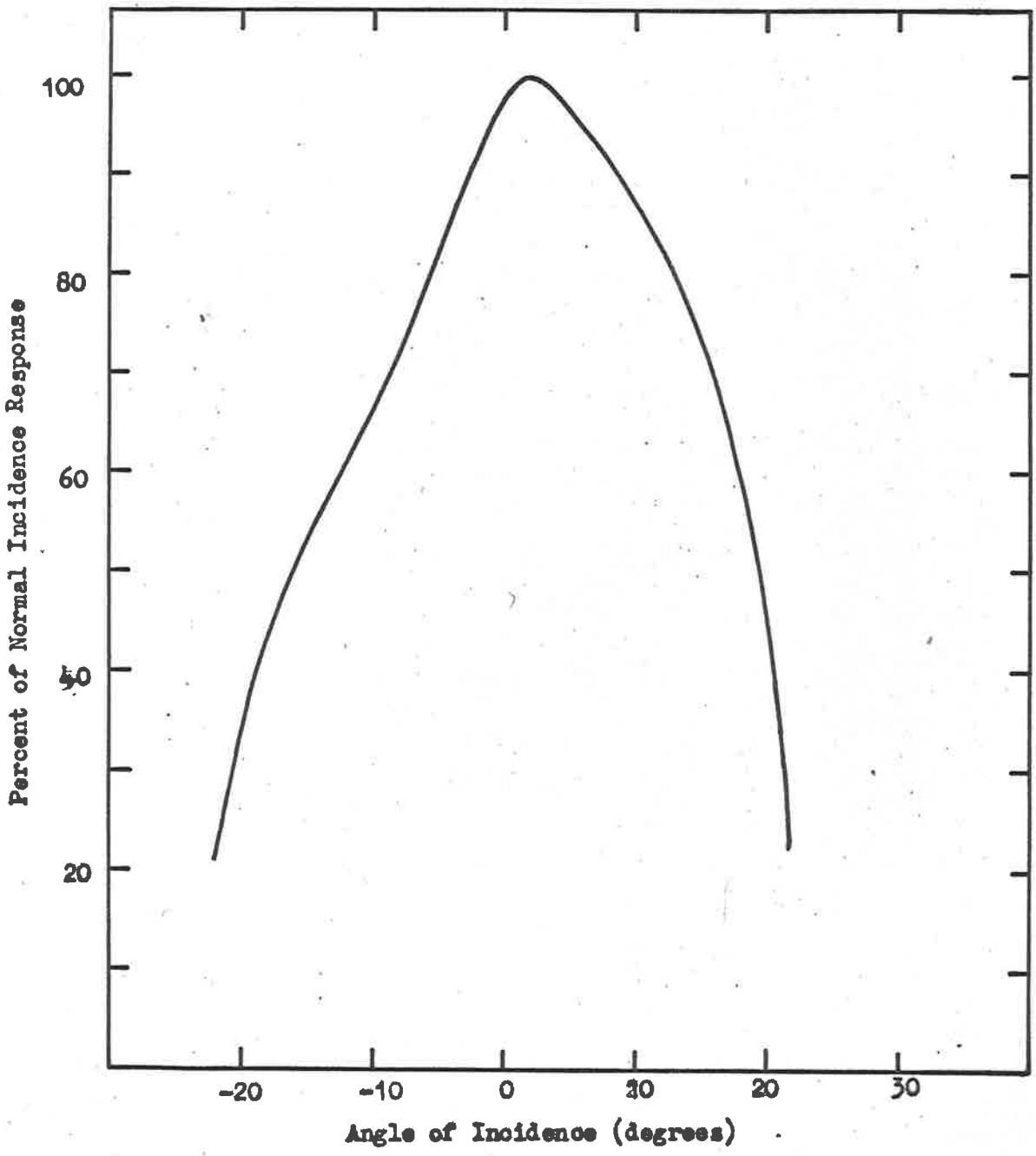

Figure 4.6.3 Angular response of 2900Å sensor in HAD 305

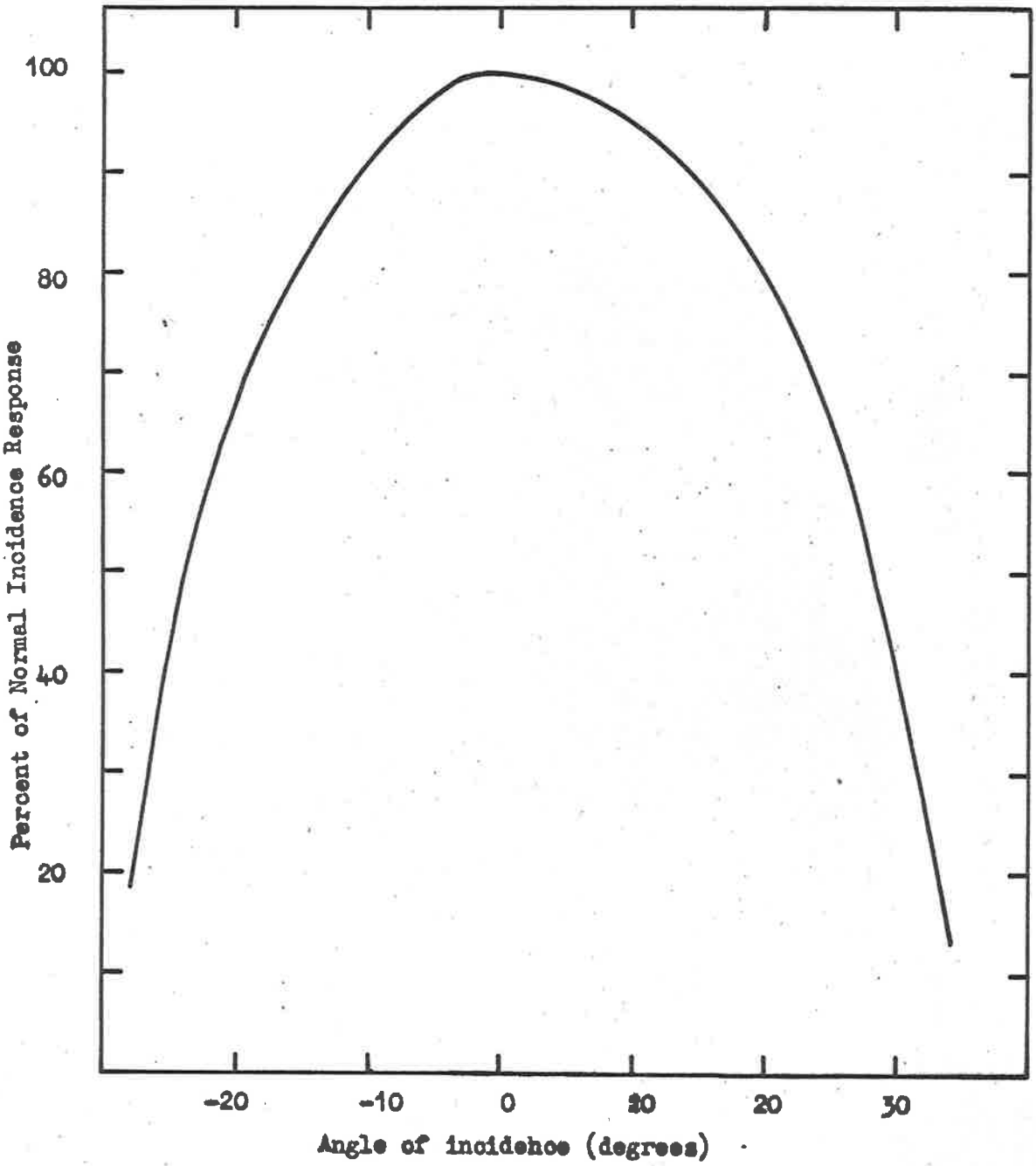

Figure 4.6.4 Angular response of 2400Å sensor in HAD 312.

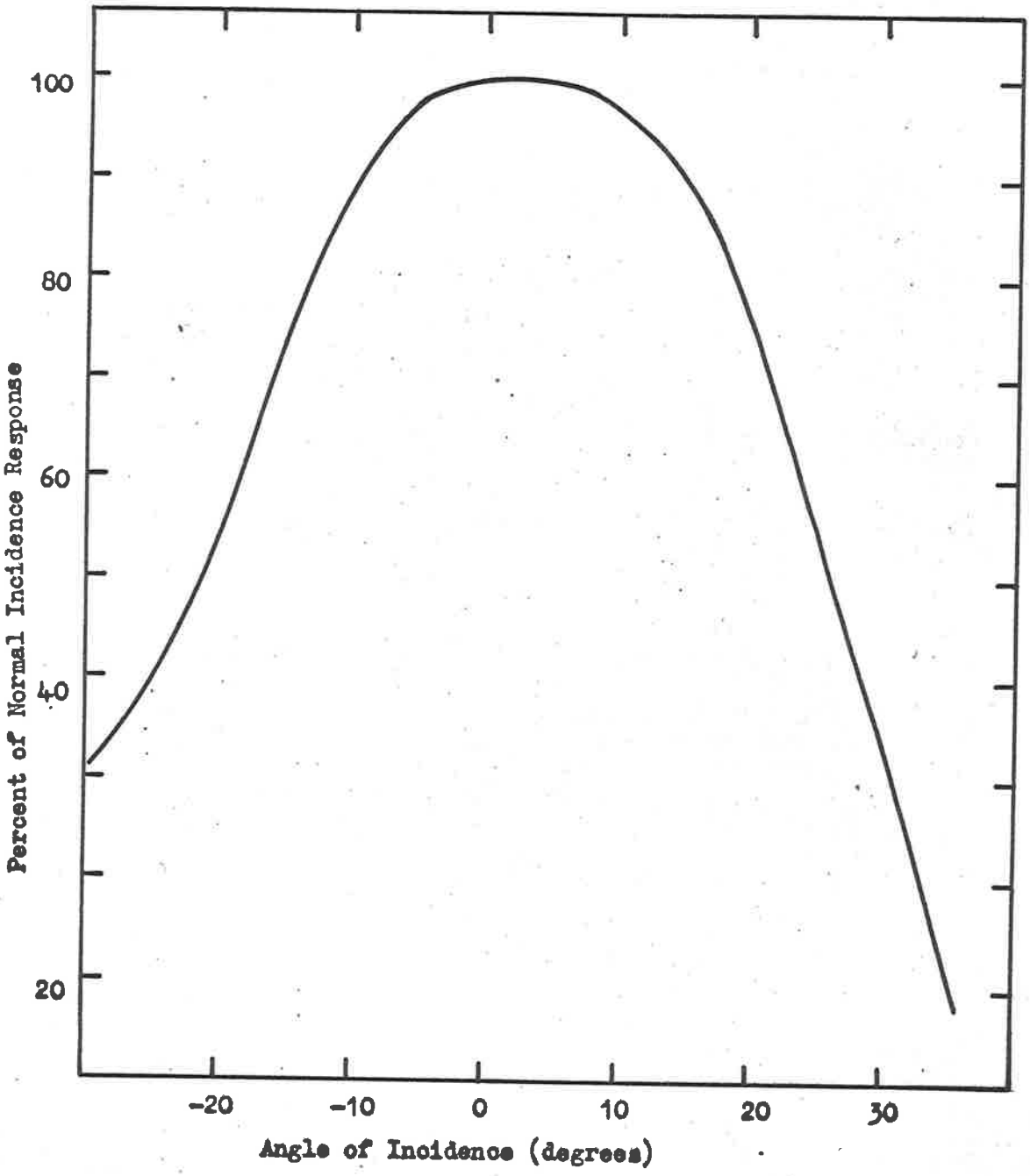

Figure 4.6.5 Angular response of 2500Å sensor in HAD 312.

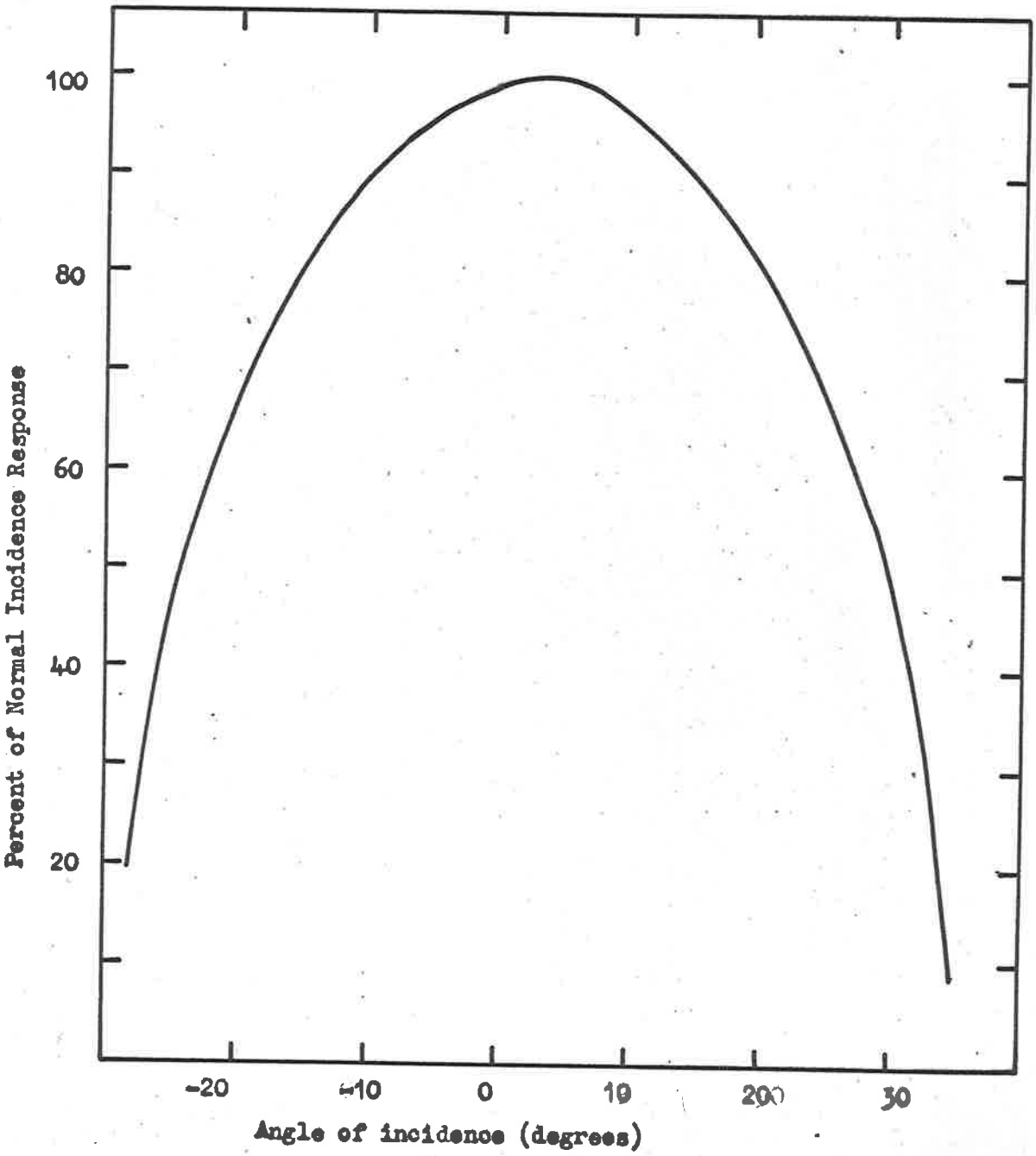

Figure 4.6.6 Angular response of 2700Å sensor in HAD 312.

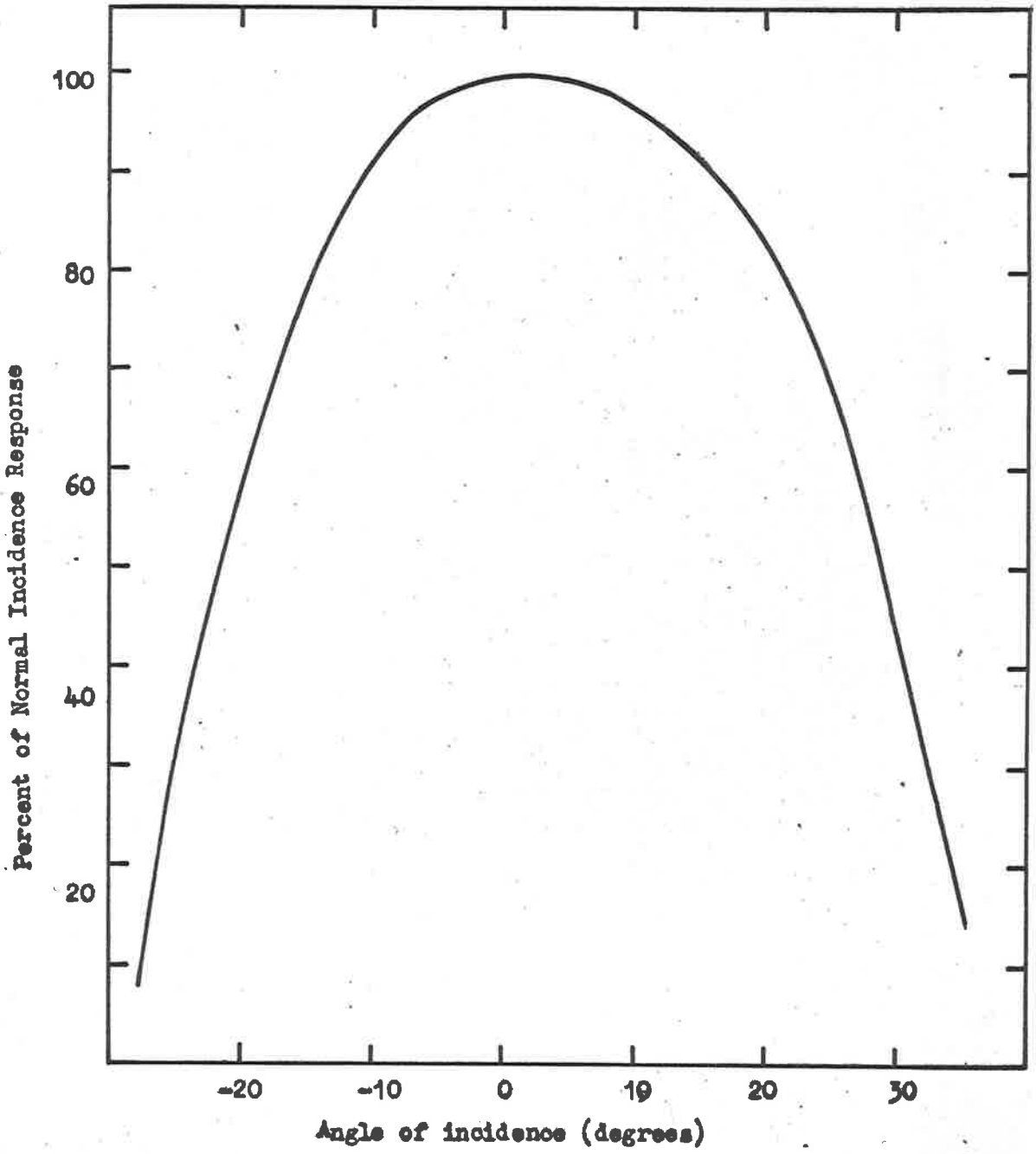

Figure 4.6.7 Angular response of 2900Å sensor in HAD 312.

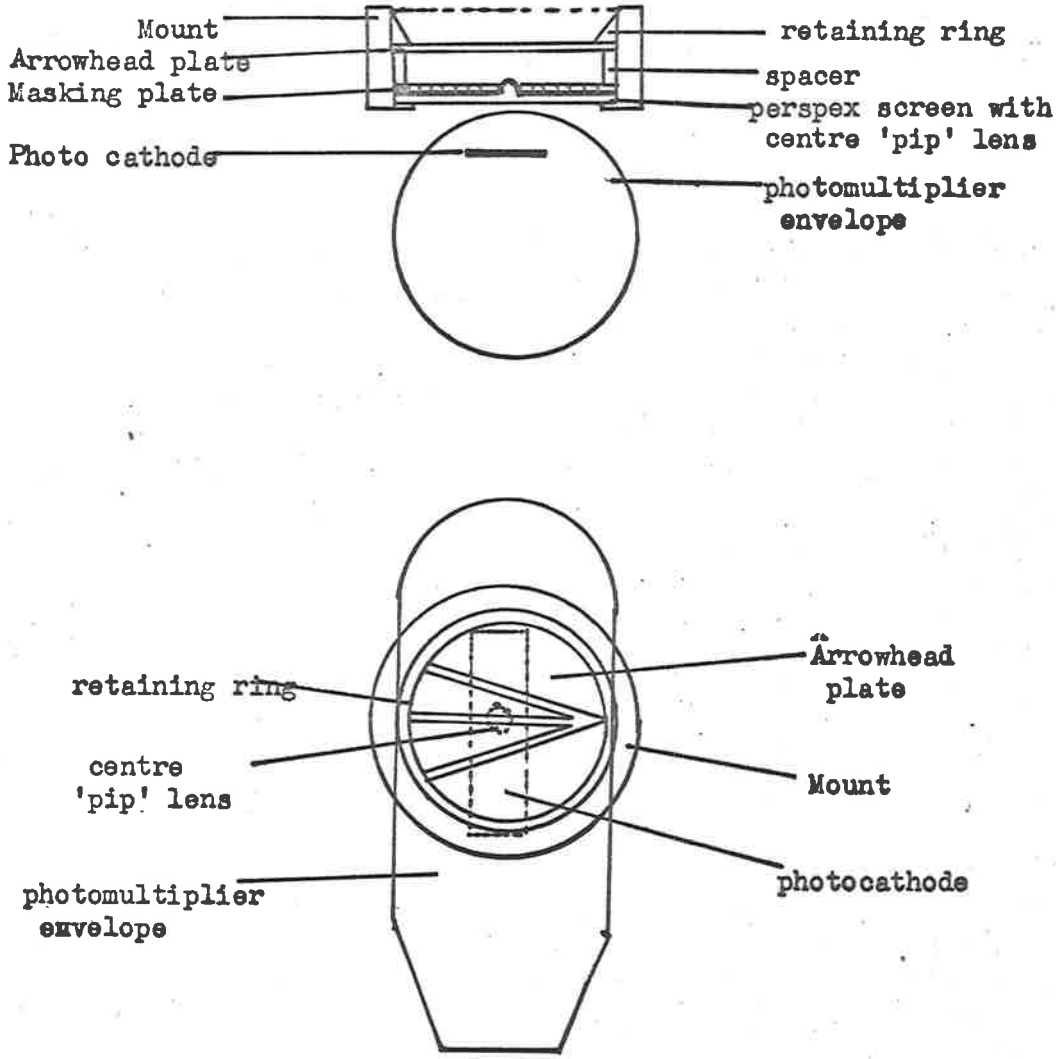

Figure 4.7 Design of the aspect sensors flown in HAD 305 and 312.

illuminate the centre lens through each of the slits of the arrowhead array. The output of the sensor is recorded as a function of time by the telemetry, a sample of record being shown in Figure 5.1. If the period between the extreme pulses of the three be t_o, the period between the centre pulse of the previous group and the centre pulse of the following group be t_1, then the angle through which the vehicle has rotated in order that the source illuminate the centre lens through the outer slits may be determined by the relation:

$$2\phi = 360 \times \frac{2t_o}{t_1} \text{ degrees}$$

Referring to Figure 4.8,

$$\phi = \tan^{-1} \frac{(a - d \tan\theta) \tan\alpha}{d \sec\theta}$$

i.e. $$\frac{d}{\tan\alpha} \tan\phi = a\cos\theta - d\sin\theta$$

$$= c \sin(\beta - \theta)$$

i.e. $$\theta = \beta - \sin^{-1}\left(\frac{d}{c \tan\alpha} \tan\phi\right)$$

Thus the aspect angle θ appears as a function of the observable angle ϕ. Measurement of the angle ϕ at normal incidence allows the evaluation of the constant c so that a theoretical curve of the response may be

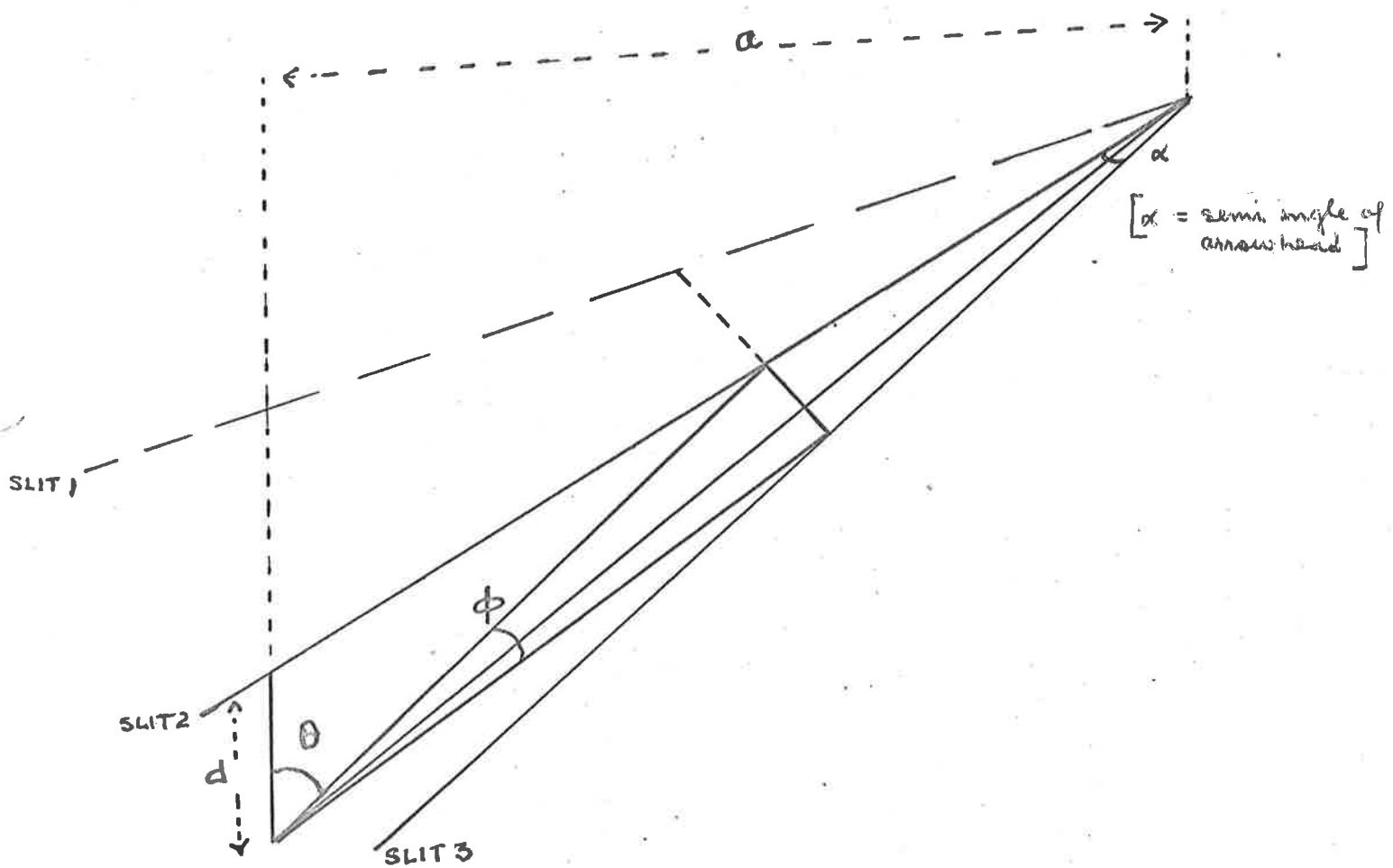

Figure 4.8 Schematic representation of the arrowhead aspect sensor.

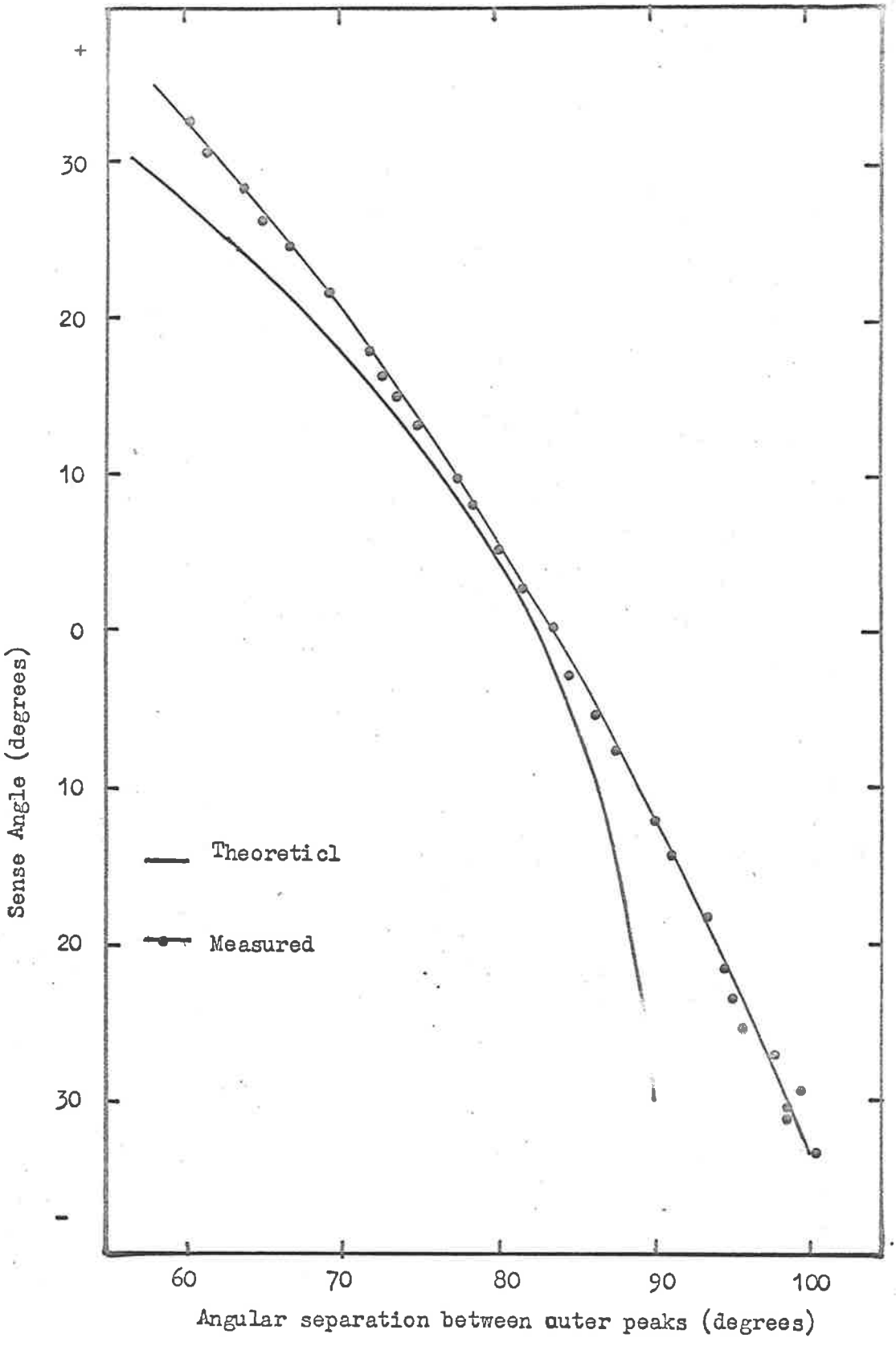

Figure 4.9 Measured and theoretical curves of aspect sensor for HAD 305. Sense angle is angle between source and line of sight of sensor. Positive is towards forward direction.

drawn. Due to the finite size of the central lens and the width of the slits, some variation occurs between the theoretical curve and the measured response obtained by rotation of the instrumentation section about its longitudinal axis while the angle between this axis and the direction of the light source was fixed by the position of the rotating table carrying the instrumentation. The measured curve and the theoretical curve for the aspect sensor in HAD 305 is shown in Figure 4.9.

CHAPTER 5

REDUCTION OF EXPERIMENTAL DATA

5.1 Details of Location and Times of Rocket Flights

In the course of the experiments performed, two rockets were successfully launched, both from the Woomera Rocket Range of the Weapons Research Establishment of the Australian Department of Supply. The range head is situated at 30° 35' South latitude and 136° 31' East longitude.

The first vehicle, designated HAD 305, was fired at 22 35 hours Australian Central Time on the 9th December, 1965 at which time the moon was at a zenith angle 67° and at a phase angle from full moon of 10°.

The second vehicle, designated HAD 312, was fired at 19 35 hours on 30th August, 1966, at which time the moon was at a zenith angle of 62° 30' and at a phase angle from full moon of 2° 30'.

The high zenith angle, on the limit of the acceptance of the Sec θ approximation, as shown in Section

2.8, was chosen such that, had the vehicle maintained the direction of its axis along the line of firing and spun about this axis, the radiation would have been incident almost normally on the windows of the sensors.

5.2 Tracking Records Available

The range centre line extends to the Northwest of the launch site, so that the flight path of the rockets was in this direction. Both vehicles were skin tracked by FPS16 radar from a site to the Southeast of the launch site. Magnetic tape records of the radar tracking data were processed by the Weapons Research Establishment and the resulting output presented in the form of X, Y, Z, $\dot{X}$, $\dot{Y}$, $\dot{Z}$ and Height as a function of time from launch, where X measures horizontal distance along range centre, Y horizontal distance normal to X and Z perpendicular distance above the launch site. Height is the Z coordinate corrected for height above sea level and curvature of the earth. The time interval between listings is 0.5 seconds.

5.3 Form of the Telemetered Data Received

Telemetered values of the voltages appearing at the outputs of the amplifiers are recorded on magnetic tape and processed by the Weapons Research Establishment and are presented in the form of film records as a plot of sensor voltage against time for the duration of the flight. Figure 5.1 is an example of the records from one of the ultraviolet photometers and the aspect sensor flown. The continuous horizontal lines appearing on the record are the 0.0, 0.75 and 1.5 volt calibration levels. The two traces shown in part b are those of two stages of the amplifier associated with the sensor.

5.4 Determination of the Height vs Time Relation

The direction of flight of the HAD rocket is set, initially, by the attitude at launch, while the velocity attained is determined by the magnitude of the two 3 second impulses imparted to it by the burning of the first and second stage motors. After burnout of the second stage motor, the trajectory, to a first approximation,

Figure 5.1 Example of the final form of the telemetry records.

(a) Aspect sensor

(b) Two stages of a photometer amplifier.

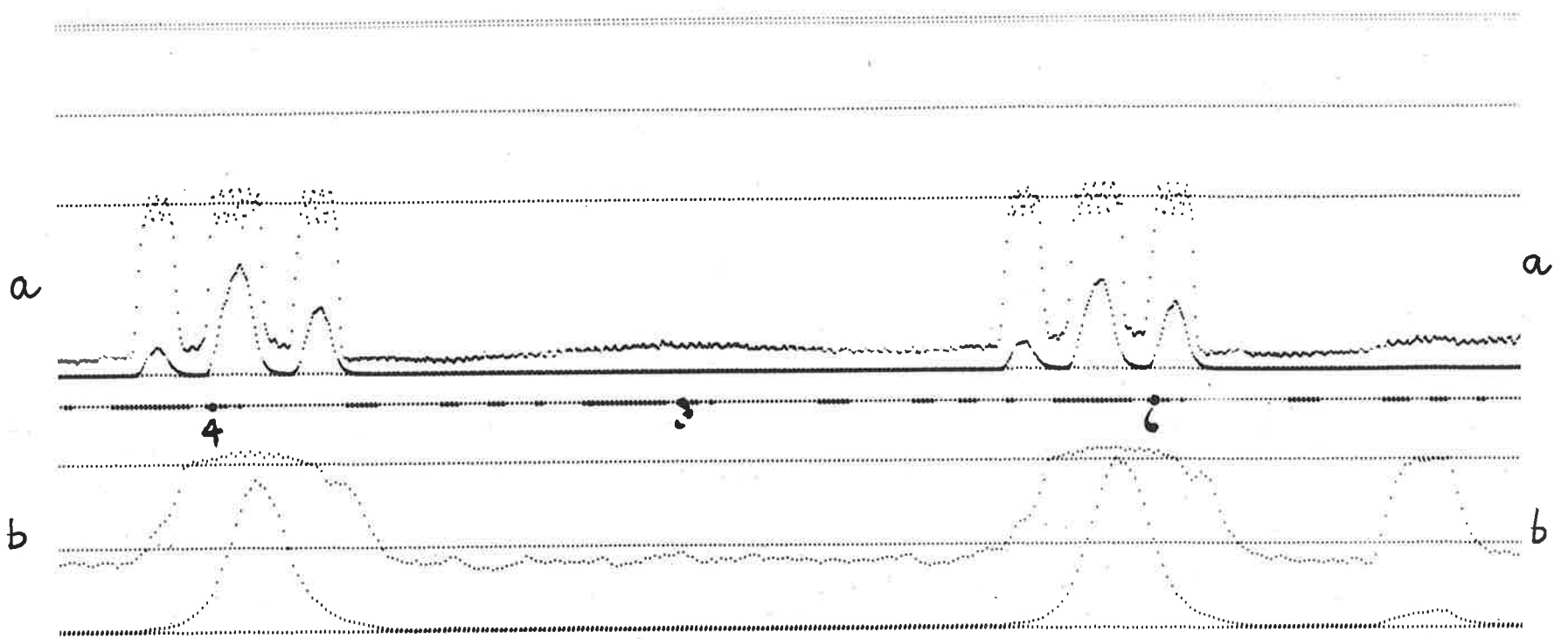
a
a
4
3
6
b
b

will be ballistic. However, as this event occurs at heights about 70 kilofeet, and the speed has a maximum value here, the effect of the viscosity of the air is sufficient to modify the ballistic character of the lower portion of the trajectory. For this reason the determination of the path of the vehicle should be calculated from measured values obtained near the position of maximum altitude where more truely ballistic conditions may be assumed. By relating the path so calculated to the measured values obtained at lower portions of the path, the effects of the air drag may be illustrated.

Because of the lack of knowledge of the attitude of the vehicle, and hence, the drag coefficient of the surface, no quantitative measures of air density may be obtained from these measurements.

The height vs time relation for each vehicle was determined in the following manner. From the radar information, a plot was made of $\dot{Z}$ vs time from launch. From this plot it was possible to estimate a time of apogee, this being when $\dot{Z}$ was equal to zero. Let the true time of apogee be T and the approximate time of apogee estimated as above, be t_o, where

$$t_0 = T + c$$

where c is a small time interval.

Let

$$\tau = |t_0 - t|$$

where t is the elapsed time since launch, in unit intervals, listed as described in section 5.2, and h(t) is the computed height as a function of time from radar results.

The estimated height of apogee was then calculated for each value of h(t) from the relation

$$h_0 = h(t) + \tfrac{1}{2} \bar{g} \tau^2$$

where h_0 is the estimated height of apogee and $\bar{g}$ is the effective value for the acceleration due to gravity experienced by the vehicle for the period τ.

The value of $\bar{g}$ was estimated by the following method. Taking a linear approximation for the value of g as a function of height in the following form

$$g = g_s - ah$$

where g_s, the value of g at the earths surface is in feet

sec^{-2}, and has the value 32.13 feet sec^{-2} and a has the value 3.0866×10^{-6} if the height h is in feet.

This is the linear approximation of the expression

$$g = 979.3244 - 3.0866 \times 10^{-4} z + 7.259 \times 10^{-11} z^2 \text{ cm sec}^{-2}$$

where z is the height in metres. (C.I.R.A. 1965)

The expression for g may be rewritten in the form

$$g = g_s - ah_o + a(h_o - h(t))$$

$$= g_{apogee} + a(h_o - h(t))$$

$$= g_{apogee} + \tfrac{1}{2} a \bar{g} \tau^2$$

As the value of acceleration due to gravity can only vary by 3% over the height range covered by the vehicle and the value of τ^2 will be of the order of 10^4, i.e. a τ^2 is of order 10^{-2}, the value of $\bar{g}$ in this expression is set at the value at apogee, and the approximation made that

$$g = \bar{g}_{apogee} (1 + \tfrac{1}{2} a \tau^2)$$

The effective value of g over the time interval

is then given by

$$\bar{g} = \frac{g_{apogee} \int_0^\tau t + \frac{1}{2} a t^3 \, dt}{\int_0^\tau t \, dt}$$

$$= g_{apogee} \left(1 + \frac{a}{4} \tau^2\right)$$

An estimate of the true height of apogee may be obtained from the relation

$$H_0 = h(t) + \frac{1}{2} \bar{g} (\tau - c)^2$$

$$= h(t) + \frac{1}{2} \bar{g} (\tau^2 - 2\tau + c^2)$$

where H_0 is the estimated true height of apogee.

As c is a small quantity the term in c^2 may be neglected;

i.e. $$H_0 = h(t) + \frac{1}{2} \bar{g} \tau^2 - \bar{g} \tau c$$

$$= h_0 - \bar{g} \tau c$$

i.e. $$h_0 = g_{apogee} \left(1 + \frac{a}{4} \tau^2\right) \tau c + H_0$$

As $\frac{a}{4}$ has the value of 7.716×10^{-7} and τ is of the order of 10^2, the above expression may be simplified

without sensible loss of accuracy to the form of

$$h_0 = g_{apogee}\, c\, \tau + H_0$$

and if a plot is made of the values of h_0, calculated from the expression

$$h_0 = h(t) + \tfrac{1}{2}\, g_{apogee}\, (1 + \tfrac{a}{4}\, \tau^2)\, \tau^2$$

vs τ, the slope of the curve gives the value of c within 1%.

From the expression above, on differentiation with respect to time interval τ, where c is equivalent to $\Delta\tau$,

$$h_0 - H_0 = \Delta h_0 = g_{apogee}\, (\tau + \tfrac{1}{2}\, a\, \tau^3)\, c$$

i.e. $$H_0 = h_0 - \Delta h_0$$

whereby a number of estimates of the value of apogee height may be calculated from the values of h_0 previously obtained. The mean value of these is taken as the best estimate of the height of apogee while, from the relation $t_0 - c = T$, the true time of apogee may be obtained. The height vs time relations for HAD 305 and HAD 312 are shown

in Figures 5.2 and 5.3.

If the calculated values of time and height of apogee are combined with the radar values of h(t) the value of $\bar{g}$ may be determined as a function of time from apogee by the relation

$$\bar{g} = \frac{2\,(h_0 - h(t))}{\tau^2}$$

A plot of the values of $\bar{g}$, so determined for HAD 305 is shown in Figure 5.4 and in this the effect of air drag on the vehicle may be clearly seen. As stated previously, lack of knowledge of the attitude of the vehicle and hence the drag coefficient at this altitude prevents the use of these values to determine air densities.

5.5 Variation of Aspect Angles During Flight

By use of the aspect sensors carried in each set of instrumentation, as described in Section 4.10, the angle between the normal to the sensor and the source position vector was determined at the instant of closest approach for each reducable scan. The angle at each scan

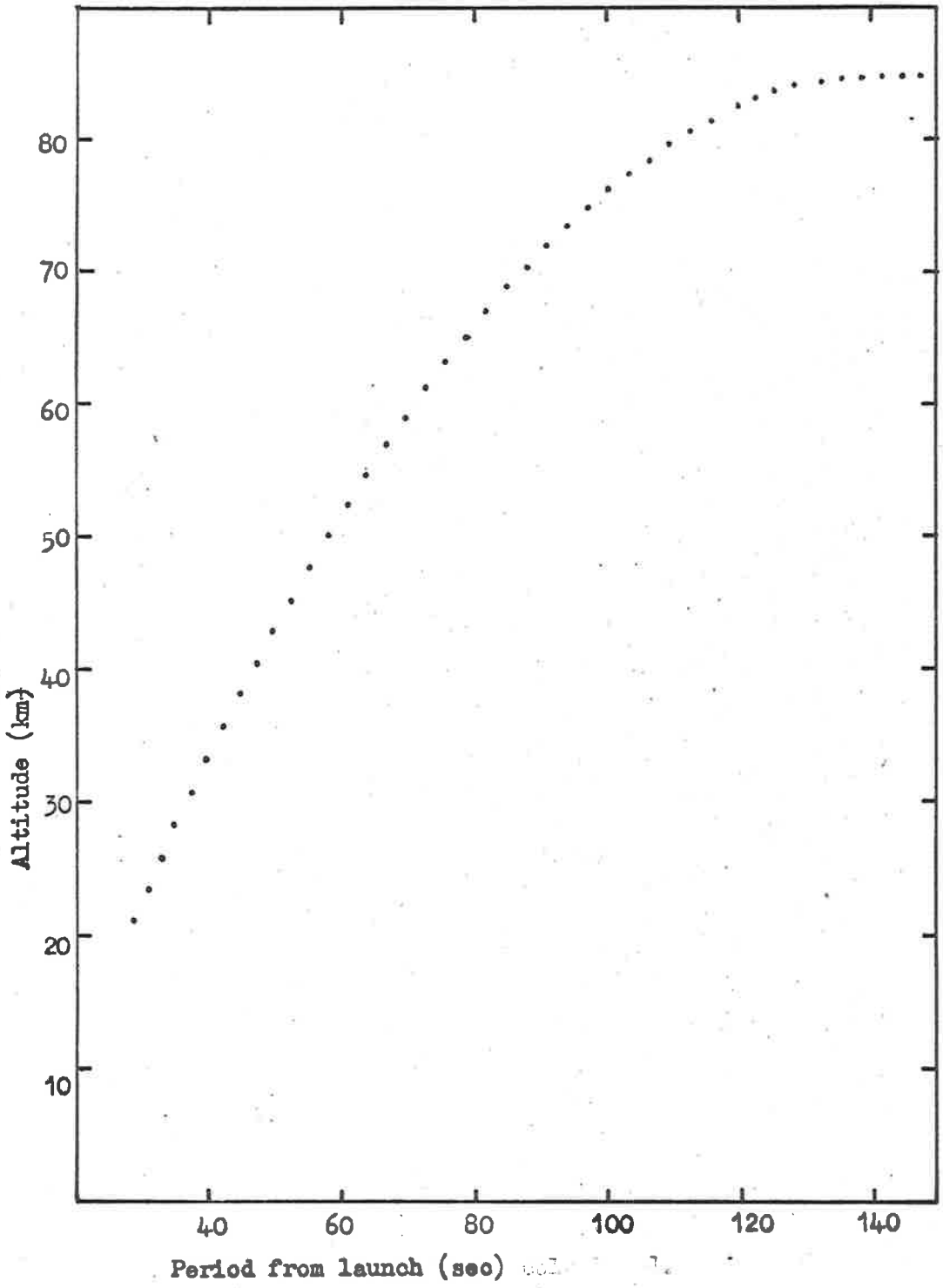

Figure 5.2 Calculated variation of Altitude with time from launch
HAD 305.

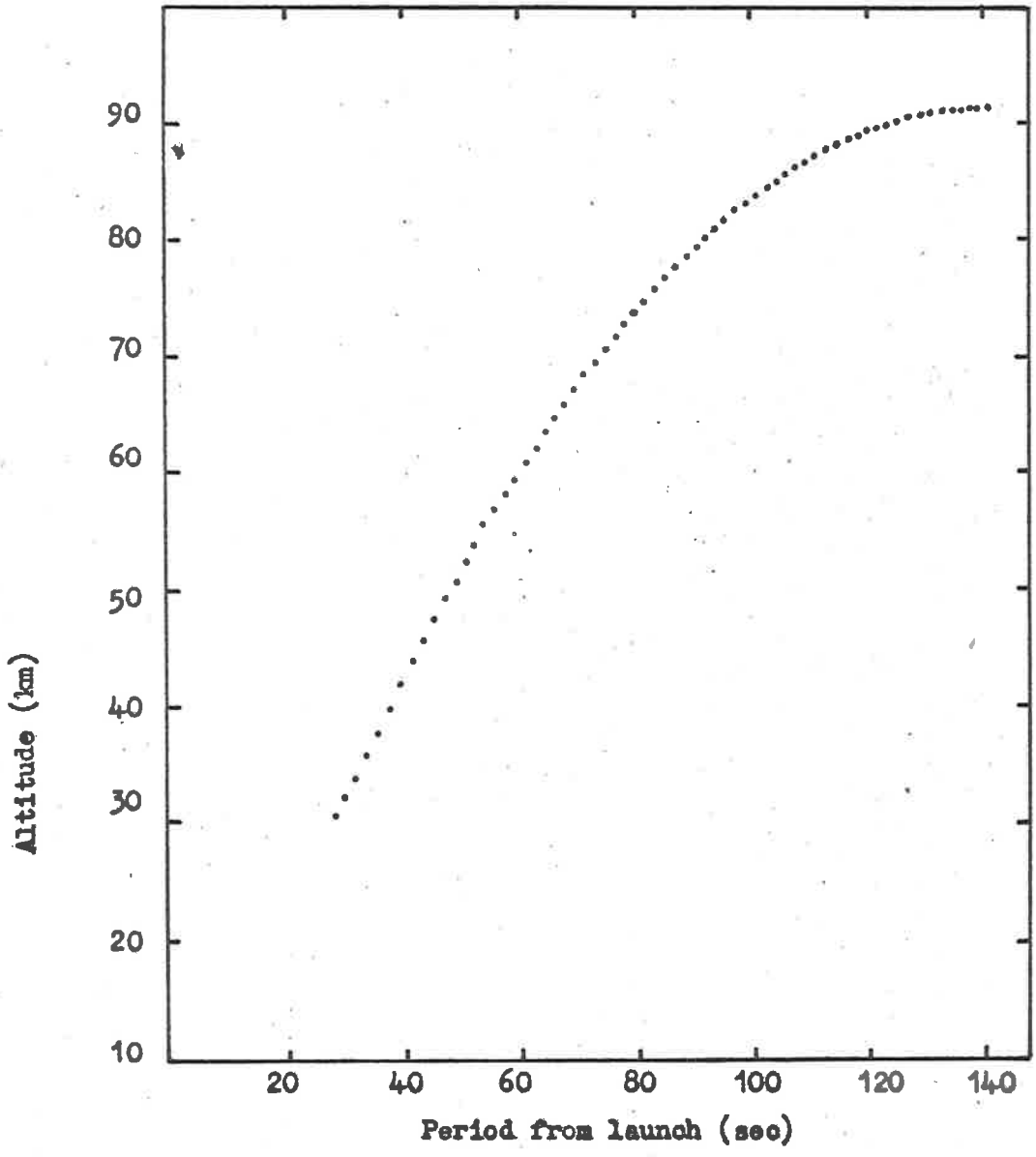

Figure 5.3 Caloulated variation of Altitude with time for HAD 312

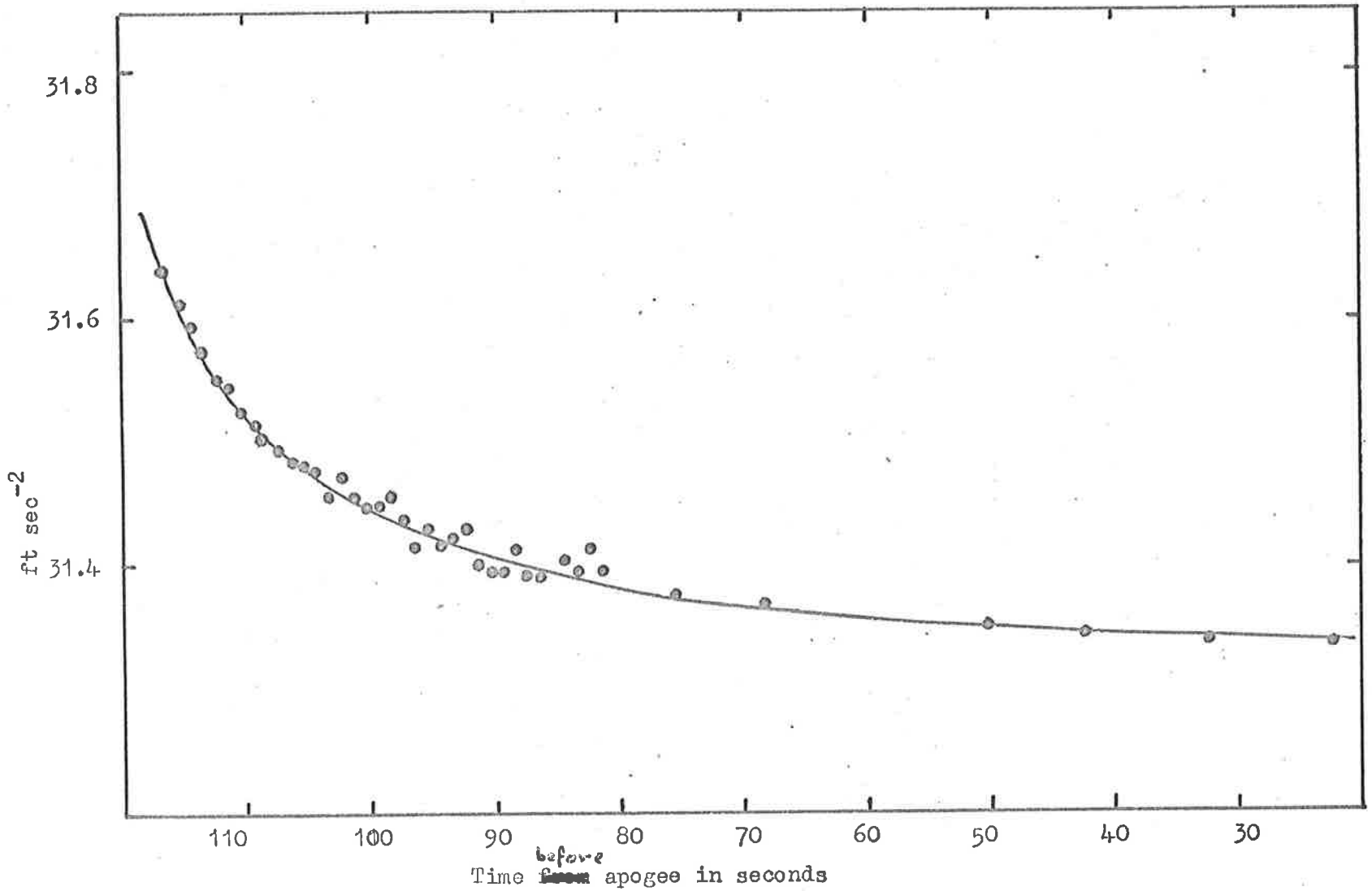

Figure 5.4 Variation of effective gravity with time from apogee.

for HAD 305 and HAD 312 is shown in Figures 5.5 and 5.6 respectively. All aspect angles shown relate to the upward legs of each flight. The attitude of HAD 305 on the downward leg of its flight was such that only the centre slot of the aspect sensor illuminated the sensor from which it was inferred that the aspect angle was too large to be measured while none of the photometers were illuminated. HAD 312, in the region close to scan numbers 40 and 55, made observations at large aspect angles such that the correction applied was large and sensitive to small errors of angle measurement. For this reason the accuracy of these points is poor. During the downward leg of the flight of HAD 312 slips in the reception of telemetry made reading of the records impossible.

5.6 Reduction of Results

The telemetry results were obtained from the Weapons Research Establishment in the form of film strips. Samples of the form of the film for (a) an aspect sensor and (b) a photometer are shown in Figure 5.1. The voltage output of each sensor was obtained by comparison of the

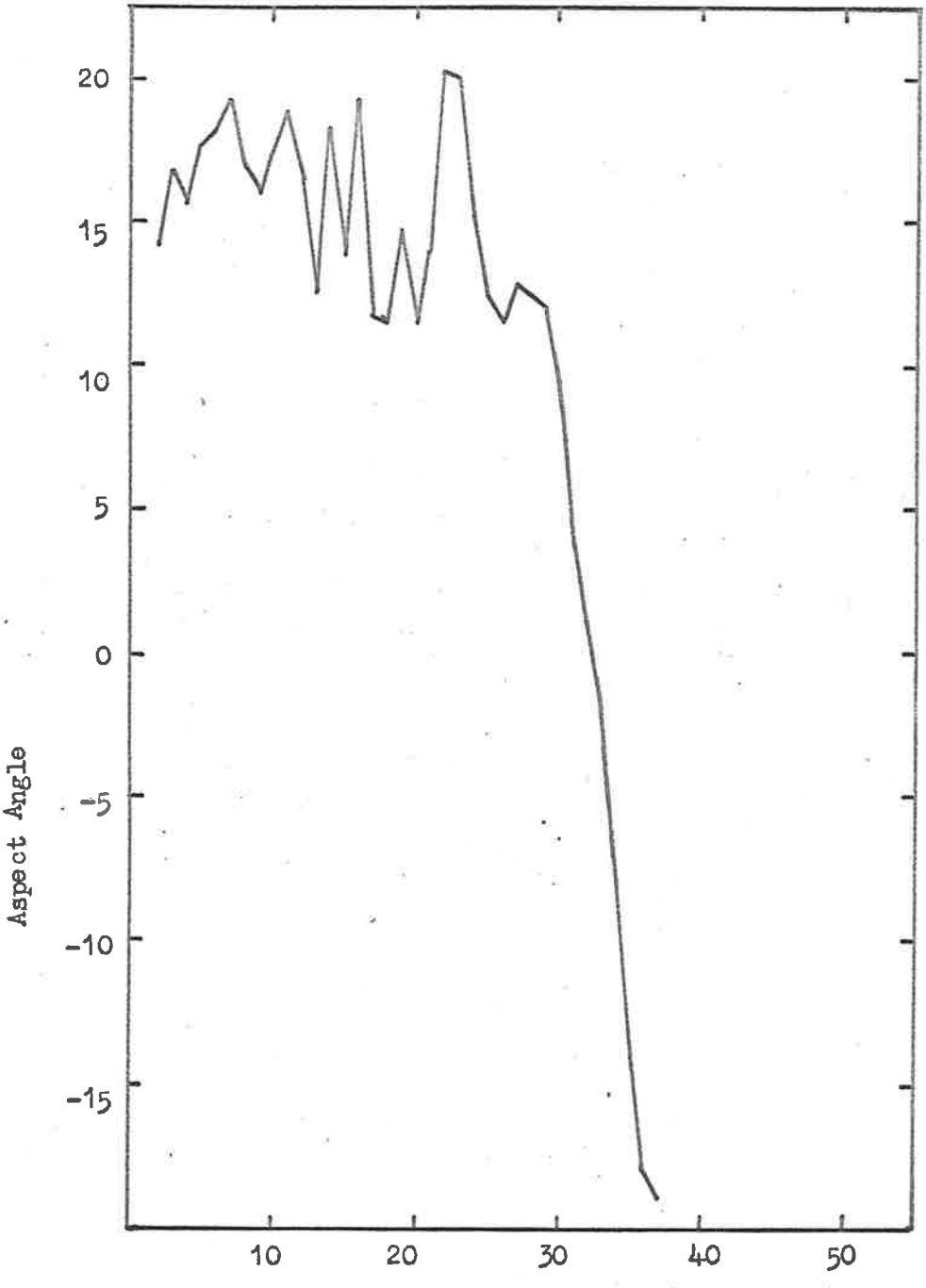

Figure 5.5 Aspect angle of source at each observed scan during flight of HAD 305.

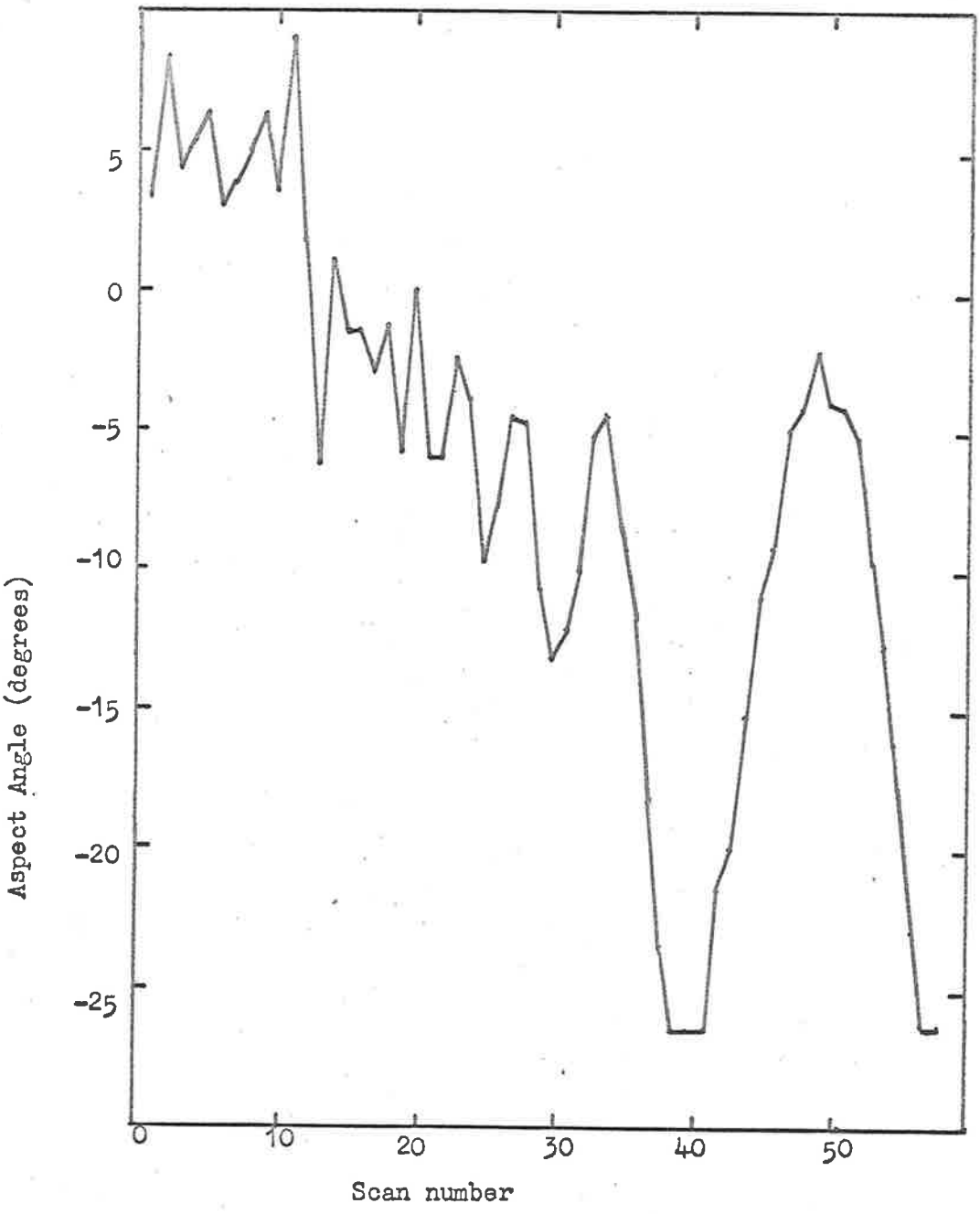

Figure 5.6 Aspect angle of the source at each observed scan during flight of HAD 312.

excursion of the amplifier channel at minimum aspect angle with the spacing between the 0. volt, 0.75 volt and 1.5 volt channels. The aspect angle correction for each sensor was then applied giving the equivalent output for normal incidence for each detector. As the first scan, in each case, was made below the expected position of the ozone maximum, so that only a small signal due to incident radiation could be expected, the voltage level associated with each first scan deducted from all succeeding readings as a zero correction. The voltage levels thus obtained were then related to the calibrations of the sensors to obtain the value of flux incident at the sensor at each scan. As the time of each scan was readable from the records by relating this time to the height vs time values already obtained, it was possible to plot the incident flux as a function of height for each sensor. This was done and a smooth curve drawn through the results of each sensor. The plotted results, together with the applied curves, are shown for each sensor in Figures 5.7 and 5.8 for HAD 305 and HAD 312 respectively.

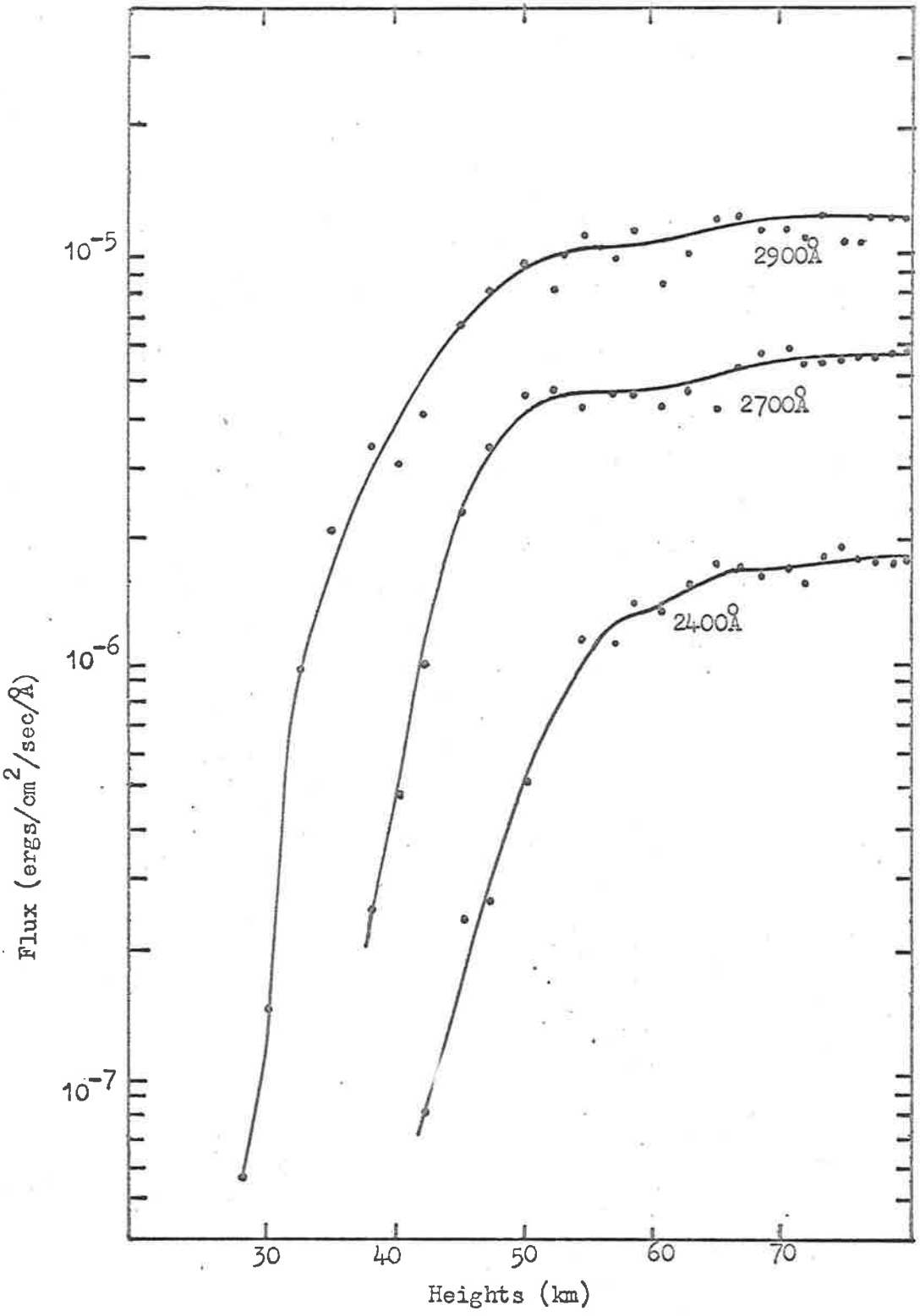

Figure 5.7 Variation of ultraviolet flux from the moon with height as measured from HAD 305.

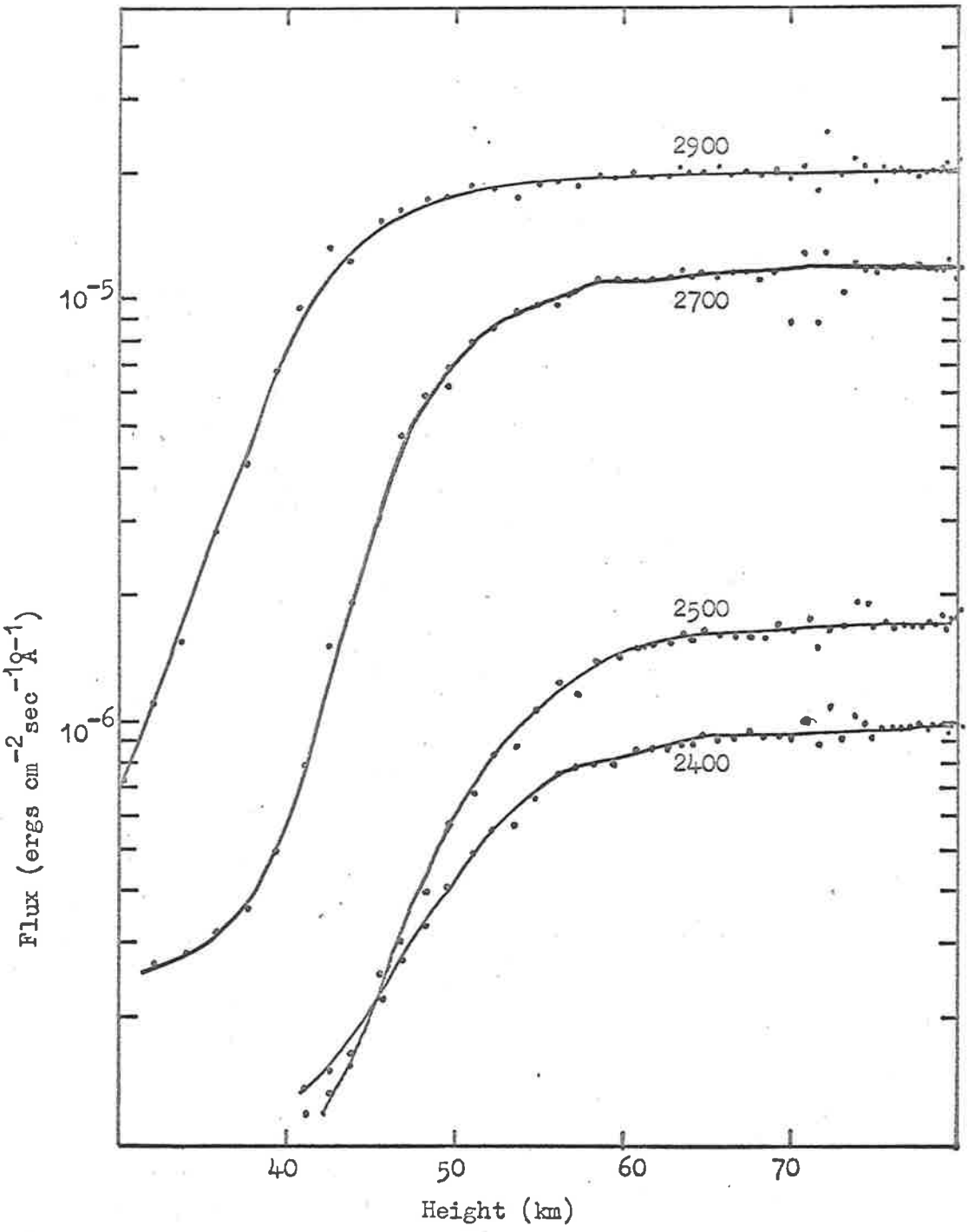

Figure 5.8 Variation of ultraviolet flux from the moon with height as measured from HAD 312.

CHAPTER 6

THE DISTRIBUTION OF NOCTURNAL ATMOSPHERIC OZONE

6.1 Curves of Variation of Intensity with Height

Curves of incident flux received by the photometers as a function of height were produced as described in Section 5.6 and shown in Figures 5.7 and 5.8. HAD 305 made 34 scans of the source which produced useful data between the heights of 28 kilometers and 84 kilometers while HAD 312 made 57 scans of the source between 23 kilometers and 78 kilometers. The difference in the scan rate is due to the difference in the uncontrolled roll rate of the vehicles involved. Because of the faster sampling rate of HAD 312 the data from this flight was accepted as defining more reliable curves though, owing to the high aspect correction applicable in the region of 70 kilometers, resulting from the large angles measured for the scans made at this level, referred to in Section 5.5, these portions of the curves are not so well defined. The values of flux, at even intervals of height, were tabulated from the smooth curves produced as above. The interval between entries was 2 kilometers for the results of HAD 305 and 1 kilometer for the results of HAD 312.

The values were listed in order of increasing altitude for each sensor. From these listings the ratio of each entry in a table to the next entry was obtained and listed against the altitude midway between that associated with the two entries. If the ratio is R the value of R is given by

$$\ln R(h) = -n\sigma l$$

where n = average number of absorbing particles per unit volume at height h

σ = effective cross section for absorption over the band pass of the sensor

l = path length of the radiation through the atmosphere determined by the interval of height Δh between the occurrence of the two values involved in the ratio

and $R(h)$ = ratio of the two entries at heights $h-0.5\Delta h$ and $h+0.5\Delta h$.

6.2 Determination of the value of the effective cross section

As the pass bands of the detectors covered approximately 100 Angstrom units to half power, an effective absorption cross section was required for each sensor. This was determined by taking values of the absorption coefficient over the whole acceptance band of the sensor (Inn and Tanaka 1959) for which the cross section was required, and weighting these values, as a function of wavelength, with the relative sensitivity of the sensor and the spectrum of the lunar radiation as estimated by Heddle (1963). If $a(\lambda)$ is the absorption coefficient at wavelength λ, $S(\lambda)$ is the relative sensitivity of the required sensor and $F(\lambda)$ is the estimated lunar spectral intensity, then a, the effective absorption coefficient is given by the relation

$$a = \frac{\int_{\lambda_1}^{\lambda_2} a(\lambda).S(\lambda).F(\lambda)\, d\lambda}{\int_{\lambda_1}^{\lambda_2} S(\lambda).F(\lambda)\, d\lambda}$$

The value of a so obtained is in the units of cm^{-1} at NTP. The value of the effective cross section may then be obtained by division by the number of particles per

TABLE 6.1

λ (A)	$a(\lambda)$ cm^{-1}	$S(\lambda)$	$F(\lambda)$
2002	8.61	.005	.002
2052	9.26	.005	.030
2102	14.7	.005	.039
2152	26.0	.010	.050
2202	48.4	.020	.064
2252	79.	.095	.080
2302	122.	.420	.098
2352	170.	1.01	.12
2402	219	1.265	.13
2452	267	1.055	.15
2502	299	0.85	.18
2552	311	.64	.26
2602	295	.39	.40
2652	256	.175	.67
2702	205	.005	1.20
2752	153	.020	1.3
2802	100	.005	1.4

TABLE 6.2

λ (A)	$a(\lambda)$ cm^{-1}	$S(\lambda)$	$F(\lambda)$
2300	120	.86	.098
2350	168	2.24	.114
2400	216	6.44	.130
2450	265	15.36	.151
2500	299	18.40	.180
2550	308	13.50	.258
2600	292	7.79	.400
2650	258	3.54	.660
2700	209	1.31	1.05
2750	155	.45	1.22
2800	100	.18	1.40

TABLE 6.3

λ (A)	a(λ) cm^{-1}	S(λ)	F(λ)
2502	299.	.005	.18
2552	311.	.015	.26
2602	295.	.03	.40
2652	256.	.08	.67
2702	205.	.39	1.2
2752	153.	.55	1.3
2802	100.	.455	1.4
2852	63.3	.315	1.8
2902	35.2	.10	3.0
2952	19.2	.025	3.5
3002	10.0	.01	4.2

TABLE 6.4

λ (A)	a(λ) cm^{-1}	S(λ)	F(λ)
2702	205.	.005	1.2
2752	153.	.015	1.3
2802	100	.055	1.4
2852	63.3	.255	1.8
2902	35.2	.95	3.0
2952	19.2	.85	3.5
3002	10.	.575	4.2
3052	7.	.210	5.0
3102	5.	.06	6.2
3152	3.	.02	7.1
3202	1.	.01	8.2

TABLE 6.5

Centre Wavelength Å	Effective Cross section cm^2
2400	9.29×10^{-18}
2500	10.00×10^{-18}
2700	4.32×10^{-18}
2900	0.825×10^{-18}

cm^3 at NTP, i.e. Loschmidts Number which is 2.689×10^{19}.

The values of $a(\lambda)$, $S(\lambda)$, and $F(\lambda)$ used for sensors centred at 2400Å, 2500Å, 2700Å and 2900Å are listed in Tables 6.1, 6.2, 6.3 and 6.4 respectively. These tables have been shortened, the actual interval used being 10Å. The derived value of the effective cross sections used are listed in Table 6.5.

6.3 Determination of the Density vs Height Profiles

As has been shown in Section 2.8 the path length of the radiation may be approximated by the height interval multiplied by the secant of the zenith angle of the source, provided that this angle is less than 70°. Using this approximation the average number density over the height interval was determined from the following relation:

$$n = \frac{\ln R(h)}{-\sigma . \Delta h \sec\theta}$$

where θ is the zenith angle of the source at the time of measurement. The height interval employed for HAD 305 was 2 kilometers and the zenith angle was 67° while the

height interval used for HAD 312 was 1 kilometer owing to better resolution obtained by high roll rate, and the zenith angle was 62° 30′.

The results obtained for the individual sensors for each flight are shown in Figures 6.1 and 6.2 for HAD 305 and HAD 312 respectively. Due to the large difference in effective cross sections for the different sensors, each sensor is suited to give information more effectively at different numerical densities. For example, the sensor centred on 2900Å, where the cross section is small, is most effective in the region of high number density but is rather insensitive in regions of low density. For this reason, the results presented in Figures 6.1 and 6.2, have been selected according to detector and combined to give the final results as presented in Figure 6.3.

6.4 Comparison with other High Atmospheric Ozone Results

Measurements of the high altitude ozone distribution have been made by other workers. These measurements have been made over a range of local times and by a variety of methods. A brief summary of these measurements is given in Table 6.6.

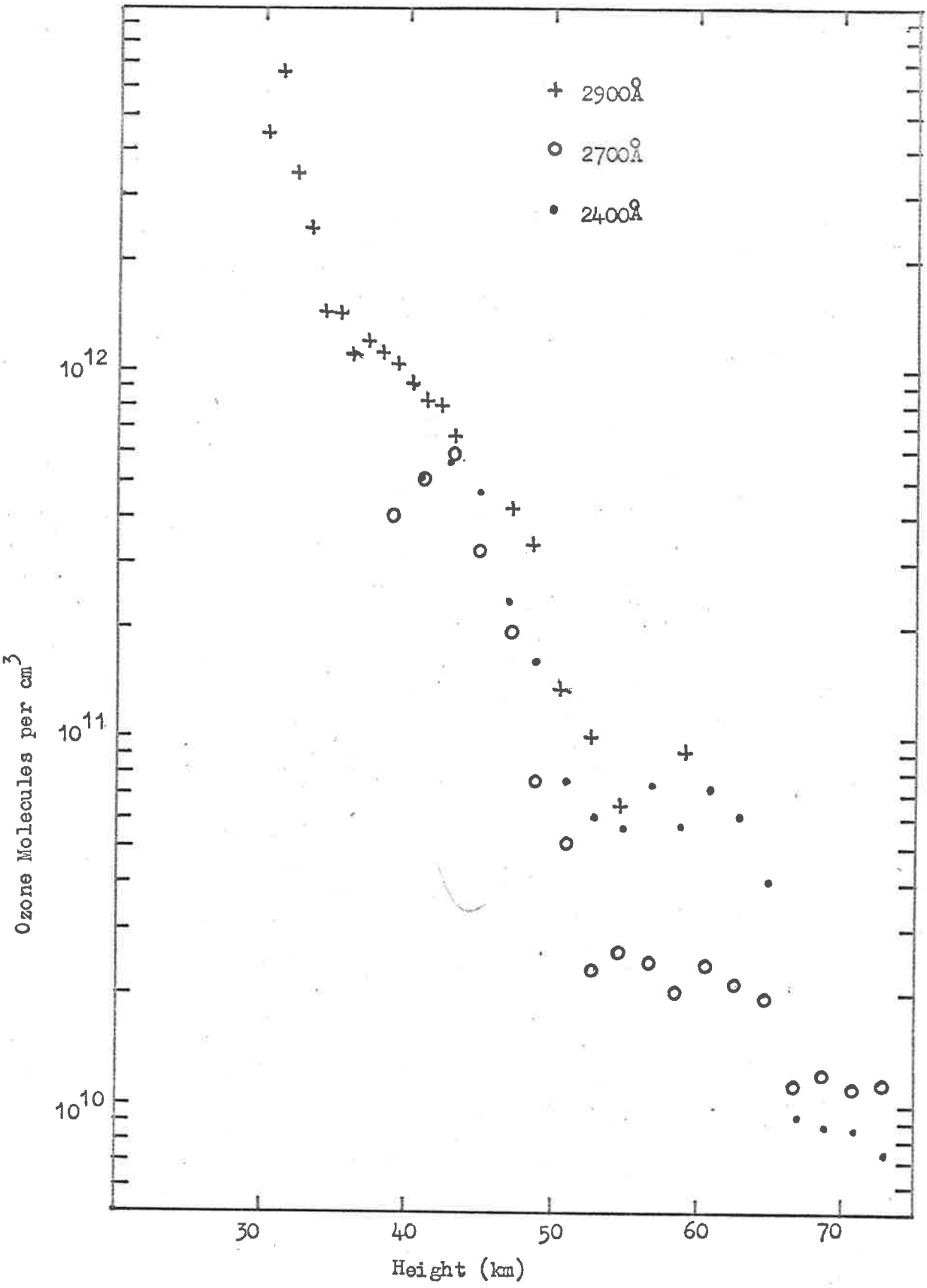

Figure 6.1 Ozone density as calculated from each sensor carried in HAD 305.

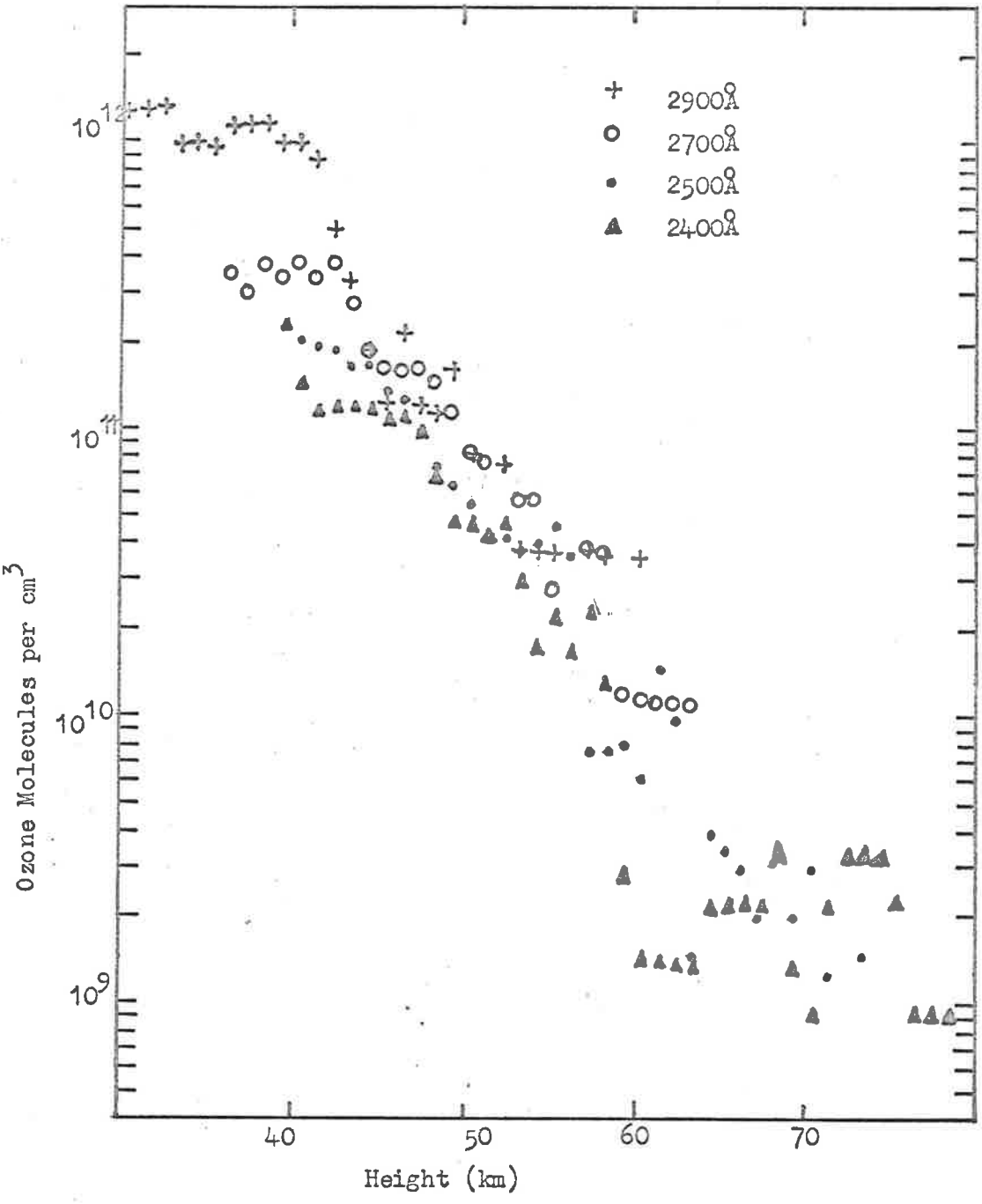

Figure 6.2 Ozone density as calculated from each sensor carried in HAD 312.

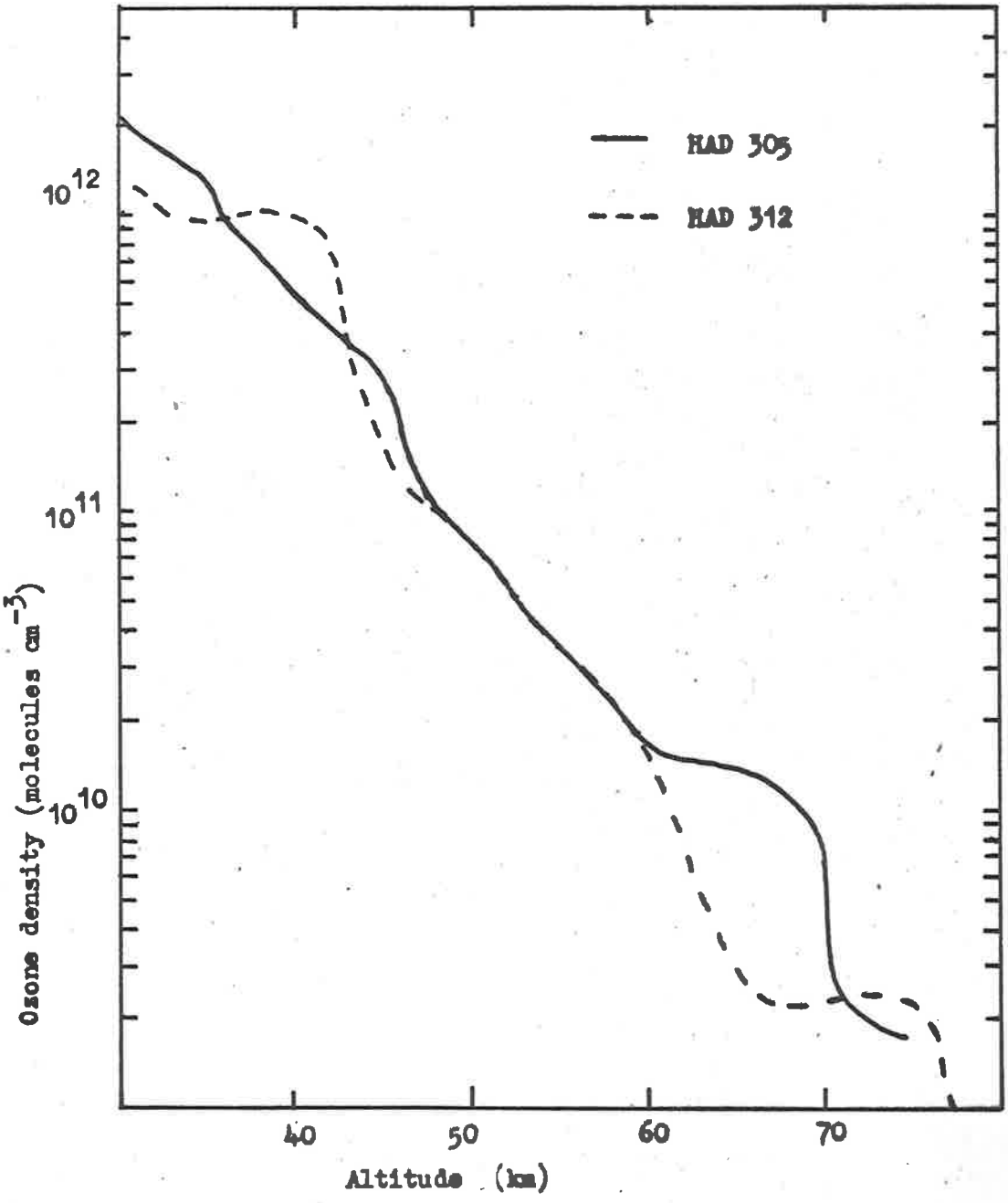

Figure 6.3 Nocturnal ozone density as measured above Woomera by HAD 305 and 312.

TABLE 6.6

Author(s)	Time of Observation	Method (briefly)
Johnson et al (1952)	Day	Rocket borne photgraphic spectrophotometry.
Venkateswaren et al (1961)	Night	Ground based modified Umkehr observation of an artificial satellite.
Rawcliffe et al (1963)	Day	Grazing incidence photometry from a satellite.
Miller and Stewart (1965)	Day	Grazing incidence photometry from a satellite.
Randhawa (1966a)	Day	Rocket borne chemiluminescent sonde.
Randhawa (1966b)	Night	Rocket borne chemiluminescent sone.
Reed and Scolnik (1964)	NNight	Rocket borne airglow photometry.
Poloskov et al (1967)	Day	Rocket borne photometry of scattered solar radiation.
Poloskov et al (1967)	Eclipse	Rocket borne photometry of scattered solar radiation.
Poloskov et al (1967)	Night	Rocket borne lunar photometry.

The results of these investigations have been presented in a number of different units by the authors. In order to present the results in a form suitable for comparison, all results have been reduced to the units of molecules per cubic centimetre. All the results pertaining to daytime measurements are presented in Figure 6.4. It may be seen that there is fair agreement between the values obtained for the number density of ozone molecules existing in a daylit atmosphere. This may be due to the intensity of direct sunlight compared to any background in the case of absorption measurements. The results obtained during night time are shown in Figure 6.5, including the results of the present investigation and the daytime results obtained by Johnson et al (1952) as representative of that condition.

In the case of the nocturnal measurements, however, a wide variance of results occurs. The result obtained by Poloskov et al (1967) seems excessively high, particularly at greater altitudes, as such variations would be measurable by an Umkehr method. The profile produced by Venkateswaren et al (1961) also indicates levels some orders of magnitude greater than the day time level observed by Johnson et al (1952) at an altitude of 55 to 60 kilometers where the theoretical work of Hunt (1966)

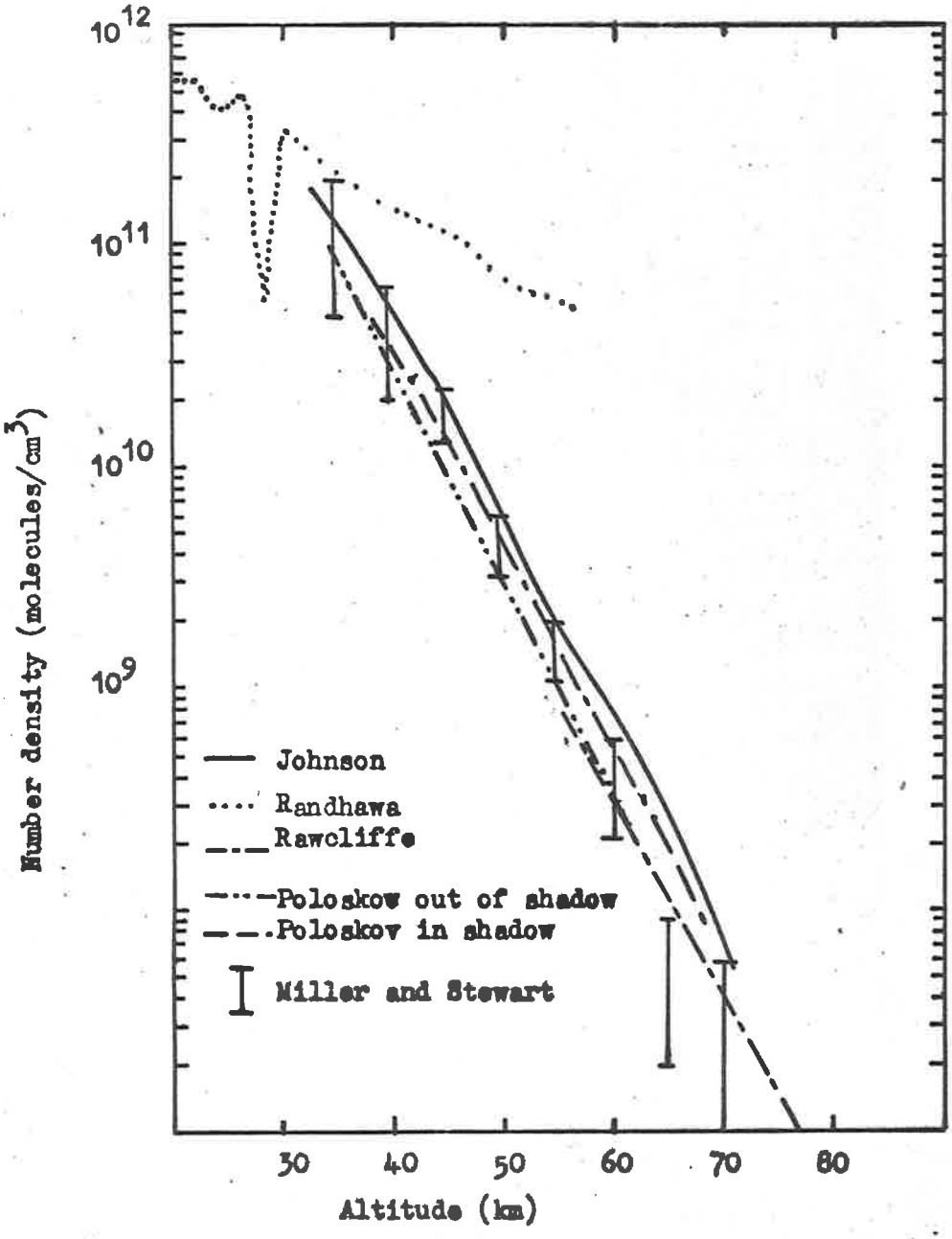

Figure 6.4 Results of some measurements of ozone density in a sunlit atmosphere.

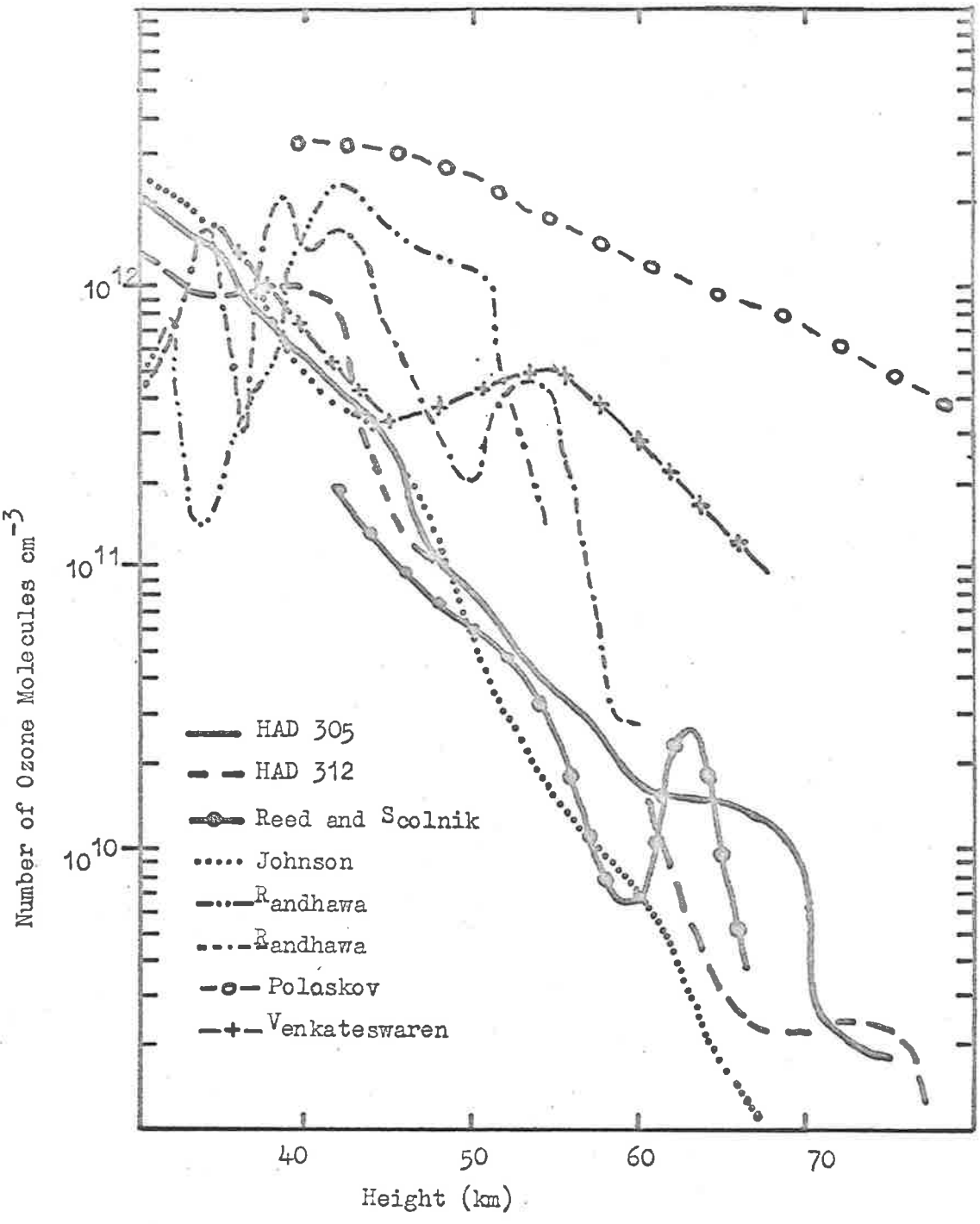

Figure 6.5 Measured values of nocturnal ozone distribution together with results obtained for a sunlit atmosphere by Hohnson et al (1952).

suggests there is no diurnal variation. Both the work of Poloskov et al (1967) and that of Venkateswaren et al (1961) was based on measurements of absorption in the Chappuis bands of the ozone absorption spectrum. It is to be expected that measurements made in this region would not be as well determined as measurements made in the Hartley bands as the ratio of peak absorption cross section in the Chappuis bands to that of the Hartley bands is approximately 4×10^{-4}. The results of Randhawa (1966b) have been extracted from his graphical presentation and may not be a fair representation of the figures he obtained, particularly at higher levels. The reason for this is the linear form of the plots, making errors in reading the values obtained above 45 kilometres comparable with the values themselves. Despite this uncertainty, the trend of Randhawa's results is towards the values obtained by Reed and Scolnik (1964) and the present results.

6.5 A possible 40-50 km Winter Maximum

An interesting feature of the results of Randhawa is the secondary maximum occurring in the region of 40 to 45 kilometres. This feature is most prominent in

his result for November 23rd, 1965. No such feature is visible in the results of Reed and Scolnik (1964), in the summer measurement of the present results or in the daylit measurement of Johnson et al (1952), although the results of HAD 312 do appear to show a region of constant density at 40 kilometres. A similar feature is suggested by Randhawa's result for a daylit atmosphere, (Randhawa 1966a) although loss of signal occurred as his sonde went through the height range 40 to 30 kilometres. If the times of measurement are transposed to equivalent Southern Hemisphere seasonal months the dates would be

Author	Month	Equiv South Month
Johnson et al	June 14th	December 14th
Randhawa (a)	February 3rd	August 3rd
Randhawa (b1)	October 25th	April 25th
Randhawa (b2)	November 23rd	May 23rd
Reed and Scolnik	May 27th	November 27th
HAD 305		December 7th
HAD 312		August 31st

It should be noted that all the results which tend to show a maximum in the 40 kilometre region were taken in the late autumn-winter season, the effect not being apparent during other parts of the year, while the

strongest indication occurred for the measurement taken in the southern equivalent of May 23rd. If now the results of zonal wind measurements in this region by Rofe (1966) are looked at on a monthly basis as a function of height, it is found that the wind shear, measured as the vertical velocity gradient with height, is a maximum in the late autumn-winter period. This can be seen by reference to Figure 6.6, from Rofe (1966) and noting that the wind velocity iso lines are horizontal for the period May through to August, the velocity gradient being in the vertical direction while the iso lines are almost vertical in the November-December period, indicating little variation of wind velocity with altitude. If turbulent cells are assumed to be associated with such a wind shear, such cells, by altering the diffusion rates, could account for the existence of this subsidiary maximum. Confirmation of the feature needs to be obtained by a series of measurements, designed to study this portion of the atmosphere. Murgatroyd (1963), in a study related to the energy available for the production of such eddies finds that such structures would be of large scale, requiring large area coverage in any systematic investigation. Such regions of higher ozone mixing ratio, as suggested by these results, may provide one of the methods of transport of ozpne from the region of

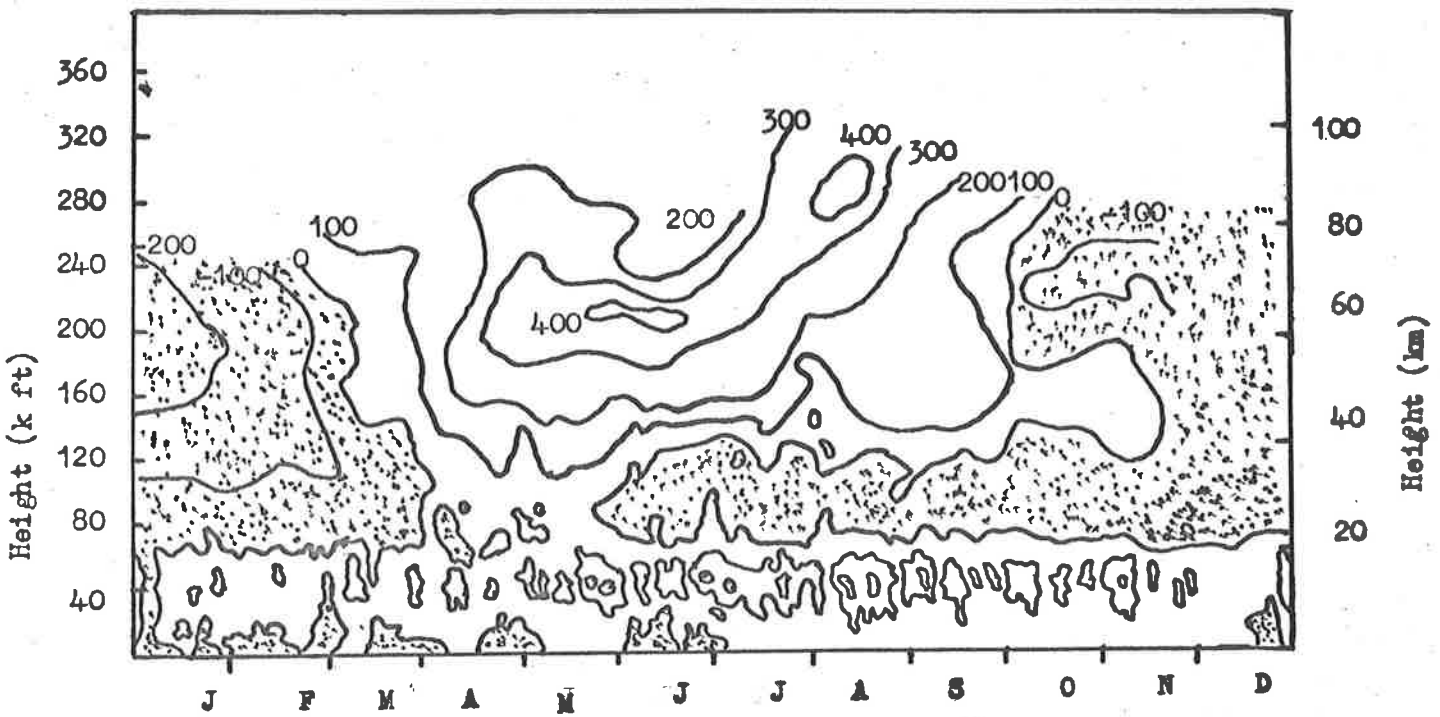

Figure 6.6 Woomera Zonal Wind Structure (ft sec^{-1}) 1964-65. After Rofe 1966. (Positive wind direction is from the west).

photochemical equilibrium, above approximately 50 kilometres, to the region of the maximum, at 20 to 30 kilometres. Here atomic oxygen concentrations are so low, arising only from dissociation of ozone by radiation in the Chappuis bands, that recombination with diatomic oxygen is so rapid that the oxone concentration remains almost constant. Losses of ozone from this lower region, due to chemical interactions with aerosols and other tropospheric gases, must be made up and seasonal dumping, due to large scale eddies, would provide a mechanism to explain the high latitude late winter maximum in total ozone that is observed.

6.6 Theoretical Diurnal Variations in the Ozone Number above 55 Kilometres

At altitudes of 25 to 30 kilometres, atomic oxygen is produced by dissociation of ozone and is lost by combination with diatomic oxygen, thus leaving the concentration of ozone relatively constant. At heights above approximately 55 kilometres this is no longer the case. Here atomic oxygen is produced by the photodissociation of a number of atmospheric components, the

major contribution coming from molecular oxygen, the contribution from ozone being small owing to the low concentration of this gas at these heights relative to molecular oxygen. In the absence of dissociating radiation during the night, the atomic oxygen is removed by collisional recombination reactions. In a pure oxygen atmosphere the reactions are

$$1.\quad O + O_2 + M \xrightarrow{k1} O_3 + M$$

$$2.\quad O + O + M \xrightarrow{k2} O_2 + M$$

$$3.\quad O + O_3 \xrightarrow{k3} 2\,O_2$$

$$4.\quad O + O \xrightarrow{k4} h\nu + O_2$$

$$5.\quad O + O_2 \xrightarrow{k5} h\nu + O_3$$

where k1, k2 etc are the reaction rates of the associated reactions, and have the values (Keneshea, 1967):

$$k1 = 3.2 \times 10^{-35} \exp(900/T) \quad cm^6\,sec^{-1}$$

$$k2 = 5.0 \times 10^{-32} \; T^{\frac{1}{2}} \quad cm^6\,sec^{-1}$$

$$k3 = 5.0 \times 10^{-10} \exp(-2800/T) \quad cm^3\,sec^{-1}$$

$$k4 = 1.0 \times 10^{-21} \quad cm^3\,sec^{-1}$$

$$k5 = 1.0 \times 10^{-21} \quad cm^3\,sec^{-1}$$

The relative importance of the reactions may be determined in an approximate manner, as follows.

Consider the temperature over the region 60 to 100 kilometers to be 225°K, this being a mean value for the range, and the O_3 number densities to be given by the relation

$$N(O_3) = N(O_3)_{60\ km}\ 10^{\frac{-h-60}{H}}$$

which, from the results of daytime measurements, (see Table 6.6) has the value

$$N(O_3) = 10^{12}.10^{\frac{-h-60}{11.5}} \text{ molecules cm}^{-3}.$$

The values for the number densities of O, O_2 and M (= O_2+N_2) are taken from Keneshea (1967).

When the value of 225°K is assumed for the temperature in the reaction region, the temperature dependent rate constants are

$$k1 = 3.2 \times 10^{-33}$$

$$k2 = 3.3 \times 10^{-33}$$

$$k3 = 2.0 \times 10^{-15}$$

and the number densities are, in units of molecules cm^{-3} as in Table 6.7.

TABLE 6.7

Altitude	60	70	80	90	100 kms
O	4.8×10^{10}	6.4×10^{10}	8.5×10^{10}	1.25×10^{11}	5.0×10^{11}
O_2	1.5×10^{15}	7.5×10^{14}	7.95×10^{13}	1.3×10^{13}	2.0×10^{12}
O_3	1.0×10^{10}	1.35×10^{9}	1.82×10^{8}	2.46×10^{7}	3.26×10^{6}
M	7.2×10^{15}	2.35×10^{15}	3.75×10^{14}	6.3×10^{13}	1.0×10^{13}

(The number densities of molecules per cm^3 as a function of altitude.)

All the reactions are proportional to the number density of O.

If n1 = number density of O

n2 = " " " O_2

n3 = " " " O_3

nM = " " " Third body particles,

the value of the ratio of reaction rate to number density of O for the reactions 1 to 5 are given by

1. 1.n2.nM.k1
2. 1.n1.nM.k2
3. 1.n3.k3
4. 1.n1.k4
5. 1.n2.k5

which, with the rates and number densities as above, have the values as listed in Table 6.8 at the heights considered.

TABLE 6.8

Reaction	60	70	80	90	100 kms
1	3.46×10^{-2}	5.8×10^{-3}	9.85×10^{-5}	2.7×10^{-6}	6.6×10^{-8}
2	1.14×10^{-7}	4.95×10^{-8}	1.05×10^{-7}	2.6×10^{-8}	1.65×10^{-8}
3	2.0×10^{-5}	2.7×10^{-6}	3.64×10^{-7}	4.92×10^{-8}	6.52×10^{-9}
4	4.8×10^{-11}	6.4×10^{-11}	8.5×10^{-10}	1.25×10^{-10}	5.0×10^{-10}
5	1.5×10^{-6}	7.5×10^{-7}	7.95×10^{-8}	1.3×10^{-8}	2.0×10^{-9}

From the Table 6.8 it may be seen that reaction 1 is predominant at all levels up to 100 kilometres although, at 100 kilometres, the two reactions 1 and 2 are comparable in rate. Because of the predominance of reaction 1, approximations of the rates of change of atomic oxygen and ozone densities are given by

$$\frac{d(n1)}{dt} = - n1.n2.nM.k1 \qquad \ldots(6.1)$$

$$\frac{d(n3)}{dt} = n1.n2.nM.k1 \qquad \ldots(6.2)$$

Equation 6.1 may be integrated directly to give

$$n1 = n1_0 \exp.(-n2.nM.k1t) \qquad \ldots(6.3)$$

Where $n1_0$ is the number density of atomic oxygen immediately preceding sunset, and t is the time in seconds since sunset.

From the values given in row 1 of Table 6.8 and the relation

$$t_{\frac{1}{2}} = \frac{0.693}{n2.nM.k1} \text{ seconds,}$$

where $t_{\frac{1}{2}}$ is the half life of the atomic oxygen content in radiation free conditions, the half life of oxygen are obtained as

kms	secs
60	20
70	119
80	7.7×10^3
90	2.56×10^5
100	1.05×10^7

If the period that is radiation free is taken to be 4.0×10^4 sec, it can be seen that all the atomic oxygen will have recombined within the space of a few minutes at 60 and 70 kilometers, some 3% will remain in the atomic state at the end of the night at 80 kilometers, while only a few percent will have recombined at heights above 90 kilometers.

Equation 6.2 may be integrated in the form

$$n3 = k1.n2.nM.n1_o \int_o^t \exp(-n2.nM.k1.5)\ dt + n3_o$$

$$= n1_o [1.0-\exp(-n2.nM.k1.5)] + n3_o$$

where $n3_o$ is the number of ozone molecules prior to sunset as in Table 6.7.

From this relation the number of ozone molecules have been calculated as a function of time for the height range from 60 to 100 kilometers and the results of these calculations are shown in Table 6.9 and plotted in Figure 6.7

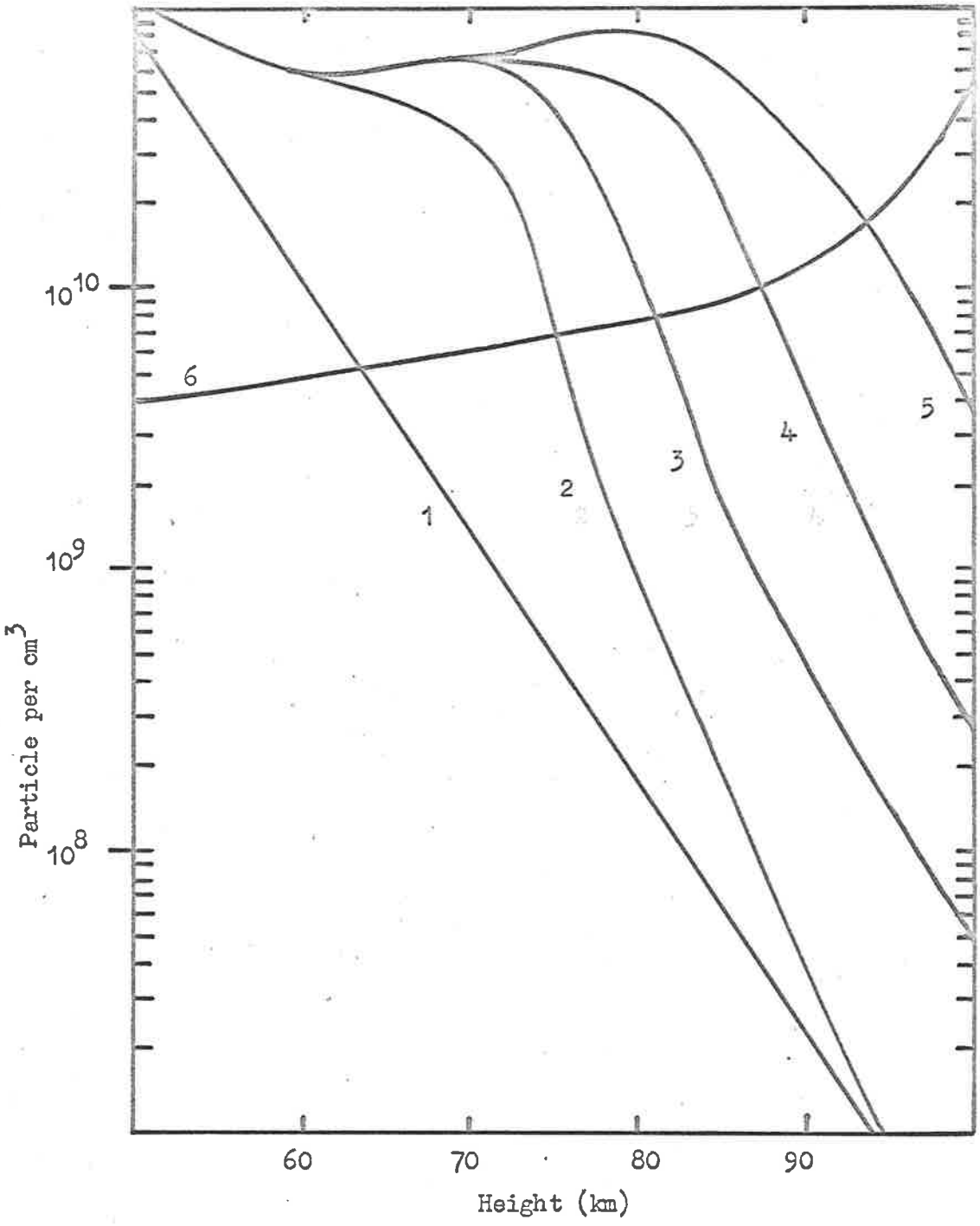

Figure 6.7 Ozone density at time t after removal of the radiation field according to simple theory. 1. t=0 sec. 2. $t=10^2$ sec. 3. $t=10^3$ sec. 4. $t=10^4$ sec. 5. $t=10^5$ sec. Curve 6 shows sunlit equilibrium concentration of atomic oxygen.

TABLE 6.9

Number of Ozone Molecules as a Function Of Time and Height

Height	10^2 sec	10^3 sec	10^4 sec	10^5 sec
60 km	5.6×10^{10}	5.8×10^{10}	5.8×10^{10}	5.8×10^{10}
70 km	3.8×10^{10}	6.5×10^{10}	6.5×10^{10}	6.5×10^{10}
80 km	8.25×10^{8}	8.6×10^{9}	5.36×10^{10}	8.35×10^{10}
90 km	5.0×10^{7}	3.6×10^{8}	3.75×10^{9}	3.0×10^{10}
100 km	3.2×10^{6}	5.3×10^{7}	2.5×10^{8}	3.75×10^{9}

It may be seen from Figure 6.7 that there is an increase in the ozone number density at high altitudes at night, the peak rising from 70 to 90 kilometers as the radiation free period increases. At heights above 100 kilometers, the situation would become more complex as other reactions competed for the available supply of molecular oxygen.

The account given above is a gross over simplification of the actual processes taking place, the main simplification being that a purely oxygen atmosphere was considered. More realistic treatments have been made by a number of

workers in recent years. Two such studies are those of Hunt (1966) and Keneshea (1967).

Hunt has considered the effect of the water vapour in the atmosphere and the products of photo-disintegration of this water vapour. Some of the reactions listed by Hunt which are relevant to the ozone concentration are

6. $H_2O + h\nu \rightarrow OH + H \quad (\lambda < 2390\text{Å})$

7. $OH + O_3 \rightarrow HO_2 + O_2$

8. $HO_2 + O_3 \rightarrow OH + 2O_2$

Reaction 6, occurring during the daylight period, supplies the hydrogen and hydroxyl components for the later reactions, which are important in the absence of radiation. Reactions 7 and 8 are found by Hunt to be the more important of the numerous reactions taking place. These two reactions form a closed loop which removes the ozone molecules in each cycle, and so reduce the net production rate of O_3.

The study by Keneshea excludes all mention of hydrogen and hydroxyl reactions and treats reactions involving nitrogen, various nitrogen oxides and various electron-ion

reactions. The lower limit of Keneshea's study is 60 kilometers and is extended to 120 kilometers. At the altitudes between 60 and 80 kilometers the effect of nitrogen-oxygen and electron-ion reactions is small when applied to the ozone content, the principle reaction in this height range considered by Keneshea being reaction 1, noted previously. Above 100 kilometers, although the O_3^- ion exists and is strongly reactive with N_2 and the NO^+ ion, these reactions resulting in loss of O_3, the ion to neutral ratio is of the order of 10^{-4} and so causes little loss to the total ozone number density.

A laboratory study by Fehsenfeld et al (1967) has measured reaction rates for reactions of atmospheric interest, and related these to possible interactions in the D region near 70 kilometers. Although the reaction rates found by Fehsenfeld are high once the ion is supplied, the D region electron density being of the order of 10^3, it is unlikely that these will affect the ozone density near the D region heights.

A further possible reactant in the upper atmosphere is introduced by Fehsenfeld, this being CO_2 with the assumption that the CO_2 mixing ratio is constant with height at the value at the earth's surface, this being of order 3×10^{-4} by volume.

In none of these studies has the effect of atmospheric movements due to thermal absorption in the regions of maximum ozone formation and dissociation about 70 kilometers been considered. Lindzen (1967) has shown that solar generated thermal tides should occur in the upper atmosphere, these being dependent on season and latitude. Lindzen uses an ozone distribution of the form $e^{0.0116(z-z_1)} \text{ Sin } \frac{\pi}{60}(z-z_1)$ $z_1 = 18$ km $z \leq 78$ km, in his determination of the wind motions and it is possible that application of one of the more detailed models as that of Hunt or Keneshea would produce finer detail. A combination of the effects considered by Hunt, Keneshea and Lindzen would also be an advance in the prediction of atmospheric densities at high altitudes.

6.7 The Observed Nocturnal Distribution of Ozone at High Altitude

The results of the flights of HAD 305 and HAD 312 are presented in Figure 6.8 together with the results of Reed and Scolnik (1964) for their night time measurements, the theoretical values of Hunt (1966) and the day time result of Johnson et al (1952) for comparison. An obvious feature

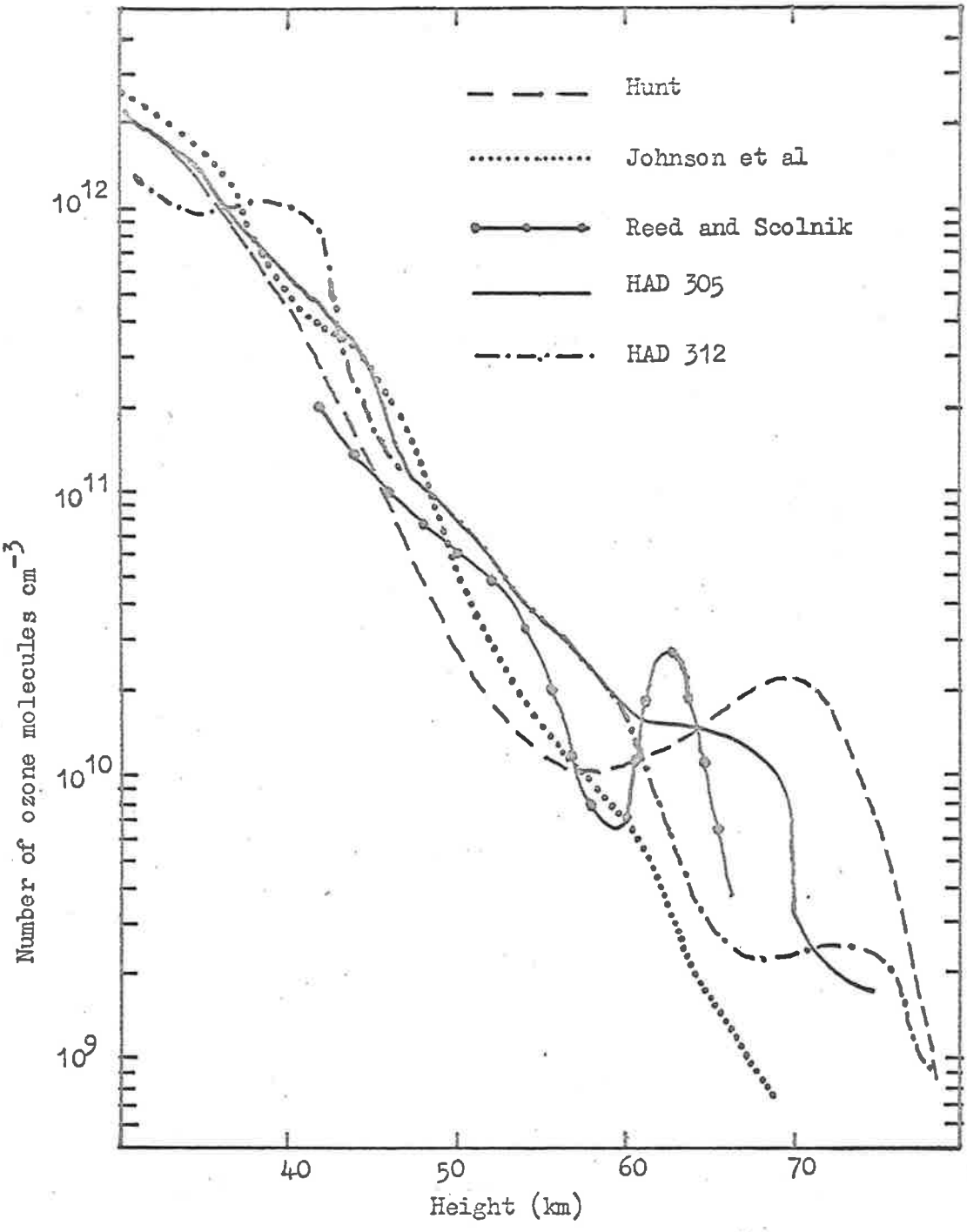

Figure 6.8 Nocturnal distribution of ozone molecules including the theoretical results of Hunt 1966. The daylit results of Johnson et al are included for comparison.

is the wide variation of the measured densities above 60 kilometers, while the number densities below this altitude are in good agreement. That this is to be expected has been shown in Section 6.6 in that the active region of the atmosphere as far as ozone is concerned lies in the height range 60 to 80 kilometers. The results of HAD 312 show very little activity below 70 kilometers compared with those of Reed and Scolnik and HAD 305. A possible explanation of this observation lies in the time of firing.

HAD 312 was fired at 1938 hrs Australian Central Standard Time, this being equivalent of 1008 hrs Universal Time. At longitude 136° 31' East and latitude 30° 35' South, the time of ground sunset, as calculated from the Astronomical Ephemeris was 1755 hrs Local Time corrected for longitude while the corrected Local Time of launch was 1914 hrs. The launch therefore, took place 1 hour 19 minutes after ground sunset. Assuming that the effective sunset for ozone dissociation occurs as the sun sets at 40 kilometers, the sunset horizon at 70 kilometers, giving an effective height above the 40 kilometer level of 30 kilometers, is given as

$$\text{(horizon distance (km))} = (15 \times \text{Ht above level (metres)})^{\frac{1}{2}}$$

$$= 670 \text{ kms.}$$

A horizon at a distance of 670 kilometers would delay the sunset by approximately 27 minutes. According to these calculations the measurements made in the region about 70 kilometers were made at a time 52 minutes after sunset below the 40 kilometer level. This period of 27 minutes while still effective for the dissociation of ozone, would be effective radiation free time for reactions producing atomic oxygen through dissociation of molecular oxygen. The values quoted relate to complete cut off of the radiation. Attenuation will be high before the actual sunset but the time lag between the effective radiation cut off will remain through this attenuation period.

Because of the time lag between ground conditions and those at high levels in the atmosphere, the assumption may be made that the equilibrium levels of nocturnal number density had not been reached at the time measurements were made by HAD 312. A comparison between the results of HAD 312 and those obtained by Poloskov et al (1967) during an eclipse are shown in Figure 6.9, together with the results of Poloskov et al for daylit comparison. It may be seen that there is correlation between the eclipse values and those of HAD 312 in that the increase at 70 kilometers is suggested. The difference in the conditions of illumination, the eclipse being a simultaneous cut off at

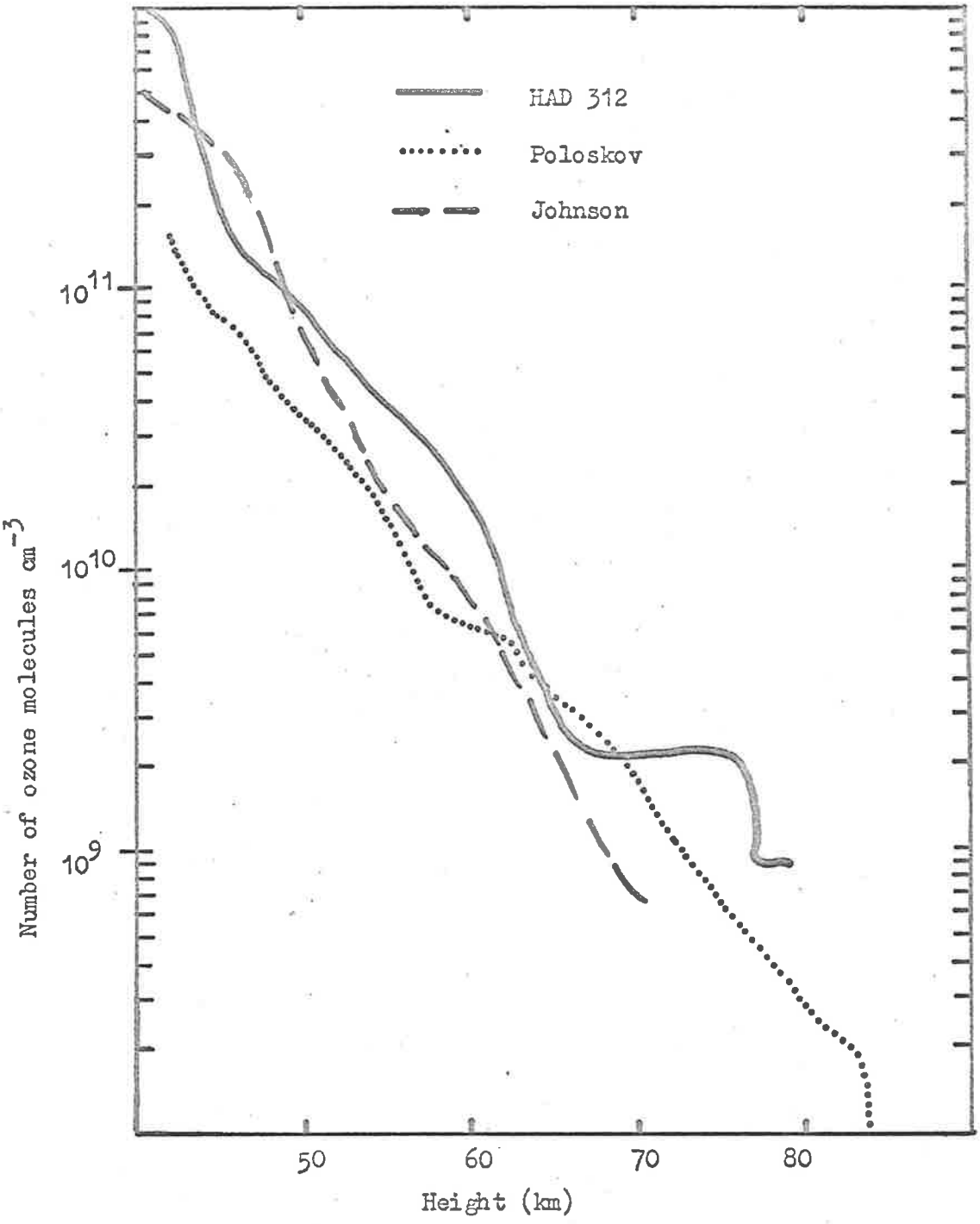

Figure 6.9 Comparison of results of HAD 312 (post sunset), Poloskov et al, (Eclipse) and Johnson et al (Sunlit).

all wavelengths, removes the possibility of complete agreement.

The results of HAD 305 and Reed and Scolnik are in qualitative agreement although the integrated number of ozone molecules above 55 kilometers is considerably less in the case of Reed and Scolnik.

The implication of the observations is that while there is qualitative agreement between the observations and the theoretical predictions of number densities above 55 kilometers, the calculated production rates appear to be too high to satisfy the range of density suggested by the measurements. This does not include the measurements of Venkateswaren and Poloskov which have been left out of this comparison as results are questionable as discussed in Section 6.4.

6.8 Suggested Directions of Future Upper Atmosphere Ozone Studies

Due to close association of ozone density with the composition of, and ractions in the atmos here between 30 and 100 kilometers and comparative ease of measurement

compared to the other trace species such as atomic oxygen and hydroxyl, regular measurement of this gas is probably the most effective check on model atmosphere calculations. The photometric method of measurement, being independent of the conditions in the immediate neighborhood of the vehicle and the dynamics of flow into any sampling chamber, is perhaps the best method of measurement. Requirements of this method, a suitable light source, high continuity of measurement, both of light received and response variables such as aspect angles, and high wavelength resolution, provide scope for further development.

The most effective region of the spectrum for photometric measurement is the Hartley absorption bands, centred on 2500Å. Refinements required of measurements are the studies of the effects of Rayleigh scattering at these wavelengths and the distribution and intensity of high atmosphere airglow. These have been neglected in the present study as the ratio of effective cross sections by number density per centimetre for ozone absorption to general atmospheric scattering is greater than 10^2 in the centre of the Hartley bands, while the lunar intensity is such that the air glow signal observed during the flights if negligible and hardly measureable.

Model atmospheric studies need to be extended to include greater detail in the chemical and photo reactions occurring as well as latitude variations and the effects of dynamic motions in the upper atmosphere.

CHAPTER 7

THE ULTRAVIOLET REFLECTIVITY OF THE LUNAR SURFACE

7.1 Introduction

The composition and structure of the lunar surface has become a matter of practical importance, in view of the planned landing of manned spaced craft on the surface of the satellite. One method of study is direct sampling and close photography by remotely controlled probes which are landed on the surface. While capable of detailed examination of the surface in the immediate neighborhood of the instrumentation, this method, because of the level of sophistication and costs involved, cannot be used in a general survey of the surface. It is necessary that such observations be supported by studies from the region of the earth. These studies may be of selected regions or of the total integrated surface area. Differences between the results of such observations would indicate the relative importance of the primordal lunar surface and the modification caused by the surface cover produced by the infall of meteoric matter. It is expected

that meteoric infall would result in a relatively uniform surface except in the case of large meteorites which, in the explosive dissipation of their kinetic energy, would remove any surface deposit, redistribute it and bare the primordal structure.

Among the methods of observation of the lunar surface that may be used from the vicinity of the earth are radio emission measurements in the decimeter to millimeter wavelength regions of the spectrum. Because of the difference in wavelength these studies make it possible to observe to some depth in the surface layer, the dielectric properties of the layer allowing transmission to a depth of a few wavelengths. Such studies, using the thermal spectrum, allow measurement of the thermal conductivity by measurement of the temperature as a function of time as the illumination conditions of the surface change as the moon rotates. Closely associated with the radio emission studies are the measurements made employing radar techniques. Dependent upon the beam width of the instrument used, radar will give a generalised picture of the surface over large areas or show the peculiarities of localised regions. One piece of information obtainable from radar studies is the polarising effect of the surface layers on radiation in the decimeter to centimeter region. Polarisation of reflected

solar radiation in the visible and near infrared wavelengths is also an observable quantity. The polarising properties of a surface are dependent upon the electrical and physical structure of the illuminated surface and the angles of incident and observed radiation. The latter two conditions are known and the response to the other variables varies with them although in a complex and interrelated manner. Other information obtainable from observations in the visible wavelength regions is the form of the reflection coefficient as a function of the direction of incident and observed radiation. The shape of the curve obtained from this relation places some restriction of form of the surface layer due to the strong peaking of intensity when observed and incident directions are the same. Photometry in the infrared is another source of information as to the temperature conditions of the surface, this wavelength providing information relating to the immediate surface layer. The combination of these results with those obtained from the radio measurements provides information as to the gradient of the thermal conductivity and hence of the variation of conditions with depth in the layer. The complexity of interpretation of such information is evidenced in a treatment by Gehrels (1964). The extraction of temperatures from measured fluxes depends upon the assumption of a black body spectrum.

A model, set up by Gehrels, includes a floating dust layer, transparent at the peak of solar radiation but involving radiative transfer theory to the emitted radiation. Some correlation between radar back scatter results and infrared temperature results have been reported by Thompson and Dyce (1966) which they have related to removal of a dust layer by relatively recent impacts from surface regions, exposing materials of different electrical properties. The suggestion is made that such measures may be related to the age of the features observed. This picture of a harder surface covered by a low density dust layer is in agreement with the theory of Gold (1964) although the suggestion of Hapke (1964a) of surface bonding of such dust particles does not agree with the model of a transparent floating dust layer transparent with respect to solar radiation.

The "fairy castle" structure suggested by Hapke, being a complex vertical and horizontal open structure, built up by the bonding of vacuum clean surfaces on contact, is one of the possible surfaces which has a reflection direction diagram similar to that observed for the lunar surface.

In an experiment, involving high angular resolution Oetking (1966), has shown that the fairy castle is not the

only type that will produce the required phase curve. His results show that a number of different chemical powders will produce a similar curve, the restriction lying in the size of the individual particles. While the sharp peaking in the forward direction is repeated for most of the substances measured it is in the case of particle sizes of the order of 10 microns or less that the curve is followed at angles greater than 20°. An exception to this is the basic rock 'melilitite', which when presented as a cut slab followed the lunar curve reasonably closely. This may be due to the type of cleaning method used for the rock prior to measurement. The material which most closely follows the lunar curve is the volcanic substance known as 'Pele's hair'. Because of the fine structure of this substance, the 'fairy castle' structure may still be applicable. Observations which have a possibility of giving information as to the composition as well as the physical structure of the lunar surface are measurements of the spectral reflectivity.

A study of the reflection spectra of possible lunar materials in the infrared region has been made by Lyon (1964). Figure 7.1 from Lyons paper shows the reflection spectra of tektite and meteoric materials over

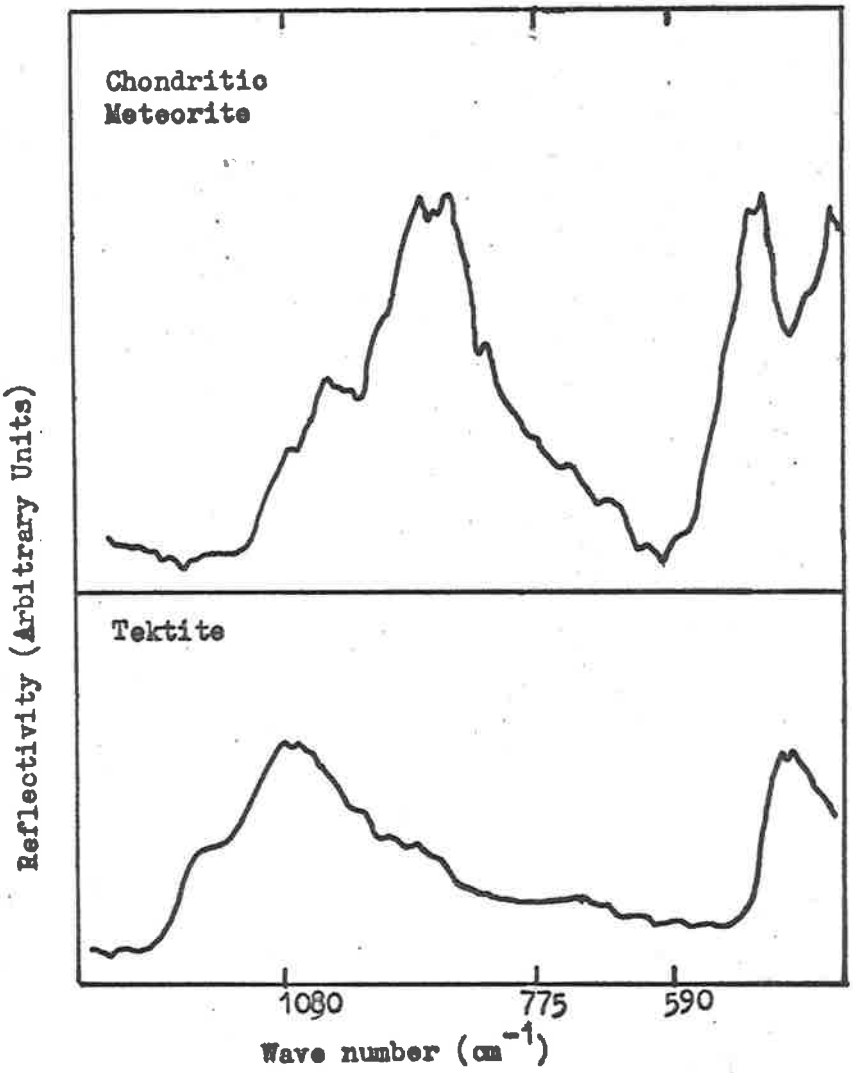

Figure 7.1 Infra-red reflection spectra of Tektite and Meteoric material. (After Howard (1964)).

the range 7 to 25 microns. It is obvious that measurements of the lunar spectrum with this resolution would provide useful information as to the composition. Measurements of the infrared spectrum of the moon, made in the 1 to 3 micron region by Wattson and Danielson (1965), however, show that there is a feature in the spectrum which may be assumed to be due to the thermal emission of the surface. This feature shows an anomolous rise at about 2.5 microns which while perhaps being introduced by the measurement method, as suggested by Wattson and Danielson, could also be due to the layer as mentioned by Gehrels above. Because of such uncertainties the infrared spectra are perhaps suspect.

Measurements made in the visible region of the spectrum by Stair and Johnston (1953) and Coyne (1963) show no indication of structure in the reflection spectrum other than a slow increase of reflectivity with wavelength tending to make the moon appear redder than the illuminating body. Stair and Johnston make this observation by direct ratios while Coyne takes magnitude differences at different colours.

In the near ultraviolet portion of the reflectivity spectrum observed by Stair and Johnston, a feature appears at about 3800Å which is a departure from the steadily falling value of reflectivity with decreasing wavelength for the

visible region. Stair and Johnston suggest that this may be associated with a small iron content. To the short wavelength side of 3600Å, Stair and Johnstons results as shown in Figure 7.2, display a sharp drop in the value of reflectivity, suggesting that the measurement in the ultraviolet may contain information as to the composition as well as the structure.

7.2 Measured Values of Ultraviolet Radiation from the Moon

For the reason stated in Section 7.1, the measurement of the spectral energy distribution of the radiation reflected from the lunar surface was an important part of the experiments performed. The wavelength range covered by the Hartley absorption bands of ozone is also that region where the results of Stair and Johnston indicate a sharp drop in reflectivity of the surface, thus no other photometers were required for this measurement.

As shown in Figures 5.8 and 5.9, the values of the flux incident on the sensors became almost constant at the top of each flight and the value obtained for absolute

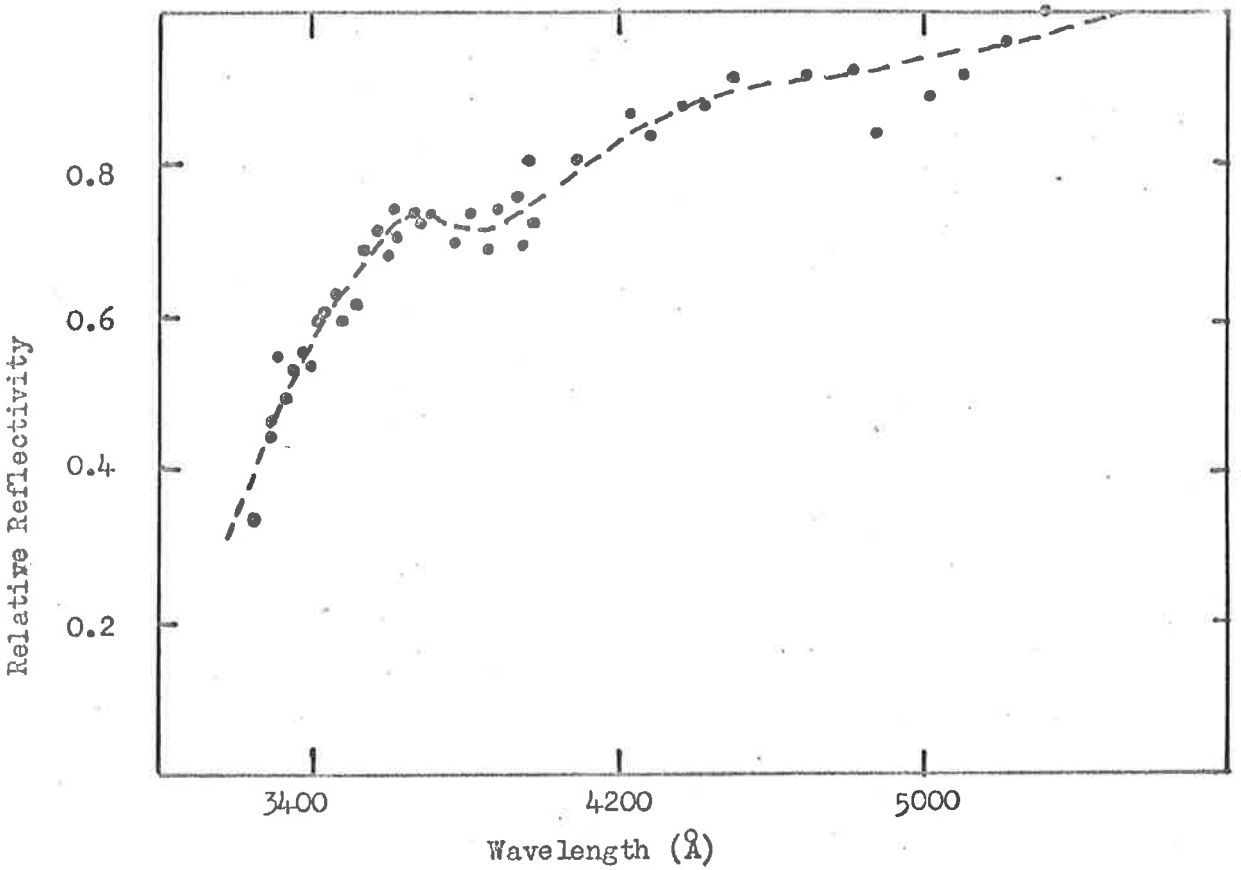

Figure 7.2 Relative spectral reflectivity of the moon after Stair and Johnston.

flux could be assumed constant within the range of calibration of the sensors. The measured values are shown in Table 7.1.

From the slopes of the ozone distribution curves in Figure 6.3, the scale height of the distribution was determined at a value of 7.7 kilometers, the same value for each curve. Taking the value of number density at height of measurement of incident flux to be 2.5×10^9 and 1.0×10^9 molecules per cm^3 for HADs 305 and 312 respectively, the residual numbers of ozone molecules along a column along the line of sight to the top of the atmosphere are 4.92×10^{15} and 1.67×10^{15} molecules per cm^2 column. The correction to the flux produced by the absorption due to these particles is negligible with respect to the error in absolute calibration so that the values of flux determined will be as shown in Table 7.1. From the results of HADs 305 and 312 the mean values of flux observed was obtained after correction for phase angle to the full moon value, the correction values being 1.25 and 1.1 respectively. The values of the lunar flux so obtained together with the result of Heddle (1962) are listed in Table 7.2.

TABLE 7.1

Lunar flux as measured uncorrected for phase
(ergsx10^{-6} cm^{-2} sec^{-1} $Å^{-1}$)

HAD	2400Å	2500Å	2700Å	2900Å
305	1.8		5.8	12.2
312	1.0	1.7	11.0	22.0

TABLE 7.2

Mean Lunar flux corrected for lunar phase
(ergsx10^{-6} cm^{-2} sec^{-1} $Å^{-1}$)

Wavelength	Flux	
2200	.61	Heddle (1963)
2400	1.66	Present work
2500	1.91	" "
2700	10.20	" "
2900	19.6	" "

7.3 Reduction of Flux Measurements to give Lunar Albedo

A quantity frequently employed in a statement relating to the reflection of radiation from a surface is the albedo of the surface. In the case of an illuminated sphere a special form, termed the Bond albedo, is used.

The Bond albedo is defined (see Allen 1963 p144) as the ratio of total light reflected from a sphere to the total light incident upon it.

i.e. A = Bond albedo = pq

where p is the Geometric albedo, and is the ratio of reflected intensity from the sphere at zero phase angle to the intensity from a perfectly diffusing disc in the same position and having the same apparent size as the sphere observed, and q is the integrated phase effect of the sphere.

Let the sphere be a planet or satellite, at a distance d from the sun, a distance R from the earth, having a radius r, all in Astronomical Units. If this planet is illuminated by the sun, of magnitude $m_\odot$, at an

angle α to the direction of observation, and is observed to have a magnitude m_o, then, from Allen (1963, p144),

$$\log p + \log \phi(\alpha) = 0.4\ (m_o - m_o) + 2 \log\left(\frac{dR}{r}\right)$$

where $\phi(\alpha)$ is the phase factor, dependent upon the surface illuminated.

From the definition of magnitude - flux relation, (Allen, 1963, p192)

$$m = \text{constant} - 2.5 \log (\text{Intensity observed})$$

and referring to the moon observed at full moon where $\alpha = 0^\circ$ and $\phi(0) = 1$ (See Allen, 1963, p146)

$$\log p = 0.4\ (-2.5 \log \text{Intensity}_{sun} + 2.5 \log \text{Intensity}_{moon}) + 2 \log\left(\frac{dR}{r}\right)$$

i.e. $$p = \frac{I_{moon}}{I_{sun}} \left(\frac{dR}{r}\right)^2$$

where I is in units of energy received per unit area.

With $d = 1$ A.U.

$$R = \frac{2.4 \times 10^5}{9.3 \times 10^7} \text{ A.U.}$$

$$r = \frac{\text{Angular radius} \times 2.4 \times 10^5}{9.3 \times 10^7} \text{ A.U.}$$

i.e. $$\frac{dR}{r} = \frac{1}{\text{angular radius}}$$

The angular radius of the moon is 15'32".6 (Allen, 1963, p149) which may be expressed as 0.0045 radians. From these values

$$p = 4.97 \times 10^4 \frac{I_{moon}}{I_{sun}} .$$

By definition (Allen 1963, p144),

$$q = 2\int_0^{\pi} \phi(\alpha) \sin \alpha \, d\alpha$$

and for the moon, has a value 0.585 (Harris 1961, p309).

i.e. for the moon

$$A = 2.9 \times 10^4 \frac{I_{moon}}{I_{sun}} ,$$

and monochromatic albedos are

$$A(\lambda) = 2.9 \times 10^4 \frac{I(\lambda)_{moon}}{I(\lambda)_{sun}}$$

where $I(\lambda)$ is the monochromatic intensity in energy per unit area for unit wavelength interval, and $A(\lambda)$ is the total light, within a unit wave interval, reflected from a spherical, in this case the lunar, surface.

7.4 The Wavelength Dependence of Lunar Albedo

To extend the range of results for the lunar monochromatic albedo beyond that of the present results, values of the lunar flux were taken from Heddle (1963) for the value at 2200Å, and from Stair and Johnston (1953) for the results to the long wavelength side of 3200Å. Values of the solar flux above the atmosphere were taken from Gast (1965). These extracted results, together with the values obtained in the present investigation, were employed in the term for $A(\lambda)$, in Section 7.3 and the values obtained are shown in Figure 7.3. The curve for the lunar albedo, shows structure in two regions. These

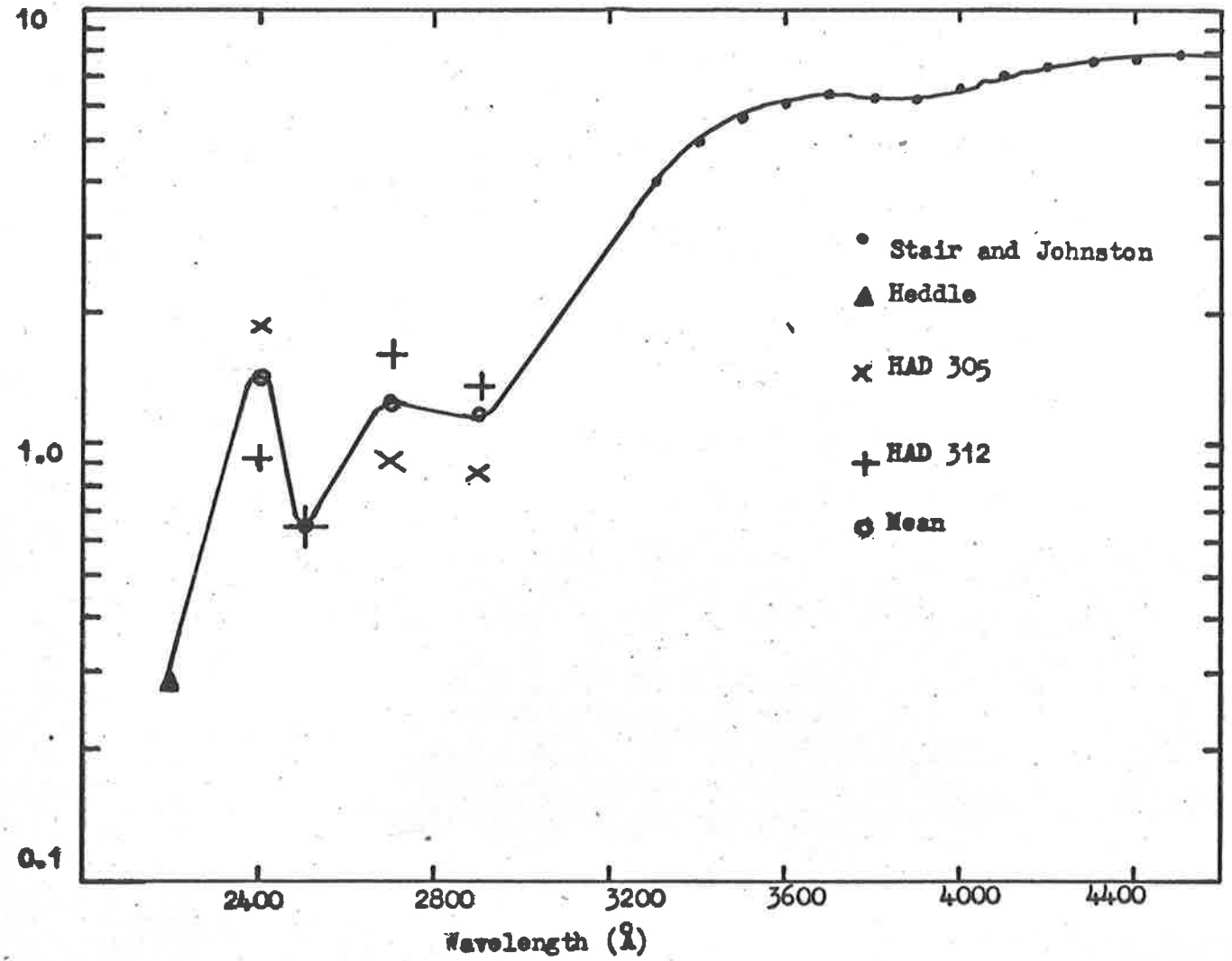

Figure 7.3 The lunar albedo as a function of wavelength

are a dip in the value near 3800Å and a peak near 2400Å. The overall effect is a steep drop in reflectivity to the short wavelength side of 3500Å.

7.5 Comparison with Laboratory Measurements of Possible Surface Types and Theoretical Results

In a review of the photometric properties of the lunar = surface and its possible structure, Hapke (1964b) considers the evidence of the observed phase relation of the reflected light and the variation of polarisation with phase angle. The response of the surface in respect to these quantities with phase angle is shown in Figures 7.4 and 7.5 from Hapke. To explain the high back scatter peak, Hapke proposes a porous surface layer with interconnected pores. The effect of this surface is that the incident light will penetrate the surface freely and illuminate the base structure on which the surface formation is supported. Light will be reflected directly back from the base structure without secondary reflection but light reflected in any other direction will be blocked by the porous structure and through many reflections be absorbed. The surface of the porous structure must not

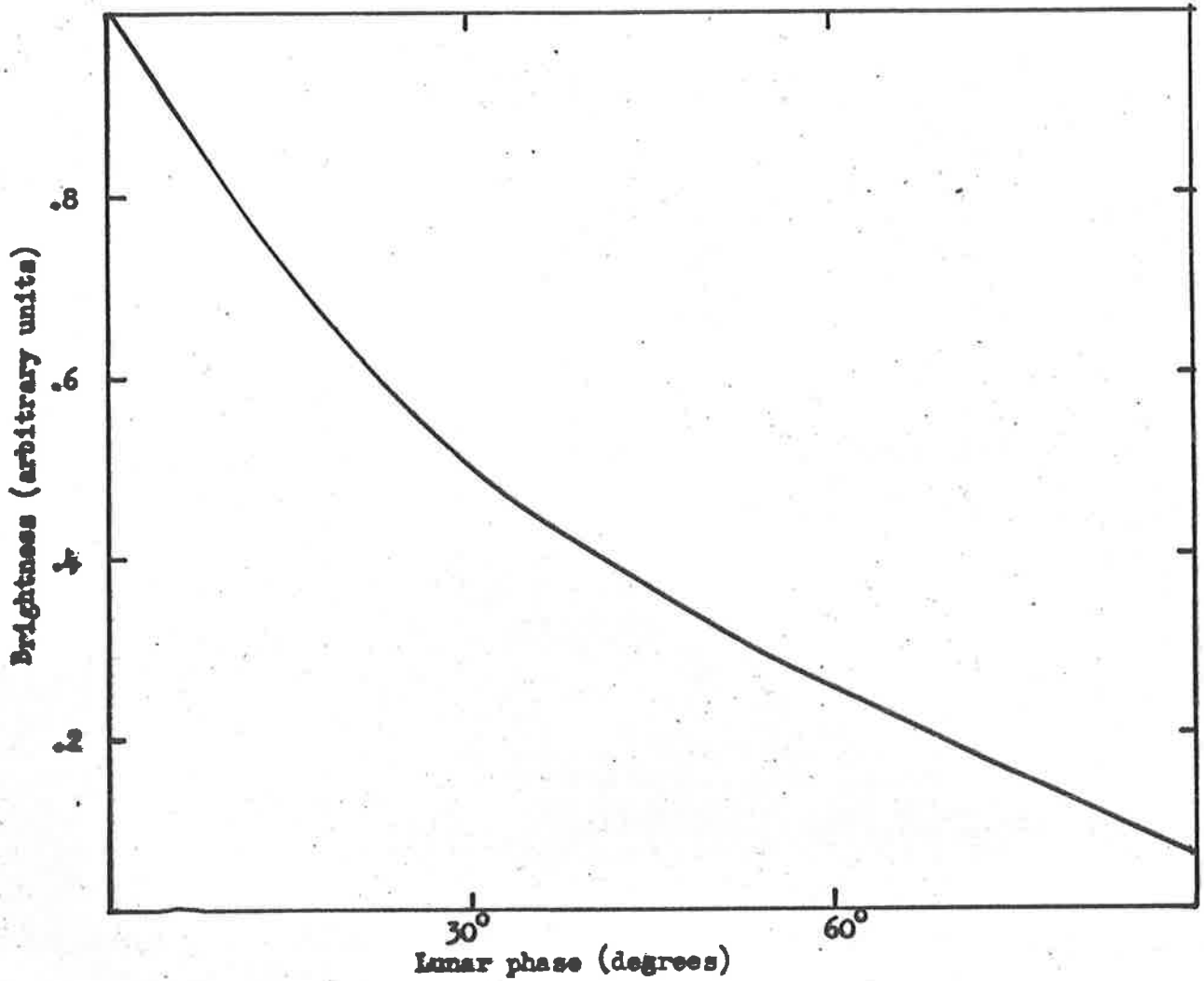

Figure 7.4 Variation of lunar brightness with phase (after Hapke, 1964).

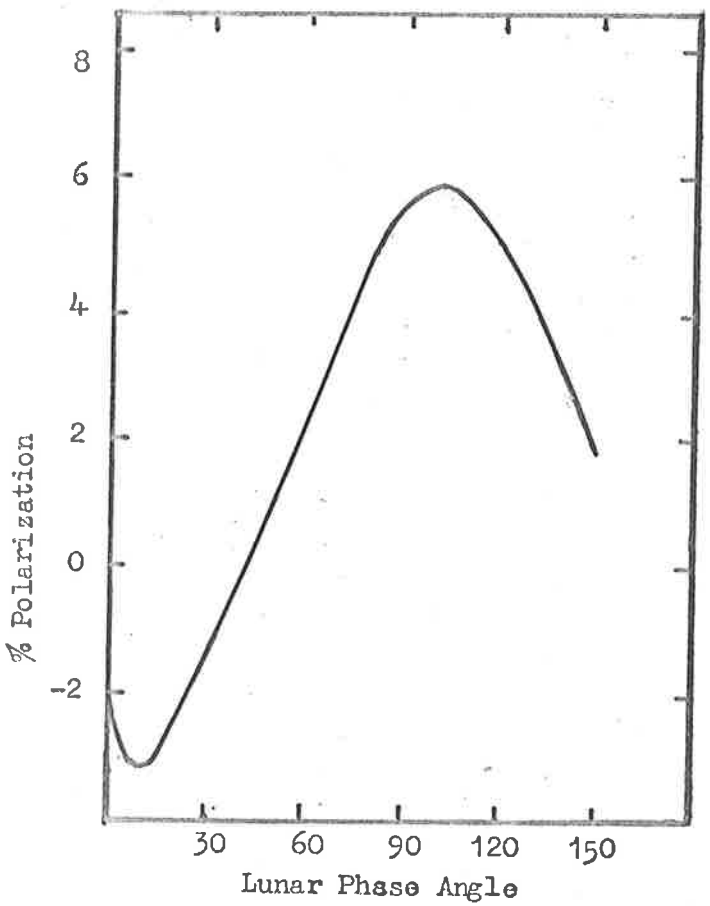

Figure 7.5 Polarization of the Lunar surface with phase angle after Hapke 1964

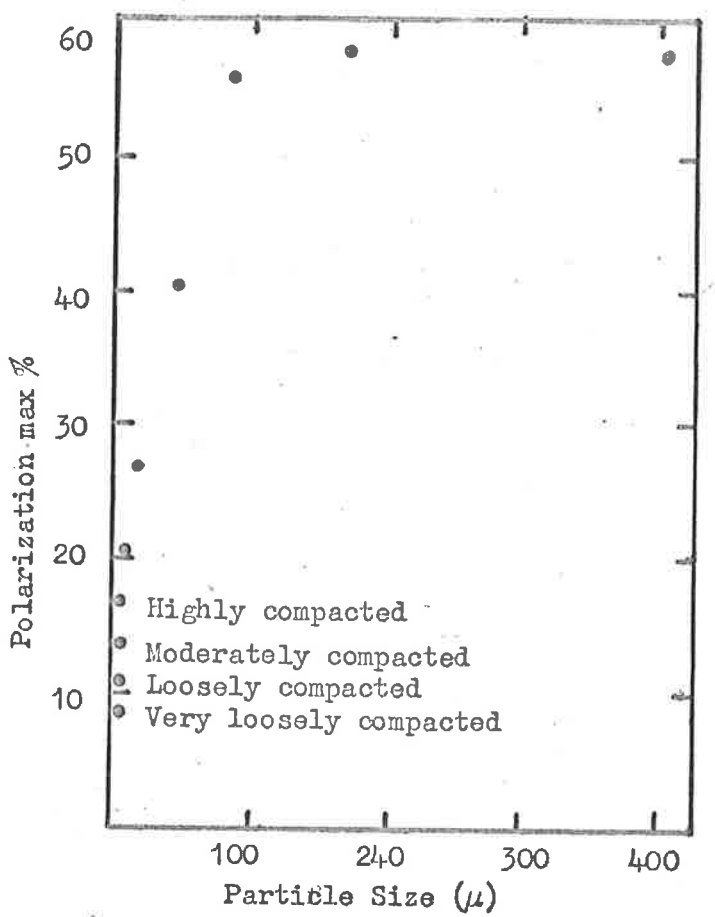

Figure 7.6 Polarisation as a function of particle size after Hapke 1964.

be strongly reflecting nor can the material be translucent as this would tend to broaden out the back scatter profile. A surface that would fit the observed back scatter function is one composed of piled large dark rock fragments but such a surface is rejected by two other pieces of evidence. The first of these is that radar results, Evans (1962) and recent surface photography by soft landing vehicles, (Bastin, 1966) indicate that the general roughness of the surface is of the order of centimetres or less. A second cause for rejection of the piled rock model is the polarisation of the reflected light observed. Such a surface would strongly polarise the reflected radiation which, by reference to Figure 7.5, is not the case for the moon's surface.

A method of obtaining the low polarisation observed is the combination of translucent material with low value of maximum polarisation with dark material with low maximum polarisation properties. Such a mixture will not, however, produce the observed back scatter peak. A form of surface that will produce the polarisation observed without losing the back scatter characteristic needed is a roughened surface. The variation of the value of maximum polarisation as a function of particle size is shown in Figure 7.6 taken from Hapke (1964b). It is obvious from

this figure that, whatever the state of compaction of the surface particles, the size of the particles that produce the same value of maximum polarisation as the lunar surface is of the order of a micron.

From the evidence of polarisation the maximum value of particle size is about a micron. Berg (1964), in a study of the size of rock particles resulting from the impact of high velocity projectiles on rock surfaces, finds that the typical size of such particles is of the order of 10^{-1} microns. As there is nothing in the work of Hapke to require a restriction of the smallness except that the surface roughness be greater than the wavelength of the incident radiation observed in reflection, the size of the particles may be of this latter dimension.

In a study of the effect of surface structure and size, O'Brien (1967) has expanded a theory developed by Davies (1954) and Porteus (1963), relating to the reflection of light from rough surfaces. This theory examines the coherence of scattered electromagnetic radiation from a surface consisting of point scatterers, having a standard deviation in height above a plane surface of σ and a separation in the horizontal direction of a, (of the order of 50,000Å, this being the distance apart where coherence

of the incident radiation may be assumed). The effect of this structure, which may be treated as the mirror image of Hapke's surface for normal incidence, i.e. full moon conditions, is dependent upon the reflectivity of the material and the magnitude of the term σ, and the wavelength of the radiation.

The expression obtained by O'Brien for the reflectivity of such a surface is

$$R = \frac{r^2}{\lambda^2} \exp\left(-\frac{16\pi^2\sigma^2}{\lambda^2}\right)$$

where R = the observed reflectivity

and r = the reflectivity of the material comprising the surface.

From this relation the value of r may be obtained in terms of the observed reflectivity, the standard deviation in height, σ, and the wavelength. The reflectivity of the material, r, is given by

$$r = \left(R\lambda^2 \exp\left(\frac{16\pi^2\sigma^2}{\lambda^2}\right)\right)^{\frac{1}{2}}.$$

From the expression for the Bond albedo, given in Section 7.3, it may be seen that the albedo is proportional to the reflectivity at normal incidence, i.e. we may assume that R is proportional to the measured values of A presented in Figure 7.3.

Using the values of A, the values of r were obtained as a function of λ for a number of values of σ. The results of these calculations are presented in Figure 7.7. Also shown in Figure 7.7 are the results of laboratory measurements of two substances which show characteristics similar to those exhibited by r. These are Pink Acid Tuff and Tektite. Because of the unknown value of the proportionality constants, the values presented for r are only relative and as such are presented in a logarithmic plot which will show any similarity of spectral response.

The chemical composition of the two laboratory samples is

Pink Acid Tuff (Approximately)	SiO_2	- 48%
	Al_2O_3	- 18%
	Fe_2O_3	- 3%
	FeO	- 6%
	MgO	- 7.5%

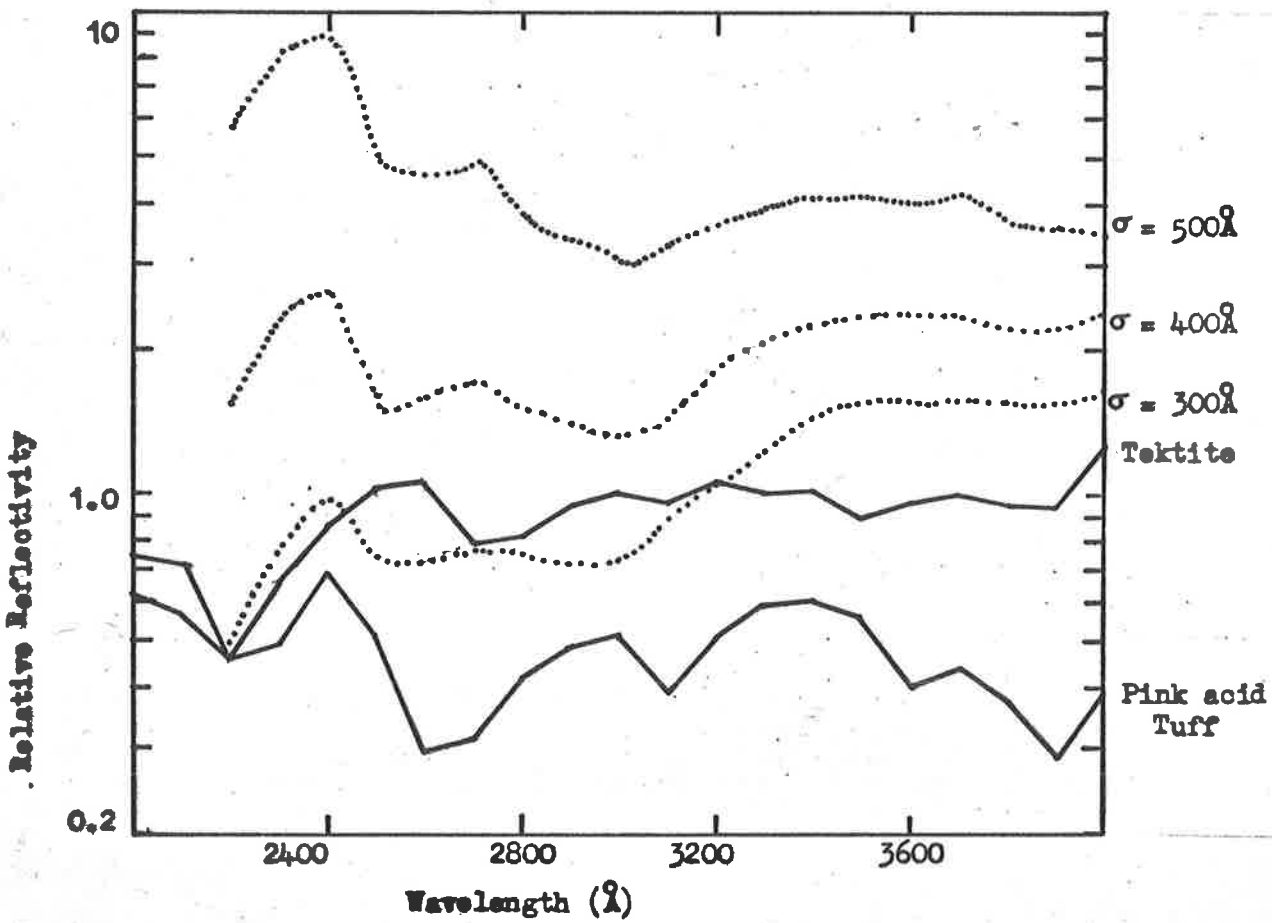

Figure 7.7 Reflectivity of the lunar surface calculated from the relation $r = (R\lambda^2 \exp(\frac{16\pi^2 \sigma^2}{\lambda^2}))^{\frac{1}{2}}$ for values of the roughness parameter and the reflectivity of two surfaces as measured by O'Brien (1967).

	CaO - 11%
	Na_2O - 2.5%
Tektite	SiO_2 - 65%
	Al_2O_3 - 17%
	Fe Oxides - 7.5%
	MgO - 2.5%
	CaO - 4%
	K_2O - 4%

7.6 Conclusions based on Experimental Results

On comparing the results presented in Figure 7.7, the obvious feature is the peak in the reflectivity in the region about 2400Å. The value of σ best suited to the reflectivity of the laboratory specimens seems to lie in the range 300 to 500Å which is between 0.1 and 0.01 times the value of the particle size suggested by the polarisation results. The 2400Å feature appears in surfaces containing a relatively high proportion of SiO_2 while pure metal specimens, as shown by Koller (1952) show no evidence of such structure. The conclusion reached is

that the lunar surface, despite the large craters and boulders observed by close photography, is covered with a fine layer of order micron size, being smooth to a limit of 0.01 - 0.05 microns, the chemical composition being similar to that of the stony meteorites and terrestrial stones rather than being purely metallic after the form of the iron meteorites known to exist.

The suggestion that the particle size is small is borne out by measurements made from the televised photographs obtained from the Surveyor 1 soft landing craft. The limit of resolution of the instruments carried was 0.5 millimetres and the basic particle structure adjacent to the landing pad of the craft was unresolved. Jaffe (1967). Another feature of the photographs was the granulated structure where the surface was broken by the pad, suggesting that the surface structure is not loose but that the basic particles are bonded together by some surface interaction similar to moisture on sand particles.

Because of the difficulty of absolute calibration, it would be preferable to observe the lunar spectrum in the ultraviolet region with a single dispersing instrument rather than the multi photometer method employed in this investigation as this would allow a more direct method of obtaining the spectral dependence of the reflectivity.

CHAPTER 8

AN AUSTRALIAN EARTH SATELLITE PROJECT

8.1 Introduction

In November 1966, a preliminary proposal was made relating to the construction and instrumentation of an earth satellite to be launched by the technical staff associated with the Sparta Programme of the United States Government from the Woomera Rocket Range of the Department of Supply. In January 1967, the task of construction of the satellite was set for the Weapons Research Establishment while the instrumentation was to be shared between Flight Projects Group of W.R.E. and the Department of Physics of the University of Adelaide. The reason for this selection lay in the previous experience of these two organisations in the production of rocket borne sensors which were suitable with little modification, for instrumentation of an earth satellite. The aim of the combined experiments included in the satellite was the determination of atmospheric densities by repeated measurement of absorption of solar radiation by the earths atmosphere. A secondary purpose was the measurement of the solar flux at the wavelength intervals

employed in the first experiments.

8.2 Launch Vehicle and Satellite Configuration

The launch vehicle to be used was a three stage configuration consisting of

1st Stage — Modified Redstone missile boost motor as used in the first successful United States Satellite launch. This unit has a liquid fuel motor and a burning time of 122 seconds.

2nd Stage — A solid fuel motor with a burning time of 33 seconds which also carried a secondary set of small motors designed to spin up the second stage and velocity package before ignition of the main second stage motor.

3rd Stage — A solid fuel motor with a burning time of 8.6 seconds which provided the final impulse to place the velocity package, consisting of the third stage motor and the satellite, into an orbital trajectory.

The satellite, which made up the greater portion of the velocity package, consisted of a cone of base diameter 30 inches and height of 5 ft 2 inches. The fuel compartment of the third stage motor extended as a hemispherical section into the satellite cone to a maximum depth of 11 inches. Because of the high heat levels generated in the motor and the mechanical connection between the motor compartment and the fuel tank, a heat shield took up the lower portion of the cone volume, protecting the instrumentation from heat generated in the motor compartment. The structure of the cone consisted of flat ring rib plates and vertical stringers covered with plate aluminium skin. The rear support for the vehicle was the mating strong ring for the third stage while the forward support was the forward sensor block. The shape of the velocity package is shown in Figure 8.1 and the launch vehicle configuration in Figure 8.2.

8.3 Radiation Detection Instrumentation

The purpose of the satellite instrumentation was the investigation of the region of interaction of solar radiation with the atmosphere of the earth. The experi-

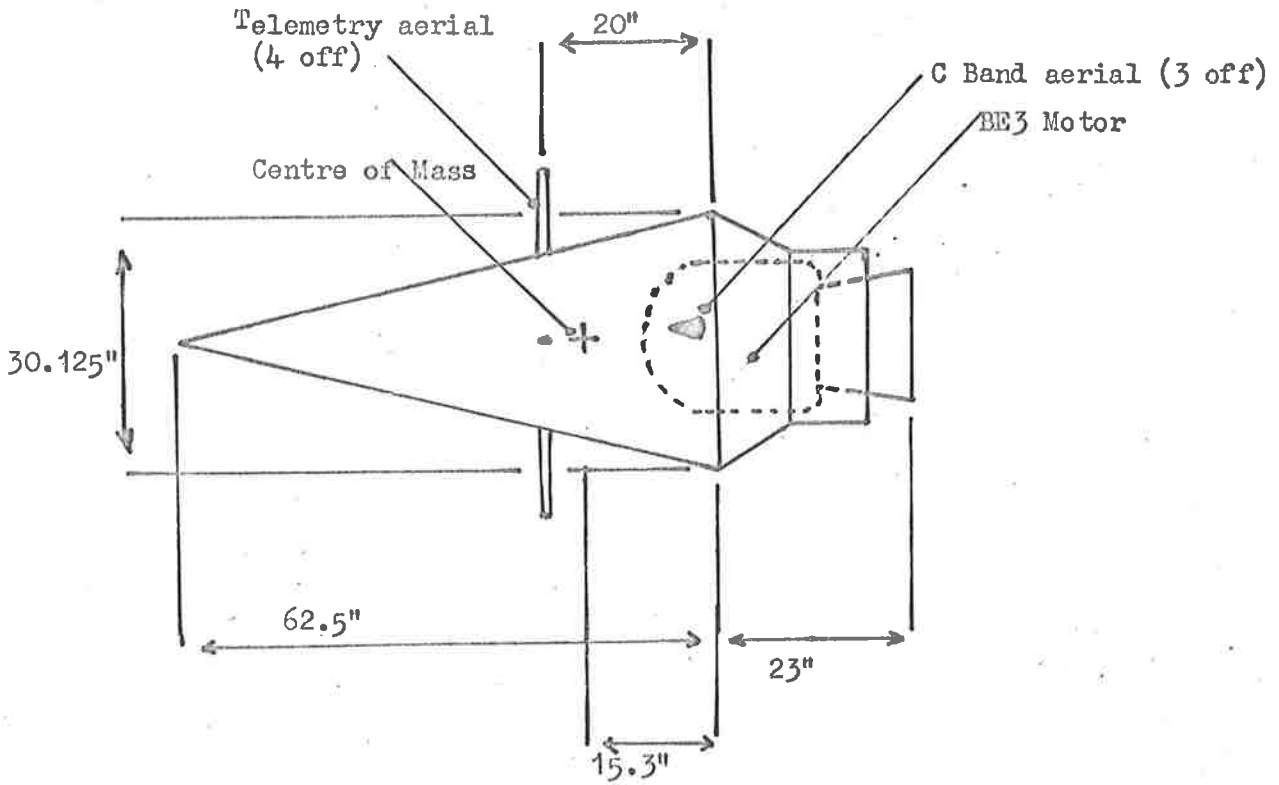

Figure 8.1 Configuration of the orbital velocity package.

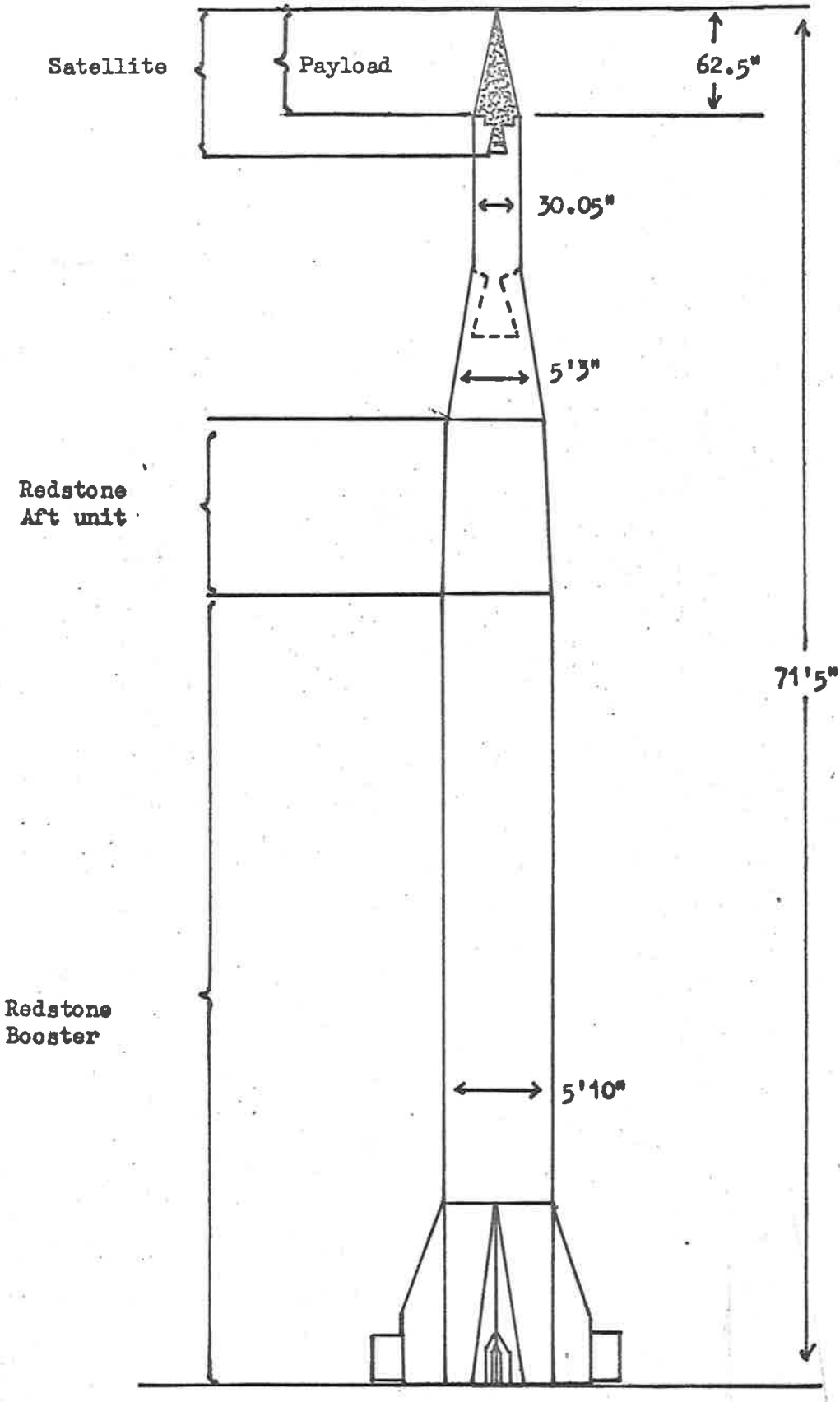

Figure 8.2 Launch vehicle configuration.

ments were:

1. By measurement of the time differential absorption of radiation from the sun, in the wavelength region 1050Å to 1660Å during satellite sunset and sunrise, combined with knowledge of the satellite orbit, to determine the density of molecular oxygen up to altitudes of 250-300 kilometers.

2. By similar measurements in the region of 2400Å, to measure the density of ozone over as wide a height range as possible.

3. By similar measurements in the 8Å region to measure the total atmospheric density over as wide a range as possible.

4. To monitor the intensity of the suns radiation over the same wavelength regions during day passes.

5. To measure the resonantly scattered radiation from atomic hydrogen at the wavelength of Lyman α at a number of different positions in the earths shadow above and below the orbit altitude.

6. To measure the scattered radiation from the sunlit atmosphere over the wavelength range about 2400Å to obtain a measure of high altitude ozone.

The instrumentation to make these measurements consisted of

2 ion chambers filled with Nitric Oxide having Lithium Flouride windows being sensitive to a wavelength range 1050 - 1340Å.

2 ion chambers, filled with xylene and having saphire windows being sensitive to a wavelength range 1425 - 1480Å.

2 ion chambers filled with triethylamine and having quartz windows being sensitive to a wavelength range of 1550 - 1660Å.

1 photometer consisting of an interference filter in front of a quartz window photomultiplier operated in photo-diode mode sensitive to a wavelength of 2400Å with a half width at half maximum of 50Å.

1 X-ray detector with mica window and neon argon filling sensitive to a narrow band about 8Å.

1 gas gain ion chamber with nitric oxide filling and lithium flouride window as a detector for a telescope consisting of a 1" lithium flouride lens operating at

f4.5 stopped down to give a field 2° full width at half maximum.

The sensors were mounted in two separate groups. The first group was mounted at the apex of the cone, the sensors being covered with a removable cover until the completion of the injection phase of the launch to protect them from atmospheric heating up to this stage. This group consisted of one each of the ion chamber types and the 2500Å photometer. The view of these sensors was along the long axis of the cone, the field of view of the ion chambers being 40° half angle while the 2400Å photometer had a mean half angle about 15° the actual field being asymetrical.

The second group of sensors were mounted near the surface of the cone, 2 ft 6 inches from the apex, such that their field of view was normal to the long axis of the cone. This group consisted of one of each type of ion chamber, the Lyman α telescope and the X-ray detector. A similar removable cover was in place over these detectors during the preinjection phases of the launch.

The block holding the forward sensors was an

integral part of the cone structure being the apex block of the cone. A rear retaining plate made possible the positioning of the ion chambers while the 2400Å detector was moulded into the block.

The side viewing sensors were mounted in a removable module which also contained the electronic units associated with the sensors in that section.

8.4 Electronic Units for the Experimental Packages

The currents produced by the ion chambers, the 2400Å photometer and the Lyman α telescope were all fed to logarithmic amplifiers. Those associated with the NO- LiF chambers, and the 2400Å photometer covered the range from 0 to 5 volts for input currents from 10^{-10} to 10^{-6} amperes while those associated with the other ion chambers and the Lyman α telescope covered the same voltage range for input currents from 10^{-12} to 10^{-8} amperes. The count pulses from the X-ray detector were passed to a pulse shaper which then fed a digital to analogue converter, making the full 5 volt excursion for a total count of 256 counts. The unit gain potential for the ion chambers

was supplied from a battery and entered the sensor packages from an external source. The high tension required for the gas gain operation of the telescope ion chamber was supplied at 1000 volts from a corona tube regulated supply from a dc-dc converter. A similar unit supplied the voltage at 500 volts for the X-ray detector while the 100 volts for the photometer operation was taken from a divider chain across the 500 volt supply. Another unit was a timer of 30 second period which provided a pulse that discharged a capacitor charged to 1.5 volts through a resistor connected in parallel to the amplifier input. This current was controlled by relay switches and supplied a 60m second calibration pulse to each amplifier. All electronic units were potted in Dow Corning 850 RTV Silastic the leakage resistance of this material being just suitable for the current ranges involved at the amplifier inputs. The HT supplies for the telescope chamber and the X-ray sensor were carried to their respective units by coaxial cable links. These cable links were potted at each end to avoid the possibility of gas leaking from the cable under vacuum environment and accumulating to sufficient pressure to maintain a corona discharge. All amplifiers associated with the side facing block and the HT supplies were mounted in that module

while the amplifiers for the forward looking set were mounted on a bracket suspended internally from the forward block for this purpose. The 100 volt line was carried from the side to forward block by a coaxial cable included in the internal looming. All voltages for operation of the units were also carried in these looms.

8.5 Solar Aspect and Attitude Sensors

As one of the purposes of the experiments was the measurement of the solar flux levels and as the detectors had known angular responses it was necessary to know the angle between the line of sight of the detector and the position vector of the sun. This was to be measured by solar aspect sensors, consisting of two photo transistors mounted side by side behind teflon diffusers. The shapes of these diffusers was such that the angle response of each transistor was different and the angle between the sun vector and the line of sight of the sensors could be determined by taking the ratio of the outputs and comparing these with a preflight calibration. Such an aspect sensor was in each experiment package. To assist in the determination of the actual attitude of the

space craft in orbit, three mutually perpendicular flux-gate magnetometers were included in the payload, mounted diametrically opposite the side facing experiment package. Due to weight limitations two of these had to be removed from the satellite prior to launch leaving one magnetometer with its axis parallel to the long axis of the cone.

8.6 Other Instrumentation Carried

An important part of the environment for both the sensors and the electronic units was the temperature existing inside the satellite. Sensors to provide this information were supplied and mounted by the Flight Projects Groups of Weapons Research Establishment. These consisted of thermistors calibrated so that the voltages across them fitted the range of the telemetry system. They were mounted on the forward experiment block, on the forward amplifier mount, on the battery package, on the telemetry unit and at five positions on the skin of the cone. A clock, designed and constructed by W.R.E., providing a digital read-out of sufficient range to cover the expected life time of the satellite, was also mounted

with the telemetry system. The telemetry unit was purchased commercially and transmitted through four half dipole aerials mounted at 90° intervals about a plane normal to the long axis of the cone. The signal was on a 136.35 Mc/s carrier as a single frequency modulated subcarrier which was modulated by the voltages appearing on a 16 x 8 array which was sampled twice a second giving the system a sample rate of 256 samples per second. The distribution of telemetry time among the information transmitted is as set out below.

Function	Rad. Expt.	Temp expt.	Attitude	HK	Clock	Sync.
% time	50	10	27	9	1	3

where HK refers to measurements of voltage levels and Sync. refers to bit identification of the matrix array.

The voltages necessary for the operation of the instrumentation and telemetry were supplied from a bank of Yardney silver-zinc cells of varying amp-hour capacity connected in series to supply the voltage lines at the required current levels. The voltage levels supplied were 12.2, 9.15, 6.1, -4.6 and -7.7 volts referred to

the satellite structure. As this type of cell depends upon a moist electrolyte, the battery pack was enclosed in a pressure vessel. An auxiliary battery in the form of a dry cell was mounted externally on the exterior of the pressure vessel to supply the unit gain voltage for the ion chambers, the level being 45 volts.

A requirement of Range Safety was the inclusion of a tracking transponder in the cone. This system receives a signal from a radar transmitter, converts the frequency and retransmits giving positive proof of radar lock on the vehicle. If the signal is lost a 'vehicle destruct' signal was to be transmitted as the path of the vehicle was then unknown. The unit was a C band transponder and separate batteries were carried to activate it, the entire system being mounted to the rear of the forward experimental package.

The positioning of the experimental packages and other units is shown in Figure 8.3.

As well as electrical systems, the cone contained a mechanical structure the purpose of which was to amplify the instability of the rotation mode about the long axis of the cone, imparted during the launch phase and bring about a rapid conversion of position of the axis of

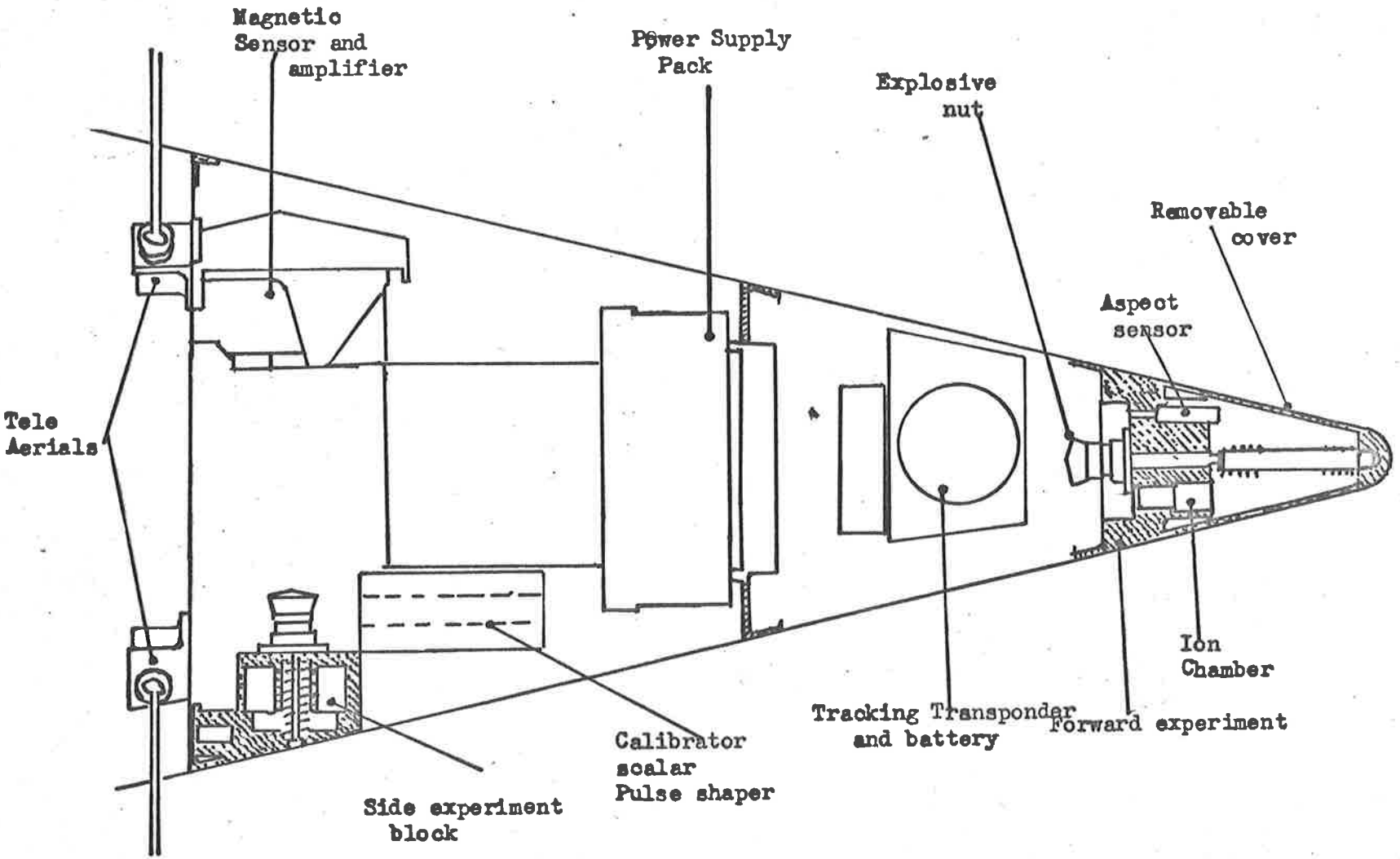

Figure 8.3 Layout of instrumentation in the WRESAT Satellite.

rotation to that of maximum moment of inertia. This was designed to be normal to the long axis and normal to the line of sight of the side viewing experiments. This consisted of a tube which followed the inside of the cone in a plane containing the long axis and normal to the line of sight of the side viewing package. This tube was partially filled with silicon oil, the oil being free to move under the forces imposed by the motion of the cone.

8.7 Temperature Balancing and Weight of the Cone

The planned orbit of the vehicle was such that it would spend some 60% of an orbit period in sunlight. The absorbing of radiation over this period followed by a period in darkness with the loss of absorbed energy by radiation would have produced a variable temperature environment perhaps too severe for the effective operation of the instrumentation which was limited to temperatures from -10°C to 60°C, the levels at these temperatures being beyond the useful range although change of the temperature towards 25°C would allow return to normal operation. Temperatures above this limit permanently changed some

of the instrumentation. The task of maintaining temperature balance was carried out by W.R.E. through Flight Projects Group. The solution lay in painting the bulk of the exterior with a flat black paint while the interior was painted white in all areas which did not endanger electrical systems. By this means energy balance was reached at fairly high temperatures on the skin but, due to the poor radiation property of the interior which was thermally insulated from the skin where possible with teflon spacers, little of this energy was radiated internally by the skin. Regions of the surface close to the experimental packages were covered with Al. tape. This tape was checked for heat tolerance both in air and under vacuum prior to application.

The completed cone containing the instrumentation described in previous sections had a mass distribution as listed below.

Structure Skin, stringers, rib plates etc	32.0 lbs
Thermal Insulation Heat shield, cork, paint etc	9.6

Energy Dissipater Tube, oil, etc	7.4
Experiment Packages	
Forward	2.7
Side	7.9
Magnetometer Head, mount etc	3.1
Telemetry Structure aerials unit etc	8.7
Power Main batteries, regulators etc	18.0
Safety Break-up and Tracking System Transponder, batteries aerials etc	5.5
Covers	1.9
Balance Weights	1.9
Wiring	8.1
	107.4 lbs

8.8 Pre-flight Checks of Instrumentation

Prior to flight all sensors in the experimental packages were calibrated. The method of calibration for each type of sensor was as follows.

ION CHAMBERS

These were calibrated by comparison of signal output as a function of the output of a photomultiplier viewing a calibrated sodium salicylate beam splitter. This had previously been calibrated by comparison with the output of a fully absorbing Nitric Oxide ion chamber, illuminated with Lyman α, assuming the ionization efficiency of Lyman α for Nitric Oxide is known. The response of sodium salicylate as a function of wavelength is also assumed known.

2400Å Photometer

This was calibrated by measurement of voltage output as a function of wavelength when illuminated with the beam from a Bausch and Lomb High Intensity monochromator. The light source used was a high pressure xenon lamp. The spectral energy output of the xenon lamp-monochromator system had been measured previously with a calibrated thermopile. The spectral energy distribution of this combination is shown in Figure 8.4 while the response of the photometer is shown in Figure 8.5. The angular response of this detector is shown in Figure 8.6.

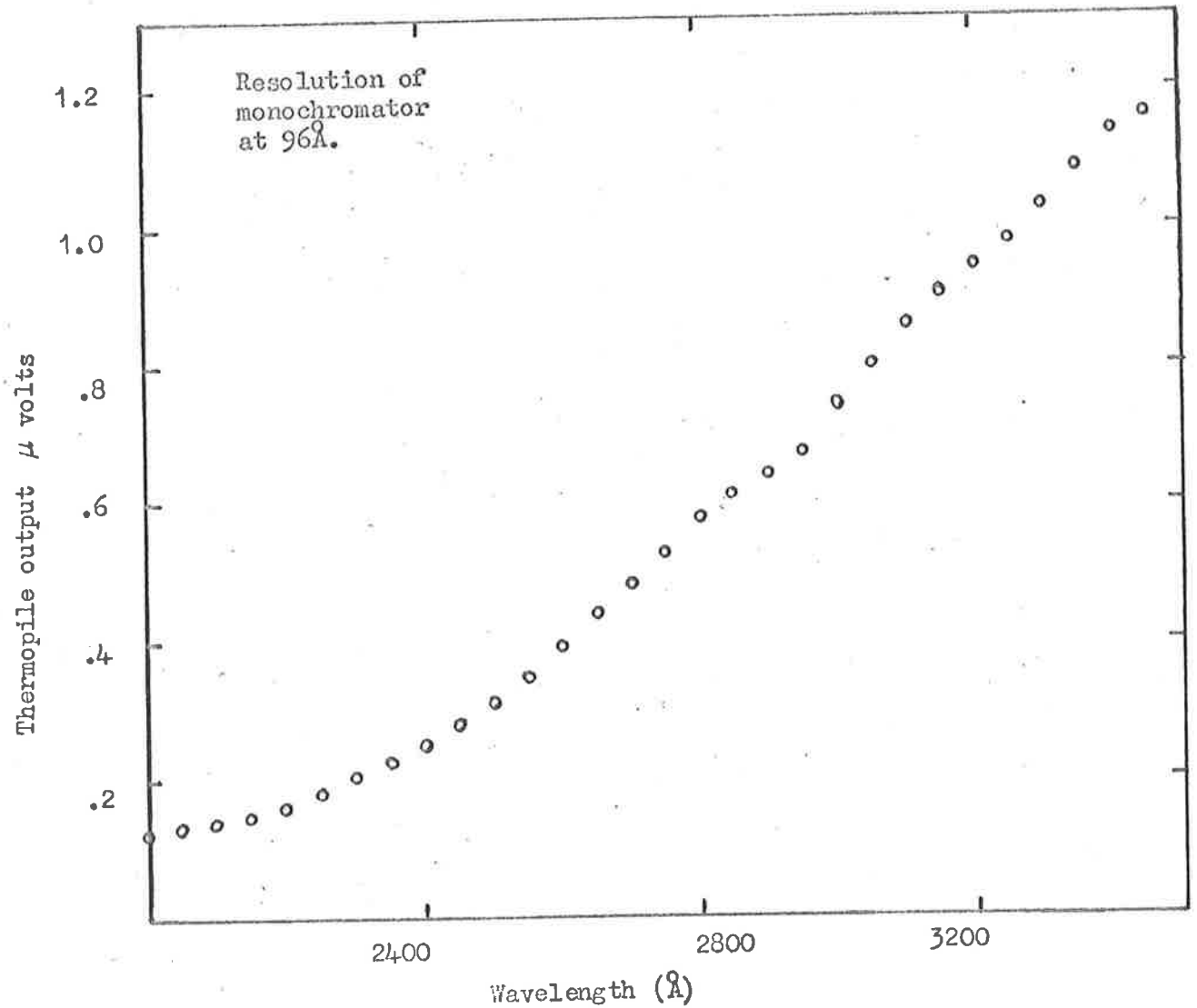

Figure 8.4 Spectral energy distribution of Xenon lamps as measured with a thermopile at 0.064μV/μ Watt cm^{-2}.

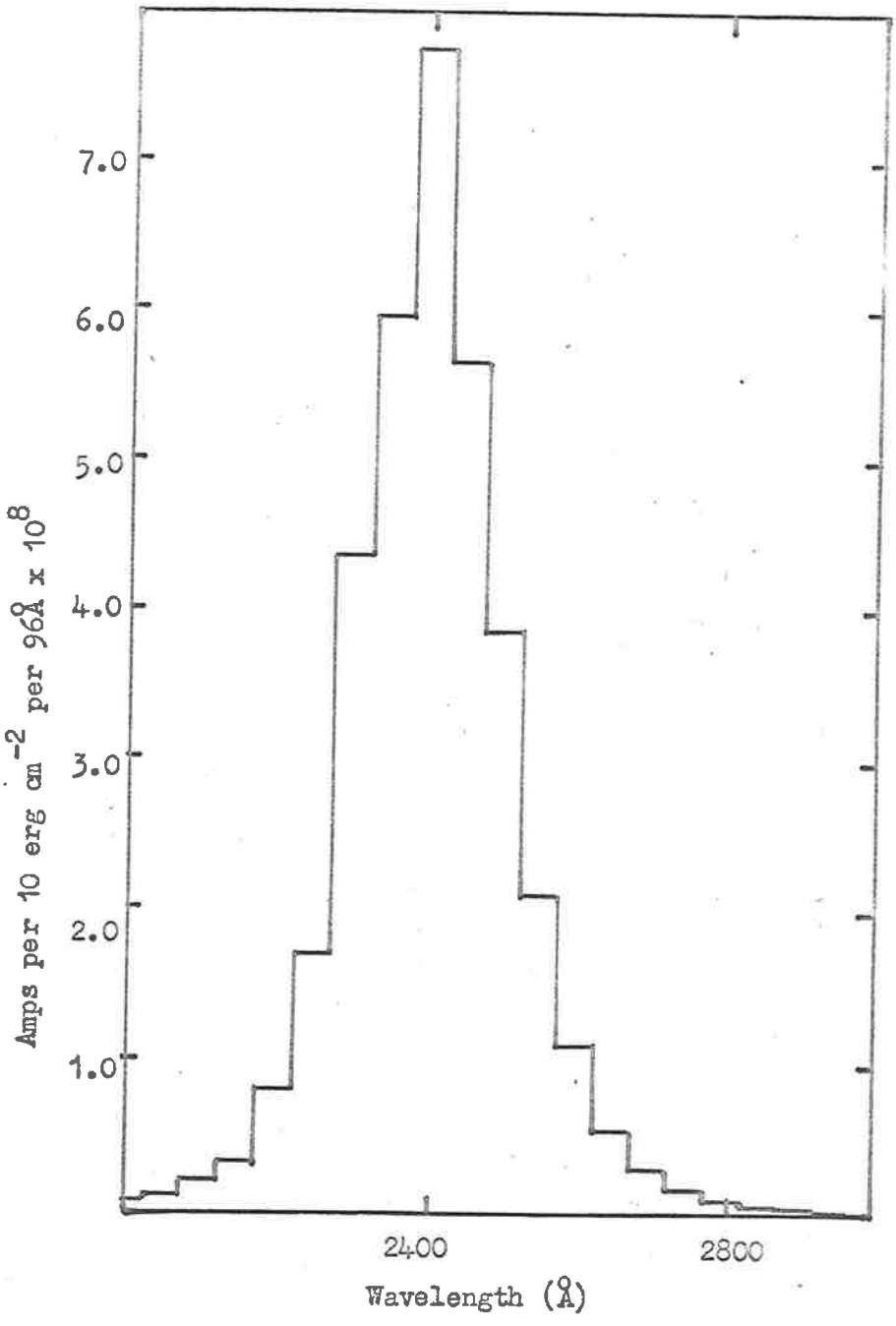

Figure 8.5 Spectral response of 2400Å photometer.

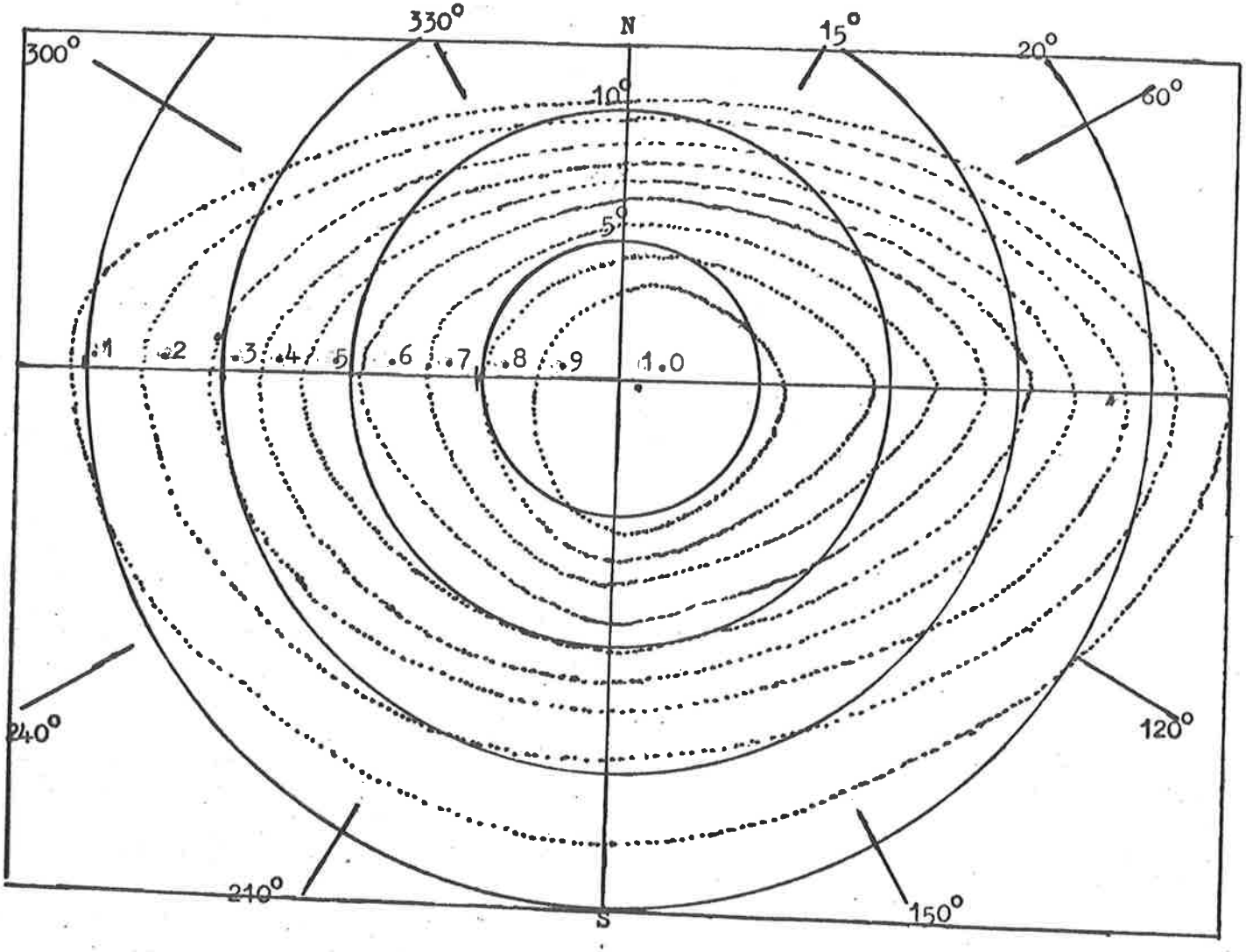

Figure 8.6 Angular response of the 2400Å detector. The line marked NS is parallel to the designed final axis of spin.

X-RAY DETECTOR

The detector, pulse shaper and scalar were calibrated for pulse detection as a function of count rate. It was found that the system saturated for an input rate of 1000 counts per second, for this reason the 256 counts for full scale deflection at two samples per second was chosen to prevent ambiguity in the readout. A lower count would have allowed a possibility of a full count range to have been undetected while a higher number of counts would have caused loss of resolution. The photon efficiency of the detector was measured separately with a standard source, which was also used to determine the angular response of the sensor.

LYMAN α TELESCOPE

A previously calibrated ion chamber was operated at unit gain then at gas gain with a voltage of 500 volts applied. The current per photon was determined from these measurements. The transmission of the lithium flouride lens was then determined and also the angular field of view of the telescope. Knowing the number of photons per second falling on the lens from within a known angular field of view as a function of

the brightness of an extended source, the lens transmission gives the number reaching the chamber. Thus the current from the chamber for a given brightness of an extended source may be determined, and through the amplifier, the voltage out for a given brightness in ergs $cm^{-2} sec^{-1} sterad^{-1}$.

All types of sensor to be included in the payload, though not the flight instruments were taken through a temperature test. This involved the heating of the units to temperatures 250°C, in steps of 50°C, the units being rechecked at each step. All units survived this check, but changes in sensitivity above 150°C set this as the upper limit that could be reached by the equipment at any time during the ascent, injection or orbital phases of the programme.

Solder joints under load were also found to weaken at this temperature. All electronic components to be used in the construction were subjected to this temperature of 150°C and, with the exception of transistors, pin up capacitors and tubular ceramic capacitors, showed no effects in operation. PNP transistors showed a gain change of 2.5% while NPN's showed no gain change. Pin up capacitors emitted some wax and showed some change of

value, a similar change being noticed in tubular ceramic capacitors.

The completed electronic units were subjected to both cold and hot checks. The logarithmic amplifiers showed some change in gain when taken to -75°C but recovered to precalibration levels on returning to room temperature. On being raised to 75°C a drift of 20% in output levels for fixed input current occurred, the amplifier returning to normal on reduction of temperature.

The X-ray detector, on being taken to -65°C, went into continuous discharge but recovered on returning to room temperature. Other units showed some small changes in operation at temperature extremes but returned to normal at room temperature.

After being assembled into the satellite cone, the whole package was placed in a space environment chamber at Adelaide University and subjected to hot and cold cycles extending over a period of four days. The equipment employed in these tests is shown in Figure 8.7. All units survived this test without observable change in operation, the temperature effects being as in the previous tests.

Figure 8.7 Vacuum chamber, hot and cold soak pumps and power supplies during space environment tests.

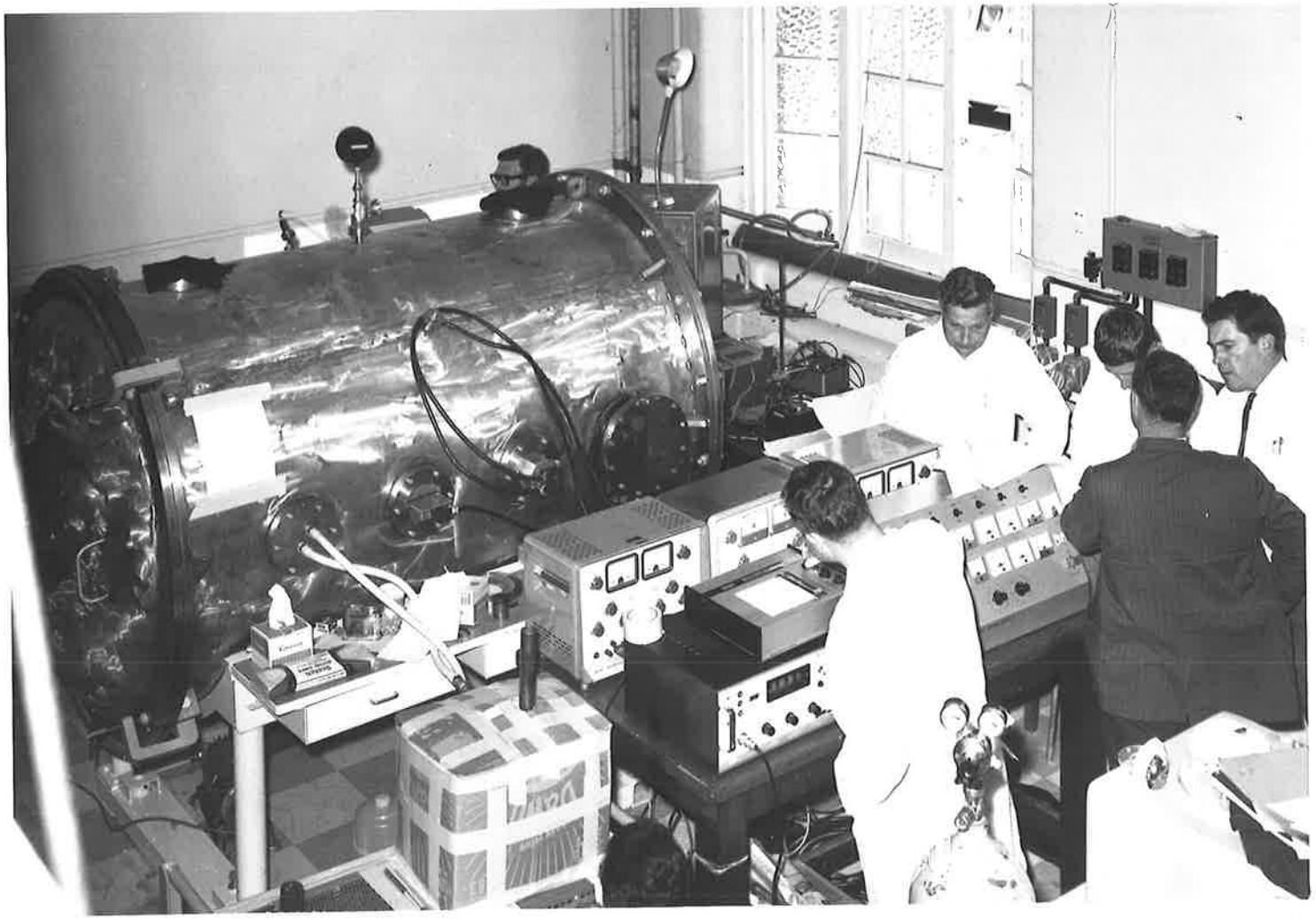

The entire unit was also subjected to vibration and acceleration tests without change in operation of any measureable parameters. Prior to integration with the launch vehicle, the satellite was transported to the Orroral Valley station of the N.A.S.A. Minitrack network to check telemetry compatability with the net.

The form of the completed cone before mating with the third stage motor is shown in Figure 8.8.

8.9 Launch and Operation of the Satellite

The satellite was mated to the launch vehicle during one week prior to the proposed launch date. A mechanical failure of a support unit prevented launch on the first date but this was followed by a successful launch at 1425 hours Central Standard Time on November 29th, 1967. Monitoring spin modulation to the signal received by tracking stations during the first orbit confirmed the conversion of spin about the longitudinal axis to a propellor mode within 35 minutes of launch while receipt of signal by the minitrack station at Carnarvan, West Australia confirmed acquisition of orbit,

Figure 8.8 Satellite cone with inspection panels removed, showing colour treatment for thermal environment control.

and the satellite was given the COSPAR designation 1967-118 A.

The vehicle transmitted telemetry for 54 orbits, the planned life of the power supply and all sensors operated satisfactorily. Preliminary studies of telemetry received indicate that a number of sunrises were obtained in the region of 20° to 25° south latitude and that all sensors saw these events. To date no accurate information is available as to the complete ephemeris of the satellite so that no quantitative results are available.

APPENDIX 1

DYNODE MODULATOR

The circuit for this component is shown in Figure A.1.1. The purpose of this circuit is to provide a square wave of 100 volts, peak to peak, which, applied to the selected dynode of the photomultiplier, will modulate the photomultiplier current in order to take advantage of the low drift characteristic of an A.C. amplifier system.

The basis of the circuit is the saturated core oscillator. The form of operation of this system is as follows.

When the supply volts are applied, one of the two transistors, T1 say, will conduct according to the initial state of unbalance existing. The main impedance in the circuit is in the winding W1 of the transformer so that the collector of T1 will be close to ground. The voltage induced in the coupled winding W3, wound on the same core is such that, when applied to the base of T1, will hold this transistor hard on. This will be the case until the core saturates when the induced voltage will drop to zero. When this occurs the collector current will decrease, because of the decrease in the base-emitter potential. This decrease

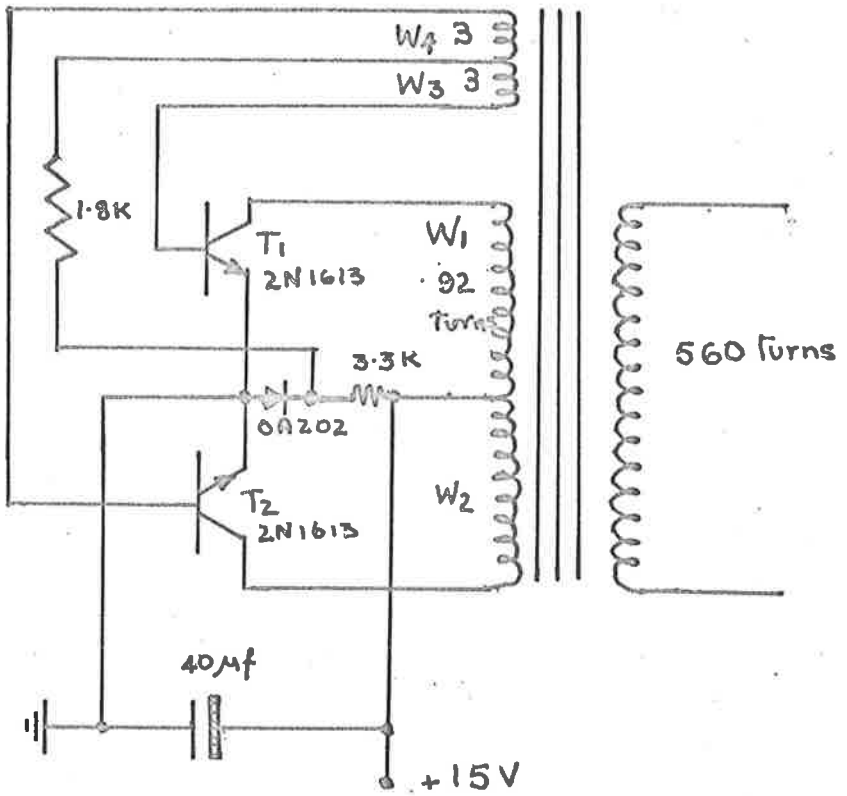

Figure A.1.1 Square wave supply for Dynode Modulator.

in current will induce in W3 a further decrease in the base-emitter potential of T1 and, at the same time, by W4, an increase in the base-emitter potential of T2 causing this transistor to conduct. The cycle is now repeated, producing a square wave across the output of the secondary winding, the magnitude of which is determined by the turns ratio of the primary and secondary windings.

The bias resistors are included to assure the initial unbalanced condition upon switch on of the low voltage supply.

APPENDIX 2

PHOTOMULTIPLIER HIGH TENSION SUPPLY

The circuit for this component is shown in Figure A.2.1. The operation of this circuit, which supplies the negative high tension for the photomultipliers carried in the experimental package is based upon a saturated core oscillator as was the dynode modulator described in Appendix 1. In the case of this system the output square wave is applied to a voltage doubler network.

If the polarity of the transformer output is such that diode D1 conducts, capacitor C1 becomes charged such that the potential across it is V_p. On the reversal of polarity, diode D2 will conduct and capacitor C2 becomes charged, with a potential across it of V_p so that the total potential between earth and the -HT point is $2V_p$. This is the condition for zero current drain. In the case of the practical system, the current drain was 250 micro amps considering one half of the network, the potential is 600 volts which, at a current of 2.5×10^{-4} amps gives an effective resistance of 2.4×10^{6} ohms resistance. The time constant of the discharge of a capacitor of 0.22 microfarads is then 0.5 seconds. The running frequency of the oscillator was

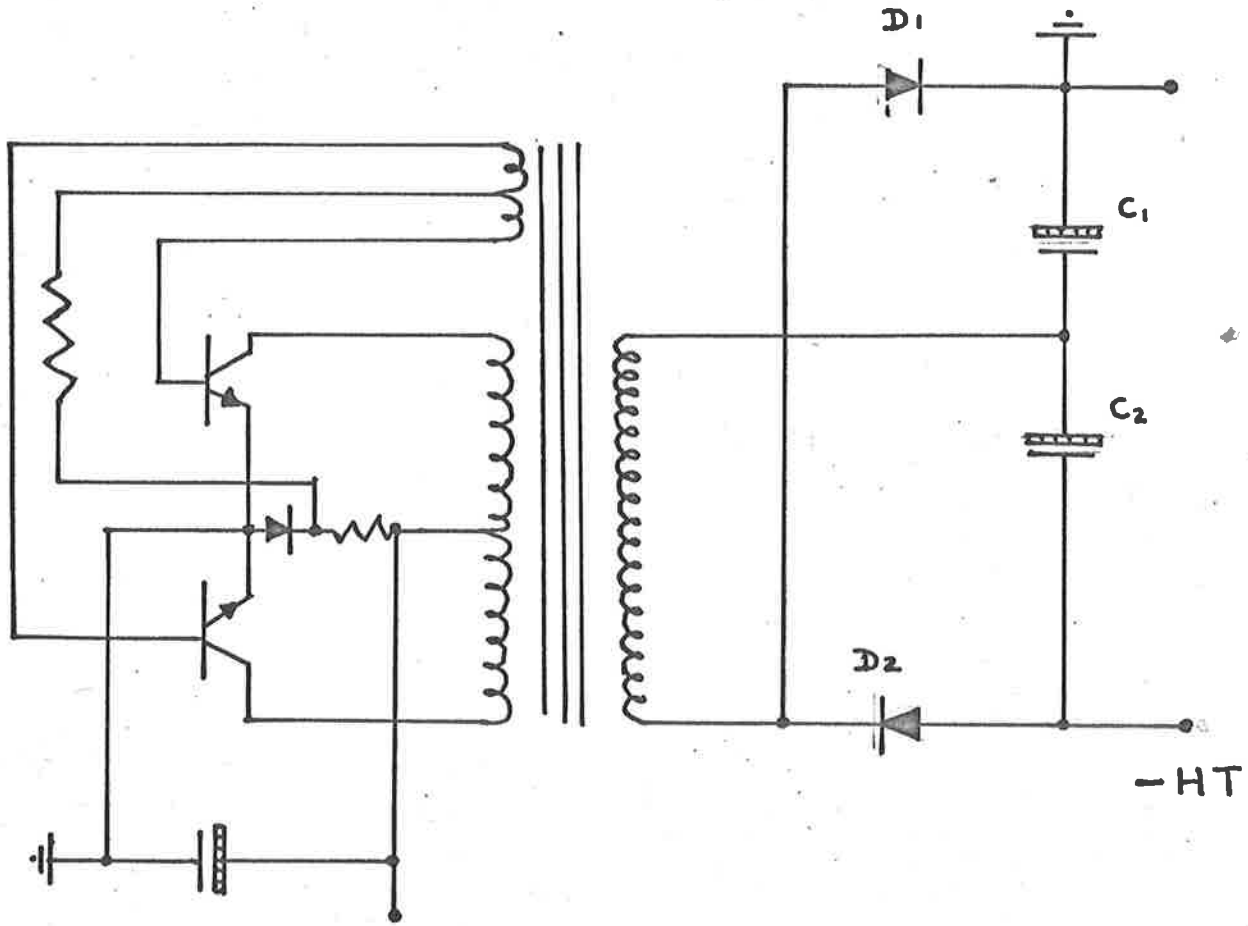

Figure A.2.1 Photomultiplier High Tension Supply. The Squarewave generator is as described in Appendix 1.

1.5 kc/s so that the capacitor will only discharge to $(1 - \exp(1.3\text{x}10^{-3}))V_p$ during a cycle making the ripple voltage negligible.

APPENDIX 3

A THREE STAGE A.C. AMPLIFIER

This is the type of amplifier which was used for all sensors carried in the instrumentation of both rockets. The circuit is shown in Figure A.3.1.

The A.C. input signal is applied to the base of transistor T1 which is biassed by resistors $R1_{a,b}$ but which maintains a high input impedance through resistor R2. The output of T1 is cascaded through T2 onto an emitter load of resistor R3. The full signal is applied to a rectifying network C1, R4 and D1 and gives output of stage 1. The signal at R3 is A.C. coupled to the base of T3 and the gain of this stage is set by the magnitude of the A.C. coupled feedback resistor R5. The output in this case appears on the collector load and is similarly treated to the output of stage 1, supplying the output of stage 2 and the input to stage 3. Stage 3 is similar to stage 2.

The initial gain of stage 1 which may require variation, dependent upon the sensitivity of the photo-electric detector, may be set by changing the input impedance through R6. Also in the input circuit is the temperature compensation net of M15 and R7.

Because of the limitation of the excursion of

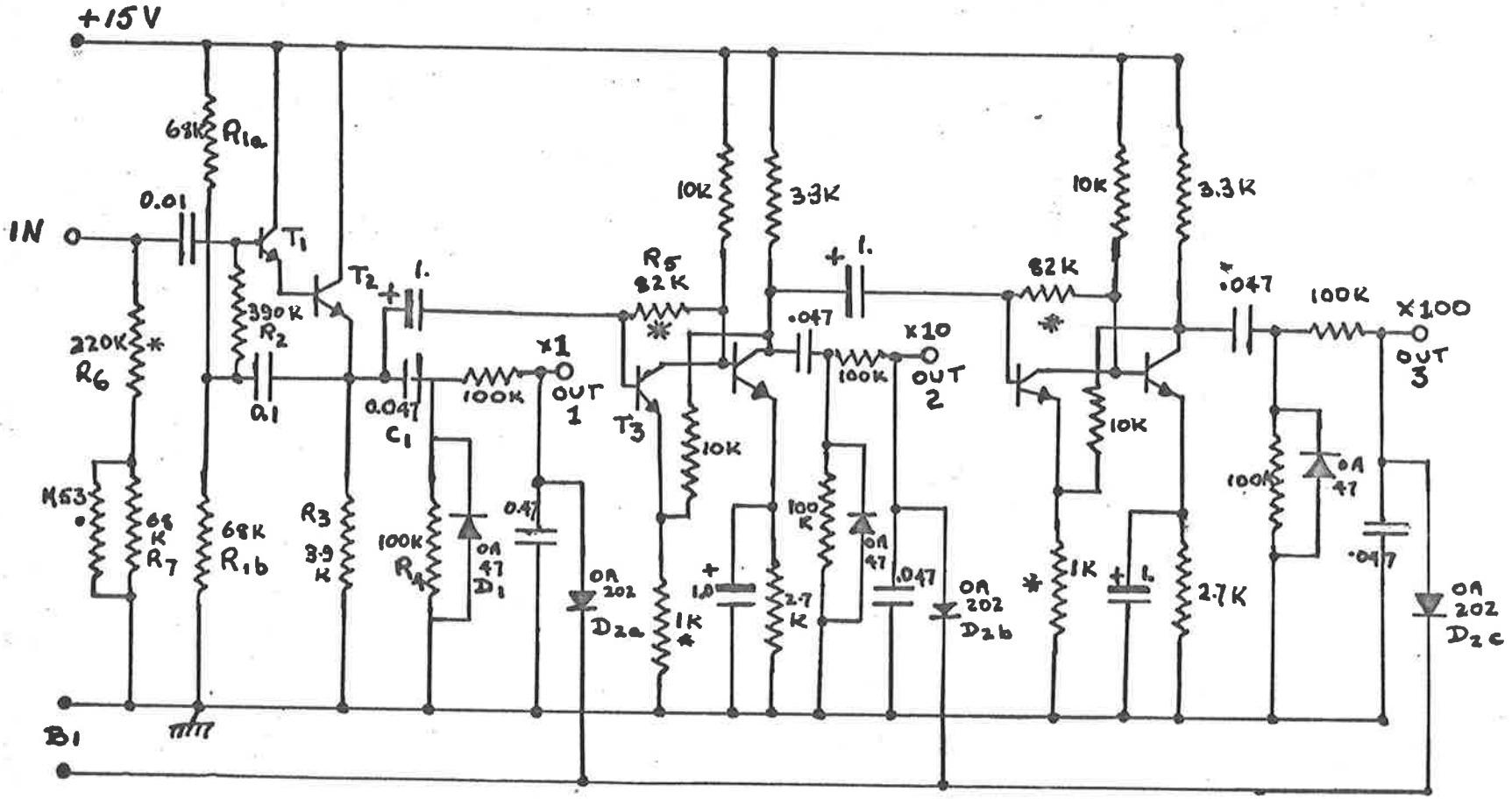

Figure A.3.1 Three stage amplifier.
Transistors - 2N 3694, Resistor - Ohms Capacitance - μ farads
* - Adjust of test.

any signal applied to the telemetry, set to avoid any false synchronous signal, all outputs were limited to 1.5 volts by the net $D2_{a,b \text{ and } c}$ and the battery B1.

Owing to the forward conducting characteristic of the diodes the signal applied to the telemetry will rise a little above 1.5 volts but this rise is not great enough to stimulate a sync signal.

APPENDIX 4

IN FLIGHT CALIBRATION SYSTEM

The in flight calibration system consisted of grain of wheat bulbs which were energised periodically for the duration of the flight. The circuit providing the timing and the switching of the system is shown in Figure A.4.1. The operation of the circuit is as follows.

Transistor T1 is biassed to conduct 1 micro amp. By gain of T2 current through lower bias resistor turns T1 hard on, charging C1 till potential applied through collector of T1 is sufficient to cut off T2. Reduced current through lower bias resistor cuts off T1 and C1 discharges directly till T1 is biassed on, turning on T2, producing negative going edge which is passed to a monostable the output of which is applied to transistor T3 with lamp B as the collector load. The positive going edge of the pulse applied to the first flash circuit fires the second flash. The zener in base circuit of the output transistor of the monostable prevents regeneration of a negative edge due to the high current load on the -15 volt line.

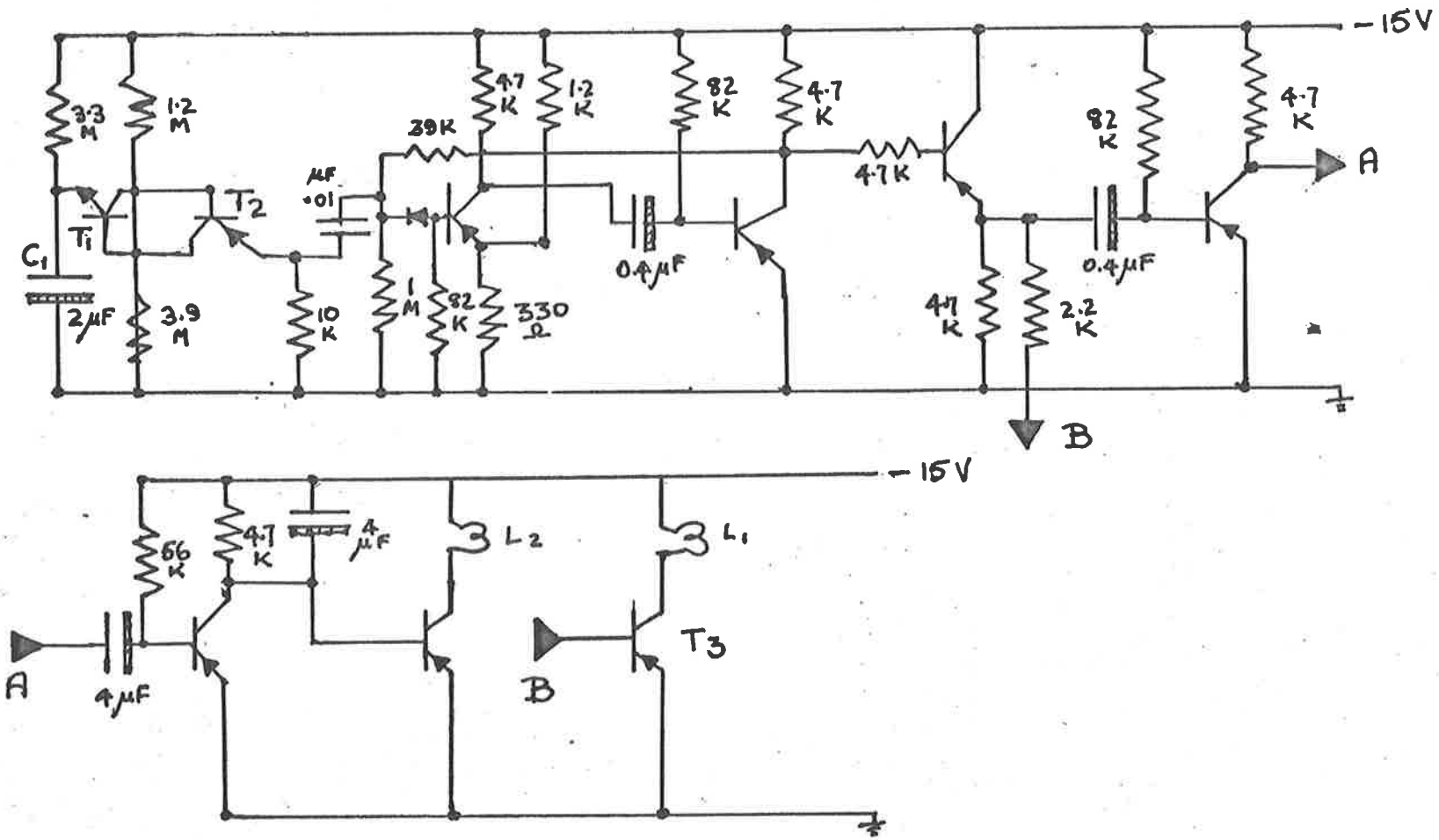

Figure A.4.1 Calibration lamp timer and power switch.

APPENDIX 5

CONTROL SWITCHING OF HIGH TENSION SUPPLIES

Because of the vibration of the vehicle caused by the rapid acceleration through the dense layers of the atmosphere, it is necessary that the high tension voltage be applied after the completion of the powered stage of the flight. No continuous switching was available from the internal rocket system the clock pulses resulting from the motion of a wiper arm over isolated contacts. To ensure the continued operation of the high tension unit, a switching net as shown in Figure A.5.1 was used. The operation is described below.

Relay RL2, which is normally closed, may be held open by ground station controls. Voltage lines permitting such operation are removed as the vehicle leaves the launcher.

For laboratory and ground checks, switch S1 supplys control of the circuit, closing RL1 which both locks itself closed and closes the low voltage line, activating the high tension unit. RL may be opened by energising RL2 after opening S1.

At launch RL2 is closed and S1 is open. After

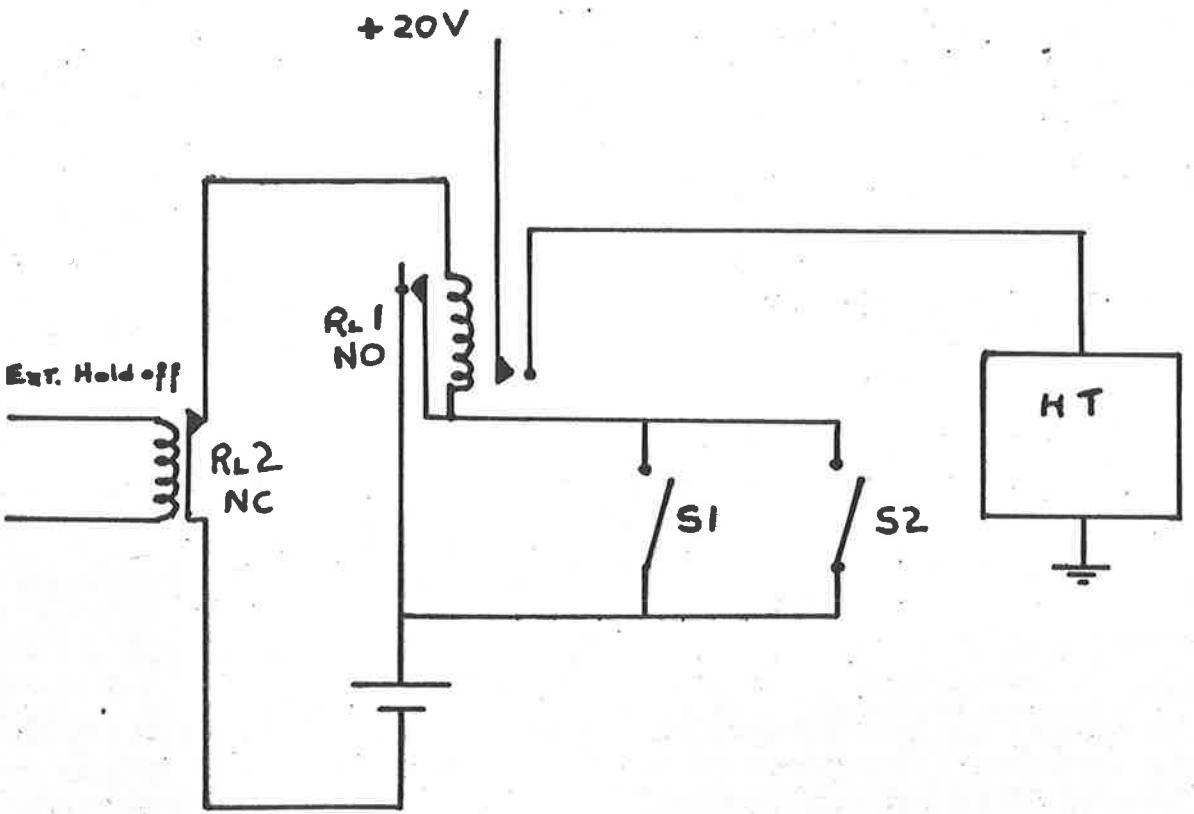

Figure A.5.1 Control switching of H.T. Supplies.

a period of 27 seconds after launch the event clock briefly closes S2. This energises RL1 which now remains closed irrespective of the later condition of S2 and thus maintains the low voltage supply to the high tension unit.

APPENDIX 6

PUBLICATIONS

The following papers have been written on the work described in this thesis.

J.H. Carver, B.H. Horton and F. Burger, 1966 "Nocturnal Ozone Distribution in the Upper Atmosphere", Journal of Geophysical Research, 71, 4189.

J.H. Carver, B.H. Horton and F. Burger, 1967, "Rocket Determination of the Night Ozone Distribution and the Lunar Ultraviolet Flux", Space Research VII, North Holland Publishing Co., pp1020-1028.

REFERENCES

Allen, C.W., 1963, Astrophysical Quantities (The Athlone Press).

Barr, W.L. and Jenkins, F.A., 1956, Journal of the Optical Society of America, 46, 141.

Bastin, J.A., 1966, Nature, 212, 171.

Bates, D.R. and Nicolet, M., 1950, Journal of Geophysical Research, 55, 301.

Berg, C.A., 1964, Nature, 204, 461.

Blake, A.J., Carver, J.H. and Haddad, G.N., 1966, J. Quant. Spectrosc. Rad. Transfer, 6, 451.

Blankenship, J.R. and Crutzen, P.J., 1966, Tellus, 18, 160.

Brewer, A.W. and Milford, J.R., 1960, Proceedings of the Royal Society, (A), 256, 470.

Cadle, R.D. and Powers, J.W., 1966, Tellus, 18, 176.

Carver, J.H., Mitchell, P., Murray, E.L. and Rofe, B., 1965, Space Research, VI, 373.

Clough, S.A. and Kneizys, F.X., 1965, A.R.C.R.L. Research Paper, 170.

Coyne, G.V., 1962, Astronomical Journal, 68, 49.

Craig, R.H., 1965, The Upper Atmosphere, Meteorology and Physics (Academic Press).

Davies, H., 1954, Proceedings of the Institute of Electrical Eng.s, 101, 209.

Evans, J.V., 1962, Physics and Astronomy of the Moon, Ed. Z. Kopal (Academic Press), p441.

Fehsenfeld, F.C., Schmeltekopf, A.L., Shiff, H.I. and Ferguson, E.E., Planetary and Space Science, 15, 373, 1967.

Friedman, R.M., Rawcliffe, R.D. and Meloy, G.E., 1963, Journal of Geophysical Research, 68, 6419.

Friedman, H., Chubb, T.A. and Siomkajlo, J.M., 1964, Sounding Rocket Research Techniques, Instruction Manual (9), (IQSY Secretariat, London.)

Furakawa, P.M., et al, 1967, National Center for Atmospheric Research, Tech. Note 26, February, 1967.

Gast, J., 1965, Handbook of Geophysics and Space Environment, A.F.C.R.L.

Gehrels, T., 1964, Icarus, 3, 491.

Godson, W.L., 1960, Quarterly Journal of the Royal Meteorological Society, 86, 301.

Gold, T., 1964, The Lunar Surface Layer, Ed. Salisbury and Glaser (Academic Press) p345.

Gotz, F.W.P, Meetham, A.R. and Dobson, G.M.B, 1934, Proceedings of the Royal Society (A), 145, 416.

Grigg, M., Chapter 4, "The Middle Ultraviolet, Its Science and Technology", (Wiley and Sons, London).

Hapke, B., 1964(a), Journal of Geophysical Research, 69, 1147.

Hapke, B., 1964(b), The Lunar Surface Layer, Ed. Salisbury and Glaser, (Academic Press), p323.

Harris, D.L., 1961, Planets and Satellites, Ed. Kuiper and Middlehurst, (University of Chicago Press).

Heddle, D.W.O., 1962, Nature, 193, 861.

Heddle, D.W.O., 1963, The Observatory, 83, 225.

Heppner, J.P. and Meredith, L.H., 1958, Journal of Geophysical Research, 63, 51.

Hering, W.S. and Barden, T.R., 1964, Air Force Cambridge Research Laboratories Report 64-30 (II) July, 1964.

Howard, J.N., 1961, Air Force Surveys in Geophysics, No 142.

Hunt, B.G., 1965, Journal of Atmospheric and Terrestrial Physics, 27, 133.

Hunt, B.G., 1966, Journal of Geophysical Research, 71, 1385.

Inn, E.C.Y., and Tanaka, Y., 1959, Advances in Chemistry, Series 21, 263.

Jaffe, L.D., 1967, Journal of Geophysical Research, 72, 773.

Johnson, F.S., Purcell, J.D., Tousey, R., and Watanabe K., 1952, Journal of Geophysical Research, 57, 176.

Kartashev, A.V., Bozhulin, P.A., and Markov, M.N., 1966, Cosmic Research, 4, 530.

Keneshea, T.J., 1967, A.F.C.R.L. 67-0221, Environmental Research Papers, No 263.

Koller, L.R., 1952, Ultraviolet Radiation, (John Wiley and Sons).

Kristianpoller, N. and Knapp, R.A., 1964, Applied Optics, 3, 915.

Leovy, C., 1964, Journal of Atmospheric Science, 21, 238.

Lindzen, R.S., 1967, Quarterly Journal of the Royal Meteorological Society, 93, 18.

Lyon, R.J.P., 1964, N.A.S.A. Contractors Report, NASA CR-100, November, 1964.

Miller, D., 1960, Handbook of Geophysics, 2nd Ed. (McMillan Co., New York).

Miller, D.E., and Stewart, K.H., 1965, Proceedings of the Royal Society, Series A, 288, 540.

Mulliken, R., 1942, Reviews of Modern Physics, 14, 204.

Murgatroyd, R.J., 1957, Quarterly Journal of the Royal Meteorlogical Society, 83, 417.

Murgatroyd, R.E., 1963, Journal of Atmospheric Sciences, 20, 213.

Murgatroyd, R.J., 1965, World Meteorlogical Organization Tech. Note 70.

Nicolet, M., 1964, Transactions of the Faraday Society, 37, 7.

O'Brien, R., 1967, Honours Thesis, University of Adelaide.

Oetking, P., 1966, Journal of Geophysical Research, 71, 2505.

Packer, D.M., 1961, Annales Geophysique, 17, 67, 1961.

Poloskov, S.M., L'Vova, A.A. and Mikorove A.E., 1967, Space Research, VII, 1009, (North Holland Publ. Co).

Porteus, J.C., 1963, J. Opt. Soc. America, 53, 1394.

Ramahathan, K.R. and Dave J.V., 1957, Annals of the I.G.Y, 5, 23.

Randhawa, J.S., 1966a, U.S. Army Electronics Command Report, ECOM-5039, March, 1966.

Randhawa, J.S., 1966b, U.S. Army Electronics Command Report, ECOM-5064, July, 1966.

Rawcliffe, R.D., Meloy, G.E., Friedman, R.M. and Rogers E.H., 1963, Journal of Geophysical Research, 68, 6425.

Reed, E. and Scolnik, R., 1964, NASA Report, X-613-64-267, September, 1964.

Regener, V.H., 1960, Journal of Geophysical Research, 65, 3975.

Rofe, B., 1966, Weapons Research Establishment Tech. Note PAD 115, April, 1966.

Roney, P.L., 1965, Journal of Atmospheric and Terrestrial Physics, 27, 1177.

Sampson, J.A.R., 1964, Journal of the Optical Society of America, 54, 6.

Schaefer, E.T., 1963, Journal of Geophysical Research, 68, 1175.

Schroeder, D.J., 1962, Journal of the Optical Society of America, 52, 1380.

Smith, L.G. and Weekes, L., 1965, G.C.A. Tech. Report No 65-10-N.

Sokolova, R.S. and Krylova, T.N., 1959, Optika Spect., 6, 513.

Stair, R. and Johnston, R., 1953, Journals of Research, National Bureau of Standards, 51, 81.

Tanaka, Y., Inn, E.C.Y. and Watanabe, K., 1953, Journal Of Chemical Physics, 21, 1651.

Tarasova, T.N., 1963, Planetry and Space Science, 11, 437.

Thompson, T.W. and Dyce, R.B., 1966, Journal of Geophysical Research, 71, 4843.

Tousey, R., 1963, Space Science Reviews, 2, 1.

Tousey, R., 1966, The Middle Ultraviolet: Its Science and Technology, Ed. A.E.S. Green, (John Wiley and Sons).

Twomey, S., 1966, Journal of Geophysical Research, 66, 2153.

Vassey, E., 1937, Ann. de Phys., 8, 679.

Venkateswaren, S.V., Moore, J.G. and Krueger, A.J., 1961, Journal of Geophysical Research, 66, 1751.

Wallace, L., 1962, Journal of Atmospheric Science, 19, 1.

Walton, G.F., 1957, Annals of the I.G.Y., 5, 9.

Warneck, P., 1964, Transactions of the Faraday Society, 37, 57.

Wattson, R.B., and Danielson, R.E., 1965, Astrophysical Journal, 142, 16.

Williamson E.J., and Houghton J.T., 1965, Quarterly Journal of the Royal Meteorlogical Society, 91, 330.

Yamamoto, G., 1962, Journal of Atmospheric Science, 19, 182.